Development of an optically synchronized seed source for a high-power few-cycle OPCPA system

Izhar Ahmad

SIGILL·UNIVERSI·TAT·LUDOVIC·MAXIM·

München 2011

Development of an optically synchronized seed source for a high-power few-cycle OPCPA system

Izhar Ahmad

Dissertation
an der Fakultät für Physik
der Ludwig–Maximilians–Universität
München

vorgelegt von
Izhar Ahmad
aus Toba Tek Singh, Pakistan

München, den 16. Juni 2011

Erstgutachter: Prof. Dr. Stefan Karsch

Zweitgutachter: Prof. Dr. Abdallah M. Azzeer

Tag der mündlichen Prüfung: 11. Juli 2011

Contents

Zusammenfassung ix

Abstract xi

1 Introduction 1

1.1 Brief history of early laser development . . . 1
1.2 Applications of short pulsed lasers . . . 2
1.3 Motivation of ultrashort high power pulses . . . 3
1.4 Different techniques for amplification of short pulse lasers . . . 3
1.5 The Petawatt Field Synthesizer—PFS . . . 6
  1.5.1 Schematic layout of PFS . . . 7
1.6 Thesis outline . . . 8

2 Seed generation and stretcher-compressor setup for the CPA pump laser 11

2.1 CPA pump laser seed generation . . . 11
2.2 Stretcher compressor setup for CPA pump laser chain . . . 14
  2.2.1 Dispersion calculations . . . 14
  2.2.2 Ray trace for the stretcher . . . 18
  2.2.3 Ray trace for the grating compressor . . . 20
  2.2.4 Alignment sensitivity . . . 21
  2.2.5 Implementation of the stretcher and compressor . . . 24
2.3 Conclusion . . . 28

3 Chirped pulse amplification of the oscillator output 31

3.1 Femtopower amplifier upgrade . . . 31
  3.1.1 Dispersion calculation of the amplified stretched pulse . . . 33
  3.1.2 Dispersion of the prism compressor . . . 34

3.1.3 Hybrid pulse compression (HPC) 39
3.2 All-dispersive mirror compressor 43
3.2.1 Stretcher-compressor setups of conventional CPA systems 43
3.2.2 Implementation of the ADMC 44
3.2.3 Outlook 46
3.3 Conclusion 49

4 Broadband seed generation for OPCPA chain 51
4.1 Optical parametric amplification 51
4.2 Idler generation using NOPA 54
4.2.1 Design considerations 56
4.2.2 Experimental setup for idler generation using NOPA 61
4.3 Broadband seed generation using cascaded spectral broadening 64
4.3.1 Spectral broadening in gaseous media 65
4.3.2 Experimental setup 67
4.3.3 Generation of few-cycle light pulses 69
4.3.4 HCF-filament 72
4.3.5 Cascaded-HCF 74
4.4 Comparison of different OPCPA seed generation methods 77
4.5 OPCPA seed stretcher 79
4.5.1 Characterization of the stretched seed-pulses 81
4.5.2 Scheme of final compression 82
4.6 Summary 83

5 OPCPA using DKDP and timing synchronization measurements 87
5.1 Experimental setup 88
5.2 Level of synchronization between the OPCPA pump and seed pulses 89
5.2.1 Timing jitter measurements 89
5.2.2 Results and discussion 91
5.2.3 Active stabilization of timing jitter 91
5.2.4 Timing jitter due to the change in beam pointing at the input of the compressor 93
5.2.5 Timing jitter due to the change in beam pointing inside the compressor . 98
5.3 OPCPA experiments in DKDP 100
5.4 Conclusion 103

6 Summary and outlook 105

A List of optical components in the current CPA pump laser chain 109

B Dispersion calculations of a double-prism pair compressor 111

C Formulae for the peak power, peak intensity and peak fluence of a Gaussian pulse 117

D Redshift of few-cycle near-infrared pulses in filamentation regime 119

Zusammenfassung

Optische parametrische Verstrkung (OPCPA), bei welcher kurze Pumppulse verwendet werden, bietet ein neues und vielversprechendes Konzept für die Verwirklichung einer Quelle, die Höchstleistungs-Lichtpulse mit einer Pulsdauer von nur wenigen Lichtzyklen erzeugt [1, 2]. Dieser Ansatz reicht weit über die Grenzen herkömmlicher Lasertechnologie hinaus [3, 4], und erlaubt durch die Verwendung von dünnen nichtlinearen Verstärkerkristallen und einer nichtkollinearen optischen parametrischen Verstärkergeometrie (NOPA) eine beispiellos breitbandige Verstärkung. Durch die wenige pikosekunden kurzen Pumppulse können äusserst hohe Pumpintensitäten verwendet werden, die eine hohe Verstärkung in diesen dünnen Kristallen sicherstellen. Die hohen Pulsenergien werden in Kristallen mit einem großen Durchmesser erreicht. Das Petawatt Field Synthesizer (PFS) Projekt am Max-Planck-Institut für Quantenoptik (Garching) soll mit dieser neuartigen Technologie Lichtpulse mit einer Dauer von wenigen Lichtzyklen und einer Spitzenleistung im Petawattbereich herstellen.

Die vorgelegte Arbeit befaßt sich mit der Entwicklung einer Ausgangslichtquelle für PFS, die optisch synchronisierte Pulse für die OPCPA-Verstärkerkette und die Pumplaserkette liefert. Wir untersuchen verschiedene Methoden für die Erzeugung der breitbandigen seed-Pulse für die OPCPA-Verstärkerkette im Nahinfrarotbereich. Einerseits verwenden wir ultrakurze Pulse eines Ti:Saphir Systems, die dann durch nichtlineare Effekte spektral verbreitert werden. Andererseits untersuchen wir den Idler-Puls, der in einer NOPA-Stufe erzeugt wird und sich über den gewünschten spektralen Bereich erstreckt. Wir stellen das Konzept zur zeitlichen Streckung und Komprimierung der seed-Pulse für sowohl die Pumplaserkette als auch der OPCPA-Kette vor. Diese Ausgangslichtquelle ermöglicht erste Verstärkerexperimente in der OPCPA-Kette mit pikosekunden Pumppulsen, die wir am Ende dieser Arbeit präsentieren. In diesen NOPA-Experimenten in DKDP Kristallen haben wir eine breitbandige Verstärkung zeigen können, die erwartungsgemäßeine Pulsdauer von weniger als zwei optischen Zyklen unterstützt.

Abstract

The scheme of short-pulse pumped optical parametric chirped-pulse amplification (OPCPA) offers a promising route towards a completely new regime of ultra-high power few-cycle pulse generation [1, 2], which reaches well beyond the limits of the conventional laser technology [3, 4]. In this approach, the gain bandwidth limitations of conventional laser amplification are circumvented by using thin OPA crystals in a non-collinear pump-signal geometry (NOPA), while the high gain and pulse energies are ensured by the intense pumping and large crystals sizes. The Petawatt-Field-Synthesizer (PFS) project at the Max Planck Institute of Quantum Optics (Garching, Germany), aims at delivering waveform-controlled few-cycle laser pulses with PW-scale peak power based on few-ps pumped OPCPA.

This work focuses on the development of a frontend light source for the PFS system to deliver optically synchronized seed pulses for the OPCPA beam-line and the pump laser. Methods of generating the broadband near-infrared seed pulses for the OPCPA chain by spectral broadening using few-cycle pulses, and idler generation using NOPA are presented. Concepts of stretching both seed pulses, for the pump and the OPCPA, in time and their recompression after amplification are discussed. A detailed experimental and theoretical investigation of timing jitter between the pump and seed pulses in our system is presented. The experimental demonstration of short-pulse-pumped non-collinear OPCPA in a DKDP crystal is presented showing an ultrabroad gain bandwidth in the visible-near infrared, which supports sub-two optical cycle pulse duration.

Chapter 1

Introduction

1.1 Brief history of early laser development

Light amplification by stimulated emission radiation—laser, is considered as a landmark invention of the Physics in the mid-20th century. Albert Einstein's proposal [5], that photons could stimulate emission of identical photons from excited atoms, is considered as a conceptual building block of the laser. The first experimental recognition of his idea took place in ruby in 1960 [6]. In the following years, much effort was expended for exploring new laser transitions in various media: crystalline solids, gases, liquids etc. Utilizing this variety of media it was soon possible to observe laser transitions in a very wide spectrum, ranging from the vacuum ultraviolet (VUV) to the mid-infrared (mid-IR) [7]. Lasing action in the near infrared (NIR) was reported in He-Ne gas mixtures [8] followed by that in Nd^{+3} doped solid-state materials in 1961 [9]. In the same year, population inversion in semiconductor materials was demonstrated, emitting in the NIR spectral range [10]. In 1961, the so-called giant optical pulsation was discovered in Ruby by the Kerr-effect Q-switching technique [7]. In 1962 the stimulated emission in He-Ne at a visible wavelength of 632.8 nm was demonstrated [7]. The laser transitions in the mid-IR at 10 μm in the vibrational-rotational states of the CO_2 molecules were discovered in 1964 [11]. This was followed by a high power CO_2 laser delivering 200 W in continuous wave (CW) mode [12]. The first optically pumped dye laser action was reported in 1966 [13]. In the subsequent years a number of dye solutions were discovered emitting laser radiation tunable in the visible and in the NIR [7]. The discovery of the Excimer laser in 1971 showed the possibility of direct lasing, without frequency up conversion, at 173 nm in the VUV spectral region [14].

Compared to the CW lasers in which the optical power remains constant over the time, the output of the pulsed lasers appears in pulses of some duration at a specific repetition rate. The peak power in this case is determined by the ratio of the pulse energy to the pulse duration. Shortening the pulse duration for a given output energy results in enhancement of the peak power as well as peak intensity (i.e. pulse energy per unit time per unit area). The quest to reach high intensity for studying laser-matter interactions and to explore the secrets of nature such as atomic or molecular structures by reducing the observation timing window demands the lasing operation in the ultrashort pulse mode. The laser sources emitting broadband spectra were requisite for obtaining such short pulses owing to the fact that the shortest achievable pulse duration from an optical spectrum is inversely proportional to its bandwidth [15]. The dye lasers were the first in the race of ultra-short pulse generation owing to their tunable and, rather, broad output spectrum [16]. In the early 1970's, Q-switched mode locking of the dye laser output produced sub-picosecond long pulses (1 ps $= 10^{-12}$ s) at kW-level peak power [17, 18]. This innovation led to interest in solid-state lasers with vibronic transitions, in which electronic transitions strongly interact with atomic vibrations, so the resulting vibronic transition show a broad gain bandwidth. In 1980 Walling et al. [19] demonstrated a cobalt-doped alexandrite laser widely tunable in the 700–800 nm spectral range operating in both CW and pulsed mode. In 1988 Moulton [20] pioneered today's most important tunable solid-state laser, titanium-doped sapphire (Ti:Al_2O_3) which have excellent thermal properties and an exceptionally broad gain-bandwidth of 660 nm to 1180 nm. A big boost to producing short pulses came from the development of Kerr-lens mode-locking in 1991 [21], in which self-focusing within the Ti:sapphire crystal results in self-bunching of a laser pulse circulating within the laser cavity. This new technique allowed a self-mode-locked Ti-sapphire laser to generate pulses as short as 60 femtosecond (1 fs $= 10^{-15}$ s). Later, utilization of intracavity dispersion management with state-of-the-art chirped mirror technology helped to reduce the pulse duration to below 10 fs [22, 23]. Nowadays sub-5 fs lasers have become turn-key devices in research laboratories.

1.2 Applications of short pulsed lasers

Ultrashort light pulses have pushed the frontiers of optical telecommunication, material processing, medical surgery and ultrafast spectroscopy. Femtosecond lasers enable precise processing of any material with minimal collateral damage and unprecedented reproducibility and precision. This permits high-quality machining, structuring of all kinds of materials and soft biological tissues with minimal invasive effects [24, 25]. The propagation of NIR femtosecond soliton in optical fibers with minimal loss offers data transmission with unprecedented rate of multi-Tbit/s over thousands of kilometers for telecommunication. In fundamental research, the femtosecond pulses has been extensively used in the studies of time-resolved dynamics, leading to significant advances in the understandings of intramolecular processes, chemical bond breaking and bond formation, and the interaction of photoactivated molecules with their environment. In 1999 this work was accredited by the Nobel Prize in Chemistry for A. H. Zewail [26]. The quest to probe atomic and electronic dynamics on ever shorter time-scales calls for light pulses with subfemtosecond (attosecond, 1 as $= 10^{-18}$ s) duration [27]. A techniques of higher order harmonic generation (HHG), in which a highly nonperturbative interaction of an intense few-cycle laser with an atomic or molecular medium generates new frequencies [28, 29, 30, 31], is generally employed for attosecond pulse generation [27, 32]. Real-time observation of ultrafast-dynamic processes can be achieved by the attosecond pump-probe experiments. Recent advancement in this field has provided a real-time picture of the valence-electron motion using attosecond light pulses [33].

1.3 Motivation of ultrashort high power pulses

High-power, few-cycle light pulses are of great interest for studying laser-matter interactions in the relativistic regime, i.e. at an intensity level in excess of 10^{18} W/cm^2 which leads to relativistic electron motion in the laser field. A number of applications such as the generation of monoenergetic electron beams or the generation of intense single attosecond pulses from solid-density plasmas has been emerged from this field [34, 35, 36, 37, 38] and call for light sources delivering ever shorter and more powerful pulses. Experiments so far have established the fact that these interactions are highly sensitive to premature heating of the target caused by a non-ideal temporal contrast (i.e. the ratio of light emitted before the main peak and the main peak itself). As an additional benefit, shorter pulses require less total energy for a given peak power. As suggested by theory [39], the relativistic interaction of such a laser pulse with a solid surface is a promising candidate for high efficiency generation of higher-order harmonics and the production of high-intensity, high-energy attosecond-pulses. While experimental evidence already exists in support of this mechanism [38], in order to exploit it to its full extent a few-cycle, petawatt-class driver laser is necessary. Also the acceleration of electron bunches would benefit from this new laser source. Here, improved stability is expected [37] making such bunches more suitable for further applications [40]. Another important application is proton acceleration with high intensity laser pulses ($> 10^{21}$ W/cm^2) [41, 42], which can lead to effective use of proton beams for medical applications [43].

1.4 Different techniques for amplification of short pulse lasers

Before 1985, the laser amplifiers were restricted to directly amplifying even short input pulses. The risk of optical damage of the gain media, due to the self-focusing caused by the change of intensity-dependent refractive index, was confronting the amplification above few-terawatt power levels (1 TW=10^{12} W) with the manageable beam sizes (< 0.5 m) [44]. The chirped pulse

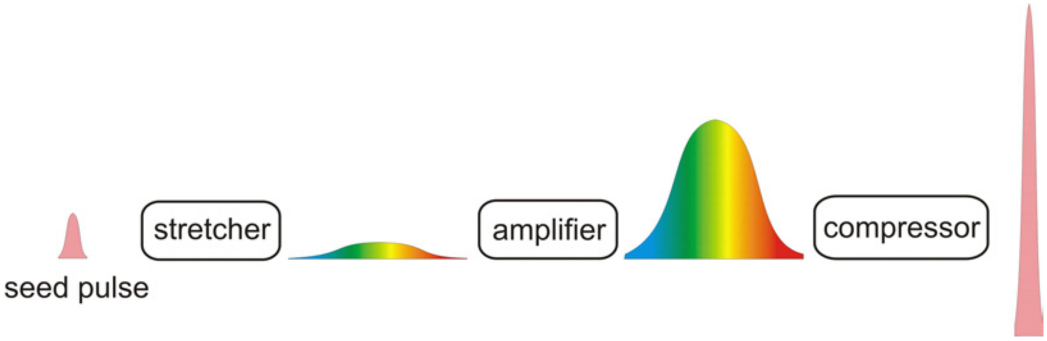

Figure 1.1: Principle of chirped pulse amplification

amplification (CPA) technique was first introduced by Strickland and Mourou [3] to overcome the problem of nonlinear effects and optical damage with increasing energies of short pulses. The amplifiers, in this scheme, are seeded with low-energy pulses temporally broadened in a dispersive pulse stretcher to permit for amplification without damaging the gain medium. The chirp of the amplified pulses is subsequently removed in a pulse compressor introducing a group-delay dispersion (GDD) of opposite sign. The pulse duration is thereby restored close to that of the input pulse (Fig. 1.1). The pulse stretching and compression can be obtained by a number of different setups such as, grating pairs [45, 46], prism pairs [47], grism pairs (a combination of a grating and prism) [48], high-dispersive mirrors [49], and material [49, 50, 51] etc. A few of these stretcher and compressor setups will be discussed in chapters 2 and 3. Detailed description about the CPA can be found in Ref. [44].

Based on CPA, as high as PW level peak power amplification was first obtained in 1996 at the Lawrence Livermoore National Laboratories (LLNL, US), with 660 J of pulse energy at a width of 440 fs using neodymium glass (Nd:glass) [52, 53]. Similar systems were later developed at the Rutherford Appleton Laboratories (RAL, UK) and Osaka University (Japan) to deliver amplified compressed pulses of 500 fs with 670 J [54] and 470 fs with 420 J [55], respectively. In the meantime a 0.85 PW CPA system was reported to yield 33-fs 28-J [56] pulses at the Japan Atomic Energy Research Institute (Japan) by utilizing the broader gain-bandwidth of Ti:sapphire [20].

Despite such achievements, conventional CPA laser systems suffer from gain narrowing as well as limited gain-bandwidth of the available amplification media and therefore approach an ultimate limit for scaling to the short-pulse regime without subsequent broadening using self-phase modulation techniques [57, 58]. The broadening techniques also have limitations in their scalability to high energy levels. Moreover, some additional issues such as self-oscillation of laser amplifiers in transverse directions (i.e. transverse lasing) and thermal lensing result in degradation of the amplification process and spatio-temporal quality of the compressed pulses.

In contrast to the conventional CPA technique which relies on the traditional laser process, i.e. population inversion of an amplification medium under excitation from a pump, optical parametric amplification (OPA) [59] originates from a three-wave mixing process inside a nonlinear crystal. Here, a short-wavelength high-intensity beam, the pump, amplifies a longer-wavelength lower-intensity beam, the signal, in a nonlinear medium. This interaction leads to the spontaneous generation of a third beam, the idler, so that the energy and momenta are conserved between the three beams. Owing to the very broad gain-width that can be achieved in the nonlinear frequency mixing process, the amplified spectrum can support few-cycle pulse width [60]. When combined with the CPA approach, the nonlinear wave mixing process (termed as optical parametric chirped pulse amplification (OPCPA) [4]) enables us to reach ultra high powers [51, 61].

There are many aspects which make the OPCPA better suited than lasers for realizing a high-power short-pulse light source. Firstly, the parametric amplification is an instantaneous and propagation-direction dependent process which make it intrinsically free from the transverse lasing hence removing one substantial limitation of high power CPA laser systems. Secondly, the single-pass gain in OPA system is much higher than that of the conventional CPA lasers [4, 62] therefore only a few single-pass stages are required for the achieving the same gain, hence avoiding the complexities of multipass cavities. Thirdly, in the case of the OPCPA, the energy difference between the pump and the signal waves is released in form of an idler wave, rather than that of heat as in CPA lasers, which, being less absorbed in the nonlinear crystal, causes significantly lower thermal load. This feature is a great benefit for high average power systems. Fourthly, the idler wave can also be useful in some case; e.g. generation of a short pulse [63] or seeding an amplifier [64, 65] in a spectral region difficult to reach with conventional techniques. Finally, OPCPA provides many degrees-of-freedom to obtain large amplification bandwidths such as the nonlinear crystal and the geometry of the nonlinear interaction etc. [4, 60]. This allows for higher flexibility in the conception and optimization of the amplifier design, as compared to the systems which are restricted to the laser amplifier medium. These features make parametric amplification more attractive, particularly for the amplifier dedicated for high-intensity applications. Nonetheless, the absence of energy storage imposes strict requirement for temporal overlap of the pulses inside the crystal to ensure interaction between the pump and the signal pulses. Precise control over the pulse timing is hence required to achieve reasonable conversion efficiency. This issue clearly becomes especially severe at shorter pump pulse duration.

Based on OPCPA, the first PW-level peak power OPCPA system with 24 J in 43 fs was demonstrated in 2007 [61] using DKDP (Potassium Dideuterium Phosphate: KD*P). This was followed by 80-mJ 8.5-fs ($\approx$10 TW) parametric amplification in BBO (Beta Barium Borate: β-BaB_2O_4). A 1.1-PW hybrid laser system utilizing both the OPCPA and conventional CPA-based laser amplification techniques was reported in 2009 [66]. A number of high power systems based on OPCPA or conventional CPA are currently in the development phase: e.g. 10 PW (300 J, 30 fs) at the RAL, UK [67]; 10 PW (150 J, 15 fs) APPOLON at the Institute Lumiere Extreme [68], France; and 200 PW pan-European Laser facility, "The Extreme Light Infrastructure—ELI [68, 69]".

In most of the PW-class light sources, reported to date [53, 54, 55, 56, 61, 66], the pump pulse duration range from 100 ps to few-ns, while the output compressed pulses could only reach down to a duration of a few-tens of femtoseconds. The PW-level amplification with few-cycle compressed pulses is yet to be demonstrated and constitutes the main goal of the development of the Petawatt Field Synthesizer (PFS) infrastructure at the Max-Planck Institute of Quantum Optics (MPQ), Germany. In the following section a brief overview of the PFS-design is presented.

1.5 The Petawatt Field Synthesizer—PFS

The PFS system is designed to deliver few-cycle (5 fs) laser pulses with an energy of >3 J and a repetition rate of 10 Hz. The focussed intensity is expected to reach or exceed 10^{22} W/cm^2 [1]. The design of the PFS is based purely on OPCPA technology but with some modifications of the conventional designs. Here, high power, few-ps pump pulses are used to amplify a broadband signal in thin OPA crystals to achieve multi-Joule energy in few-cycle pulse durations [2]. The thin OPA crystals ensure large bandwidth in a noncollinear pump-seed arrangement [60], while the high gain and pulse energies are achieved by intense pumping and large crystal size, respectively. This technique possesses immense potential for generating pulses of significantly enhanced contrast, compared with the conventional long-pulse pumped OPCPA, due to the short time window for the parametric fluorescence. Moreover, very simple, compact, and high throughput stretcher-compressor systems, such as bulk glass and chirped mirrors, can be used owing to the small stretching factor. The requirement of high level of temporal synchronization between the pump and seed pulses during parametric amplification in this scheme, to ensure stable gain, calls for an optical synchronization technique where the seed pulses for both the pump and OPCPA chain are derived from a common source (master oscillator: MO). The detailed description of the PFS design is presented in Ref. [2].

The short-pulse-pumped OPCPA to fulfil the design goals of the PFS requires a very special pump source, delivering 1 ps pulses with 15-20 J pulse energy in the green, i.e. a total of ~50 J in the fundamental (infrared) beam, at 10 Hz repetition rate. Such a system is not commercially available and its development is one of the main bottlenecks of the project. The PFS pump source with these specifications is based on the CPA principle [3] using mainly the Yb:YAG (Ytterbium-doped:Yttrium Aluminium Garnet) as an amplification medium pumped by high power laser diodes [70, 71, 72]. The emission cross-section of Yb:YAG is peaked at 1030 nm and its amplification bandwidth supports sub-ps pulse durations [2, 73, 74].

To allow for broadband amplification with reasonable gain, DKDP is chosen to be the host for nonlinear wave-mixing in the OPCPA chain owing to its availability in large aperture as well as broad amplification bandwidth in the range of 700–1400 nm [75] in a noncollinear pump-signal arrangement. The anticipated total pump energy of 15-20 J at 515 nm will be used to amplify the μJ level broadband signal pulse (OPCPA-seed) in 7 or 8 OPCPA stages to achieve the design goals [2]. The design requires the broadband OPCPA-seed pulse to be temporally stretched to 1-2 ps in order to match with the pulse duration of the pumping source to make the OPA process more efficient and to allow for damage-free amplification. This small stretching factor can be achieved by a negative dispersion device, e.g. a prism pair and/or chirped mirrors, which in turn allow for simple and efficient recompression using few-tens of milimetres bulk material alone or in combination with chirped mirrors. The beam diameter can be adjusted such as to avoid the intensity-dependent nonlinear effects.

1.5.1 Schematic layout of PFS

The planned layout of the PFS system is schematically shown in Fig. 1.2. The "CPA pump chain" is dedicated for the development of the PFS pump laser at 1030 nm, while the "OPCPA chain" will amplify the ultrabroadband signal using nonlinear frequency mixing in OPA crystals when pumped at 515 nm (frequency doubled output of PFS pump source). The CPA-pump and OPCPA chains are optically synchronized via a common frontend. The output of the oscillator at the frontend is split into two parts; one part is coupled into a photonic crystal fiber (PCF) for

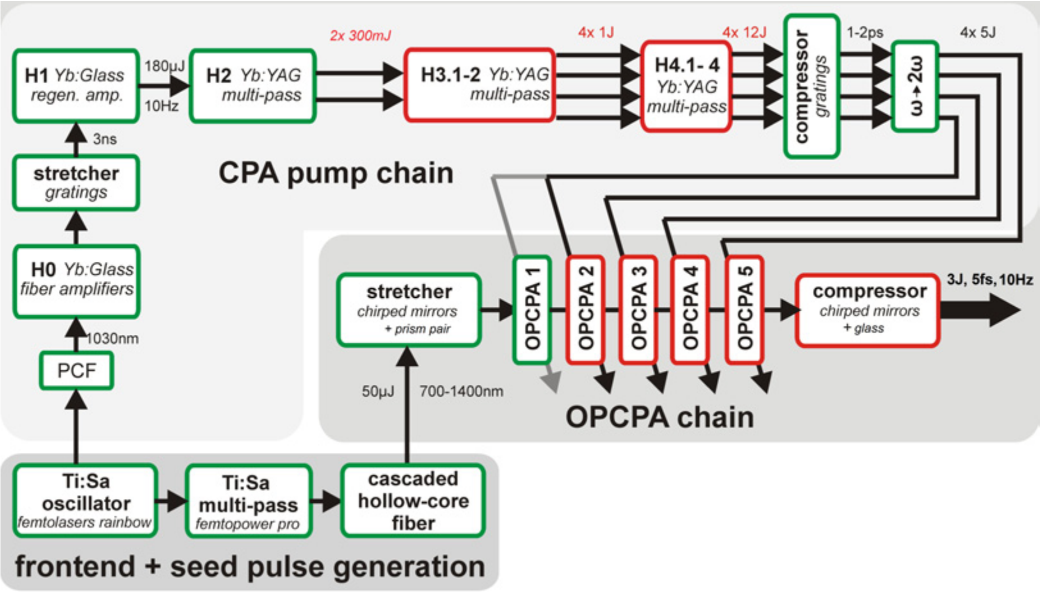
H1 Yb:Glass regen. amp.
180µJ
10Hz
H2 Yb:YAG multi-pass
2x 300mJ
H3.1-2 Yb:YAG multi-pass
4x 1J
4x 12J
H4.1- 4 Yb:YAG multi-pass
compressor gratings
1-2ps
ω→2ω
4x 5J
3ns
stretcher gratings
CPA pump chain
H0 Yb:Glass fiber amplifiers
1030nm
PCF
stretcher chirped mirrors + prism pair
OPCPA 1
OPCPA 2
OPCPA 3
OPCPA 4
OPCPA 5
compressor chirped mirrors + glass
3J, 5fs, 10Hz
50µJ
700-1400nm
OPCPA chain
Ti:Sa oscillator femtolasers rainbow
Ti:Sa multi-pass femtopower pro
cascaded hollow-core fiber
frontend + seed pulse generation

Figure 1.2: Planned layout of the PFS system.

spectral shifting to the pump laser wavelength of 1030 nm while the other is further amplified in a Ti:sapphire amplifier for broadband OPCPA seed generation. The spectrally shifted output of the PCF is pre-amplified in the Yb:doped fibers to boost the CPA-pump laser seed energy before injecting it into the pulse stretcher (discussed in Chapter 2). These stretched pulses are amplified in a chain of amplifiers (H_1–H_4) to deliver a total of ~50 J at 10 Hz in four beams with amplified spectrum supporting a pulse width of 1-2 ps. The amplified pulses are subsequently compressed and frequency doubled to pump the OPCPA chain at 515 nm.

The broadband OPCPA seed (700–1400 nm) is generated at the common frontend using a cascaded hollow core broadening technique (discussed in Chapter 4). The seed pulses are temporally stretched in a negative dispersion prism pair in order to match the pulse duration of the pump laser. These pulses are subsequently amplified in the OPCPA chain of 7-8 OPCPA stages (for clarity only 5 such stages are depicted in Fig. 1.2). The amplified pulses are recompressed in a bulk-material compressor.

1.6 Thesis outline

In this dissertation, the development of the common frontend for the PFS system is presented which provides optical synchronization between the OPCPA beam-line and the pump source using a state-of-the-art commercial Ti:sapphire oscillator-amplifier system. The design and development of a stretcher-compressor system for the CPA-based pump laser is detailed. A scheme for dispersion management of the broadband OPCPA seed pulses and first results of the short-pulse pumped OPCPA seeded by this frontend are presented. A short survey of the thesis structure is as follows:

- The seed generation for the CPA-chain of PFS system is discussed in Chapter 2. The design and development of the stretcher-compressor setup for the CPA-chain is presented. Different aspects which can affect the pulse quality of the stretched and recompressed pulse are highlighted. The results of compression of the amplified stretched pulses are also summarized.

- The experimental setup for amplification of the part of the oscillator spectrum dedicated for OPCPA-seed generation is presented in Chapter 3. Theoretical calculations of the dispersion introduced by a paired double-prism compressor are presented. The limitations of pulse compression using the prism compressor are discussed. A hybrid pulse compression technique is demonstrated to cope with these challenges. Moreover an alternative technique for the compression of TW-level pulses using a novel high-dispersive-mirror compressor is presented, providing remarkable simplifications in dispersion management.

- Different methods for broadband OPCPA seed generation in the spectral range of 700–1400 nm are discussed in Chapter 4. A scheme of idler generations using noncollinear OPA is described. The results of theoretical calculations for idler generation are presented. A technique of angular chirp compensation is discussed. The preliminary results of the experimental setup for idler generation are discussed. The schemes of cascaded spectral broadening using HCF-filamentation and cascaded-HCF for broadband supercontinumm generation are detailed. The NIR-parts of such spectra are then analysed for seeding the OPCPA chain of PFS. The dependence of gas-pressure and input pulse-energy on the infrared part of the supercontinuum is discussed. A new kind of double-angle chirped mirrors are introduced for few-cycle pulse generation. Moreover, the design of the OPCPA seed stretcher and compressor is presented.

- Measurement of the level of temporal synchronization between the OPCPA pump and signal is described in Chapter 5. Theoretical calculations of the temporal jitter introduced by the beam pointing fluctuations in the stretcher-compressor setup of the CPA-chain are presented. The proof-of-principle experiments for broadband parametric amplification in thin DKDP performed at the first stage of the PFS OPCPA chain are presented.

- The summary of the results is presented in Chapter 6.

Chapter 2

Seed generation and stretcher-compressor setup for the CPA pump laser

In this chapter a scheme for seed generation for the CPA pump-laser chain of the PFS system (cf. Fig. 1.2) is discussed. The design and development of a stretcher-compressor setup for the CPA chain is presented. Different aspects such as grating alignment sensitivity and angle of incidence which can affect the pulse quality of the stretched and recompressed pulses in the sretcher and compressor are also summarized.

2.1 CPA pump laser seed generation

As discussed in Chapter 1, the ps-pumped OPCPA requires very precise temporal synchronization between the pump laser and OPCPA pulses. This requirement in case of the PFS is fulfilled by deriving the seed pulses, both for CPA-pump laser chain and OPCPA chain, from a common source. The CPA-pump chain, which utilizes the Yb-doped gain media, requires seeding at 1030 nm owing to its laser emission at this wavelength [2, 74]. The OPCPA using DKDP crystals, on the other hand, requires a broadband seed ranging from 700 nm to 1400 nm. An ideal potential seed source for the PFS would be an octave spanning oscillator emitting in the design spectral ranges of the pump laser and OPCPA. However, such a source does not exist owing to the unavailability of a broadband gain medium in this spectral range. We used a commercial Ti:sapphire oscillator (Rainbow, Femtolasers GmbH) to serve as the master oscillator (MO) for the PFS frontend. It delivers nJ-scale pulses of < 7 fs duration at a repetition rate of 70 MHz with most of the output spectral energy ranging from a wavelength of 620 nm to 950 nm. The output contains only sub-pJ energy pulses within the bandwidth of our ps-scale amplifiers for the CPA-pump chain. Such an energy is not enough for efficient competing with the amplified spontaneous emission (ASE) in the high-gain regime, hence reducing the temporal contrast of the amplified pulses [76, 77]. One solution for avoiding such undesired effects is to use high energy seed pulses [77].

In order to obtain energetic seed pulses for the CPA-based pump laser chain of the PFS from a part of the output power of the master oscillator (MO), we employed a spectral shifting scheme based on soliton self-frequency shift (SSFS) [78] in a photonic crystal fiber (PCF) [51, 78, 79]. This scheme is considered more efficient as compared to the spectral broadening techniques based on self-phase modulation [80] at such small pulse energies. The SSFS in a PCF originates from the intrapulse stimulated Raman scattering, which transfers the high-frequency, or short-wavelength, part of the pulse spectrum to the low frequency, or long wavelength. Optical soliton pulses generally experience a continuous downshift of their carrier frequencies when they are propagating in a PCF with anomalous group velocity dispersion (GVD < 0) [81, 82]. The PCF substantially enhances this nonlinear optical process [83] due to a strong field confinement in a small-size fiber core and the possibility to tailor dispersion of guided modes by varying the fiber structure [84]. Moreover by varying the input energy and the length of the PCF, central wavelength of the red-shifted spectrum can be fine tuned. As discussed by Serebryannikov et al. [85], the radiation energy carried by the soliton is localized in the time domain within a short spike which, during its propagation through the fiber, dominates the main temporal envelope of radiation intensity. Owing to the anomalous group-velocity dispersion of the PCF, the red-shifted soliton becomes delayed and eventually isolated, both spectrally and temporally, with respect to the rest of the pump field. This isolation of the frequency-shifted soliton suppresses the interference between the solitonic part and the rest of the spectrum of radiation field. In this way the output red-shifted spectrum is significantly less modulated, making it better suited for seeding the amplifiers.

The schematic sketch of the experimental setup is shown in Fig. 2.1(a). The output of the MO was divided into two parts using a broadband beam splitter (BS). One part is utilized for OPCPA seed generation, the details of which are presented in next chapters. The other part of the MO output (100 mW, 1.4 nJ) was focused by a 0.25 numerical-aperture microscope objective (see Fig. 2.1(b)) into a 1.6-μm core diameter 25-cm long PCF (NL-PM-750 PCF; Crystal Fibre Ltd.) mounted on a very stable 3-D translation stage (Nano Max-313, Thorlabs) for spectral shifting at the CPA-pump laser wavelength of 1030 nm. Very fine displacement of the PCF entrance along the beam propagation axis, which in turn changes the coupling into the fiber, helps in fine-tuning the central wavelength of the soliton spectrum. Under optimum conditions an overall thoughput of $\sim 30\%$ was observed after the PCF with a broadband supercontinuum shown in grey shaded area in Fig. 2.1(c). An interference filter selected a $\Delta\lambda = 10$ nm band centred at 1030 nm from the frequency shifted spectrum after the PCF yielding about 3.4 pJ pulse energy after the filter. In order to ensure a stable PCF output spectrum at 1030 nm, an active fiber alignment system (APT

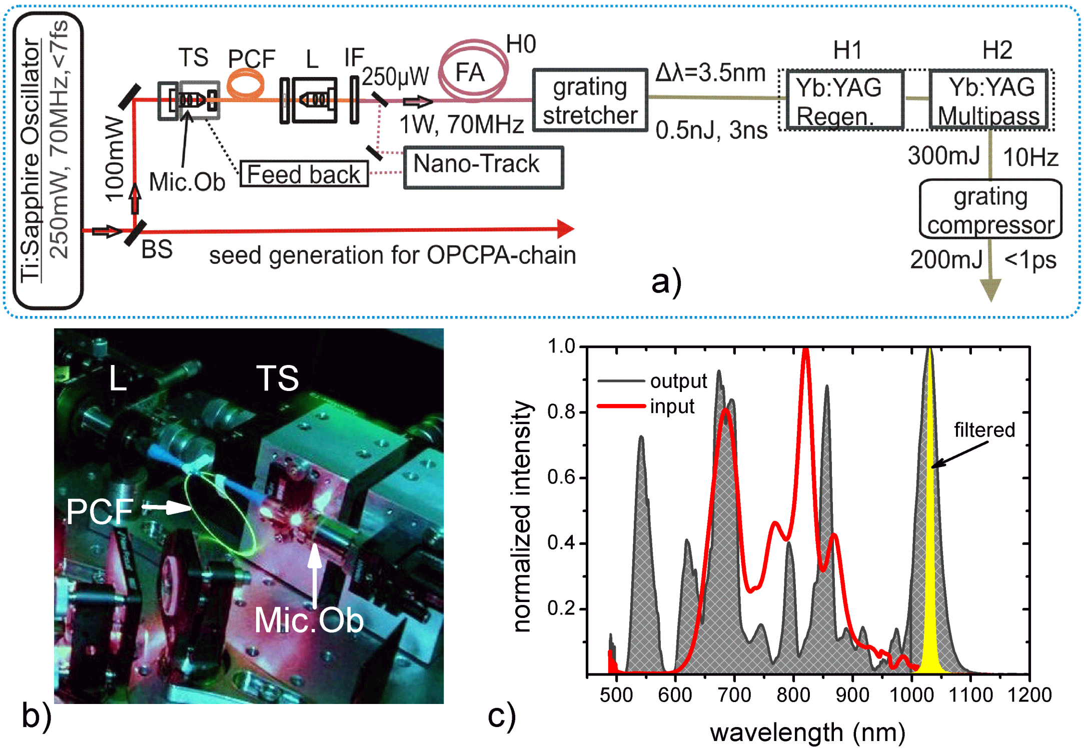
Ti:Sapphire Oscillator
250mW, 70MHz, <7fs
100mW
BS
TS
PCF
L
IF
Mic.Ob
Feed back
250µW
FA
H0
1W, 70MHz
Nano-Track
grating stretcher
Δλ=3.5nm
0.5nJ, 3ns
H1
Yb:YAG Regen.
H2
Yb:YAG Multipass
300mJ
10Hz
grating compressor
200mJ
<1ps
seed generation for OPCPA-chain
a)
L
TS
PCF
Mic.Ob
b)
c)
normalized intensity
1.0
0.8
0.6
0.4
0.2
output
input
filtered
500
600
700
800
900
1000
1100
1200
wavelength (nm)

Figure 2.1: (a) Schematic layout of the experimental setup. BS: beam splitter; Mic.Ob: microscopic objective; PCF: photonic crystal fiber; TS: 3D-translation stage; L: lens; IF: interference filter; FA: fiber amplifiers; Regen.: regenerative amplifier; H0, H1 and H2 are according to the schematic layout of the PFS shown in Fig. 1.2. (b) Picture of the apparatus used for spectral shifting at 1030 nm. (c) Input and output spectra of the PCF. The filled area highlighted in yellow indicates the 10-nm FWHM band spectrum after an interference filter. All the spectra are normalized to their peak values.

Nano-Track BNT001, Thorlabs) was used. Such a stabilization is needed to avoid the beam pointing fluctuation at the entrance of PCF due to a thermal drift in the laser cavity which in turn causes a change in the power as well as spectrum at the exit of the PCF. This system provides 2-D stabilizing of beam pointing in a plane vertical to the beam propagation direction by keeping the fiber throughput power at maximum. The output after the interference filter was coupled into a two stage Yb-doped fiber amplifier pumped at 976 nm (designed by the Institute for Applied Physics, Jena, Germany) delivering $>$ 14 nJ in a spectral bandwidth $\sim$10 nm (FHWM) centred at 1030 nm at 70 MHz. These pre-amplified pulses were then fed into an all-reflective grating stretcher (see next section) in order to stretch them in time up to $>$ 3 ns with spectral FWHM of 3.5 nm centred at 1030 nm for damage-free amplification in the CPA chain. This reduced spectrum of FWHM 3.5 nm is defined by the gain bandwidth of the subsequent amplifiers of the CPA pump laser chain [71, 72]. The dispersion calculations and design of the stretcher compressor setup for the CPA pump laser are presented in the following section.

2.2 Stretcher compressor setup for CPA pump laser chain

2.2.1 Dispersion calculations

In order to stretch the $\sim$ 3.5-nm (FWHM of spectral intensity) seed pulse for the CPA-chain of the PFS system, a modified all-reflective grating stretcher [86] was designed. It is based on the principle of conventional Martinez-type grating stretcher [46] which comprises a pair of gratings, a 1:1-imaging telescope, and an end mirror as shown in Fig. 2.2. In this setup each beam leaving the first grating (grating1) with an angle β is sent on the second grating (grating2) with an incidence angle $\beta' = -\beta$ by a 1:1 imaging telescope. Therefore all the spectral components are diffracted at the same angle $-\alpha$ from the second grating. In this way the redder spectral components (compared to the central wavelength) of the pulse travel shorter or longer optical paths between the gratings, depending on the position of the grating2, than the bluer ones, introducing a wavelength-dependent delay. Moreover in this configuration the image of the grating1 and grating2 through the telescope forms a Treacy-type grating compressor [45], for identical angle of incidence and spectral range, with separation $L_1 = f_1 - z_1$ along the central wavelength λ_0. The dispersion introduced by such a stretcher therefore matches with that of the Treacy-type grating compressor [87, 88].

The frequency dependent spectral phase of a frequency component ω after a Martinez-type stretcher can be written as [46, 89]

$$\Phi(\omega) = X\frac{\omega}{c} \cdot \ell \cos(\beta - \beta_0), \tag{2.1}$$

where $\ell = (z_1 - f_1)M^2 + (z_2 - f_2)$; z_1 and z_2 are the distances of respective gratings from the principle planes of the telescope lenses as shown in Fig. 2.2; $M = \frac{f_2}{f_1}$ is the magnification factor of the imaging telescope, equal to one in our consideration; X denotes the number of passes of the incident pulse through the stretcher, e.g. equal to two in Fig. 2.2; β and β_0 are the first-order diffraction angles from a grating corresponding to an angle of incidence of α for the wavelength components λ $(= 2\pi c/\omega)$ and λ_0 as given by

$$\beta = \arcsin(N\lambda - \sin\alpha), \tag{2.2}$$

and

$$\beta_0 = \arcsin(N\lambda_0 - \sin\alpha), \tag{2.3}$$

where N denotes the line density (lines/mm) of the diffraction grating.

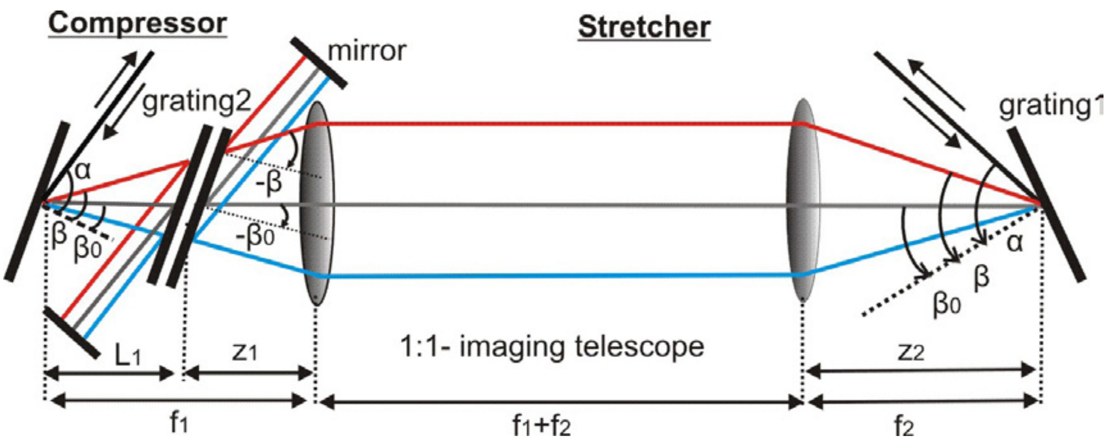

Figure 2.2: Principle of a grating-based stretcher compressor setup with matched dispersion. The right hand side of the picture denotes a Martinez-type stretcher [46] where each beam leaving the grating1 with an angle β is sent on the grating2 with an incidence angle $\beta' = -\beta$ by a 1:1 imaging telescope. Therefore all the spectral components are diffracted at the same angle $-\alpha$ from the second grating. The end mirror redirects the beam to fold the optical path. The image of the two gratings forms a Treacy-type parallel grating compressor [45] (left hand side of the picture) with matched dispersion for a grating separation $\mathrm{L}_1 = f_1 - z_1$ along λ_0 [87]. Here for clarity the imaging system is shown with lenses instead of mirrors as for our real design.

The spectral phase of a frequency component ω can be expanded around the central frequency $\omega_0 = 2\pi c/\lambda_0$ using the Taylor series as follows

$$\begin{aligned}\Phi(\omega) &= \Phi(\omega_0) + \frac{(\omega-\omega_0)}{1!}\cdot\left.\frac{\partial\Phi}{\partial\omega}\right|_{\omega=\omega_0} + \frac{(\omega-\omega_0)^2}{2!}\cdot\left.\frac{\partial^2\Phi}{\partial\omega^2}\right|_{\omega=\omega_0} + \frac{(\omega-\omega_0)^3}{3!}\cdot\left.\frac{\partial^3\Phi}{\partial\omega^3}\right|_{\omega=\omega_0} + \cdots \\ &= \Phi(\omega_0) + \frac{(\omega-\omega_0)}{1!}\cdot D_1 + \frac{(\omega-\omega_0)^2}{2!}\cdot D_2 + \frac{(\omega-\omega_0)^3}{3!}\cdot D_3 + \cdots\end{aligned} \tag{2.4}$$

The coefficients $D_1 = \left.\frac{\partial\Phi}{\partial\omega}\right|_{\omega=\omega_0}$, $D_2 = \left.\frac{\partial^2\Phi}{\partial\omega^2}\right|_{\omega=\omega_0}$, $D_3 = \left.\frac{\partial^3\Phi}{\partial\omega^3}\right|_{\omega=\omega_0}$ are termed as group-delay (GD), group-delay dispersion (GDD), and third-order dispersion (TOD), respectively. The expression (Eq. 2.4) can be expanded to higher order terms, however we assume that for the spectral bandwidth of our setup the influence of those terms on the pulse duration will be negligible. Differentiating Eq. 2.1 with respect to ω up to three orders we have

$$\frac{\partial\Phi(\omega)}{\partial\omega} = X\frac{\ell}{c}\cdot\left[\cos(\beta-\beta_0) - \omega\sin(\beta-\beta_0)\frac{d\beta}{d\omega}\right] \tag{2.5}$$

$$\frac{\partial^2\Phi(\omega)}{\partial\omega^2} = -X\frac{\ell}{c}\cdot\left[\left(2\frac{d\beta}{d\omega} + \omega\frac{d^2\beta}{d\omega^2}\right)\sin(\beta-\beta_0) + \omega\left(\frac{d\beta}{d\omega}\right)^2\cos(\beta-\beta_0)\right] \tag{2.6}$$

$$\begin{aligned}\frac{\partial^3\Phi(\omega)}{\partial\omega^3} =& -3X\frac{\ell}{c}\left(\frac{d\beta}{d\omega}\right)^2\left(1+\omega\,\frac{d^2\beta}{d\omega^2}\Big/\frac{d\beta}{d\omega}\right)\cos(\beta-\beta_0)\\ &-X\frac{\ell}{c}\left(3\frac{d^2\beta}{d\omega^2}+\omega\frac{d^3\beta}{d\omega^3}-\omega\left(\frac{d\beta}{d\omega}\right)^3\right)\sin(\beta-\beta_0)\end{aligned} \tag{2.7}$$

Simplifying Eqs. 2.5– 2.7 for $\frac{d\beta}{d\omega}=\frac{-2\pi cN}{\omega^2\cos\beta}$ and $\frac{d^2\beta}{d\omega^2}=\frac{4\pi cN}{\omega^3\cos\beta}\left(1+\frac{\pi cN\sin\beta}{\omega\cos^2\beta}\right)$ (cf. Eq. 2.2) under condition of $\omega\rightarrow\omega_0$ we obtain

$$D_1 = X\cdot\frac{\ell}{c} \tag{2.8}$$

$$D_2 = -X\cdot\frac{\ell}{c}\cdot\frac{\lambda_0}{2\pi c}\left(\frac{\lambda_0 N}{\cos\beta_0}\right)^2 \tag{2.9}$$

$$D_3 = 3X\cdot\frac{\ell}{c}\cdot\left(\frac{\lambda_0}{2\pi c}\right)^2\left(\frac{\lambda_0 N}{\cos\beta_0}\right)^2\left(1+\frac{\lambda_0 N\sin\beta_0}{\cos^2\beta_0}\right) \tag{2.10}$$

By assuming a Gaussian spectrum of the input pulse, following expression can be used for the estimation of required GDD for stretching a nearly transform limited (TL) pulse τ_0 to the desired FWHM pulse duration of $\Delta\tau$ [88]

$$GDD = \frac{\Delta\tau_0}{4\ln 2}\sqrt{\Delta\tau^2-\Delta\tau_0^2} \tag{2.11}$$

where $\Delta\tau_0=\frac{2\ln 2}{\pi c}\frac{\lambda_0^2}{\Delta\lambda}$ and $\Delta\lambda$ is the FWHM of the Gaussian shaped spectrum. In order to stretch the seed pulse from $\Delta\tau_0 = 560$ fs, as calculated from the Gaussian spectrum assuming a FWHM of 3 nm, to the desired pulse duration of 3 ns, the estimated GDD amounts to $+6.14\times10^8$ fs^2. As can be visualized from Eq. 2.9, a Martinez-type stretcher can provide both normal and anomalous dispersions depending on the sign of ℓ whether it is negative or positive, respectively. However, in order to employ a Treacy-type parallel grating pair compressor, which provides anomalous dispersion, the effective distance ℓ for the stretcher should be negative to get opposite sign of the dispersion.

Figures 2.3(a) and (b) show the GDD introduced by the pulse stretcher as a function of the parameters ℓ and α at $\lambda_0 = 1030$ nm. The calculations have been performed for a Martinez-stretcher configured in a double-pass (X=2) arrangement using a pair of N=1740-lines/mm diffraction gratings and an M=1 imaging telescope (Fig. 2.2). The GDD introduced by the stretcher varies linearly with respect to the effective length ℓ (Eq. 2.9), however it also depends very sensitively on the angle of incidence (Figs. 2.3(a,b)). The dependence of calculated GDD for three different values of α is shown in Fig. 2.3(a). The slope of the GDD changes from neary $+1\times10^8$ fs^2/m to $+6.24\times10^7$ fs^2/m for a change in α from 58.5° to 63° (see more details in Table 2.1). Therefore, significant accuracy of the angle of incidence and grating separations would be required for attaining a matched dispersion for the stretcher-compressor pair. For example a deviation of nearly 0.15° $\approx$ 2.6 mrad in the angle of incidence in the stretcher or compressor

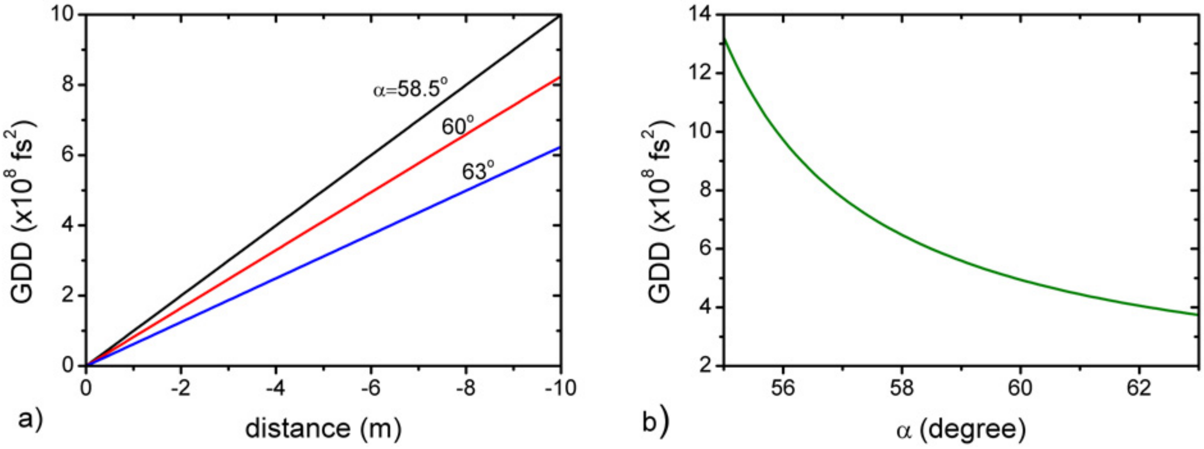

Figure 2.3: Calculated GDD introduced by the Martinez-stretcher [46] set up for a double-pass (X=2) configuration using N=1740-lines/mm diffraction gratings and M=1 imaging telescope (Fig. 2.2). (a) Dependence of GDD on effective distance ℓ for $\alpha = 58.5°$, $60°$, and $63°$. (b) Calculated GDD as a function of α for a fixed value of ℓ of 6 m (cf. Eqs. 2.3, 2.9).

from an angle of 58.5° and a stretching/compression ratio of ≈ 5000 results in an uncompensated GDD of $\pm 1.28 \times 10^7$ fs^2, and TOD of $\mp 6.39 \times 10^{10}$ fs^3, which can change a pulse, given the parameters of our setup, upto two orders of magnitude compared to its TL width. Here the residual GDD is corrected by changing the grating separation, whereas the TOD and higher order terms will remain uncompensated. Moreover, different grating separation can provide the same stretching factor at different α as elaborated in Fig. 2.4(a). In order to provide the design GDD of $+6.14 \times 10^8$ fs^2, the required distance ℓ for the stretcher increases from nearly -3 m to -10 m when α changes from $\sim 55°$ to $63°$. These results favour small angle of incidence for incoming beam in order to construct a compact stretcher and compressor setup. However the diffraction efficiency of the grating which, dominantly, defines the overall throughput of the setup changes in the opposite way. It exhibits maximum diffraction efficiency in a specific diffraction-order near the Littrow angle and less elsewhere. As can be seen from Fig. 2.3(b), the measured first-order diffraction efficiency for our available N=1740-lines/mm multilayer diffraction (MLD) grating [90] for a p-polarized light reduces from $\sim 94\%$ to 82%with a decrease of 11° in the angle of incidence from its Littrow angle of $\sim 63°$ at 1030 nm.

We employed an optimum angle of incident of 58.5°, keeping in view both the diffraction efficiency of the gratings as well as the available space in the lab, for our stretcher and compressor setup which corresponds to an effective distance ℓ of -6.1 m in the stretcher for double pass (X=2) configuration (Fig. 2.2). The equivalent distance L_1 along λ_0 in the compressor, assuming negligible dispersion from the amplifier materials, would also be 6.1 m (Fig. 2.2). The available

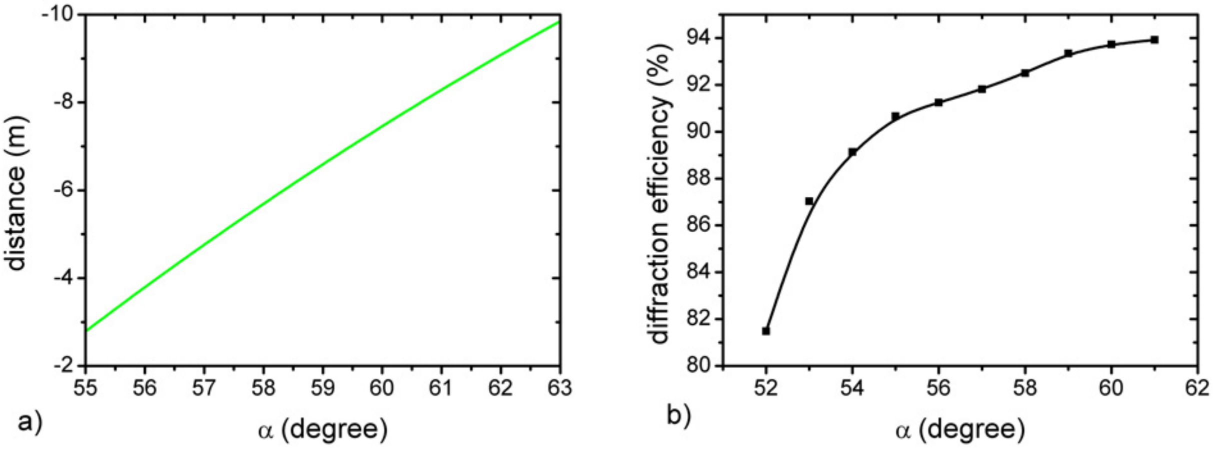

Figure 2.4: (a) The dependence of distance ℓ on the angle of incidence (α) (cf. Eqs. 2.1, 2.9), for introducing a GDD of $+6.14 \times 10^8$ fs^2 at $\lambda_0 = 1030$ nm, in a Martinez stretcher set up for a double-pass (X=2) configuration using N=1740-lines/mm diffraction gratings and M=1 imaging telescope (Fig. 2.2). (b) Measured first-order diffraction efficiency of the gratings, used in the experimental setup, at different values of α.

gratings exhibit a diffraction efficiency of $\sim 93.9\%$ at this angle of incident for p-polarized light. In the following the design of our modified all-reflective grating stretcher is presented.

2.2.2 Ray trace for the stretcher

Figure 2.5 shows the beam propagation through our stretcher in the horizontal (xz) as well as vertical (yz) planes, with the z-axis being the propagation direction, as drafted using a ray-tracing program RAYTRACE [91]. It consists of a single grating, a spherical mirror, a flat mirror and two roof mirrors. The spherical and flat mirrors form a 1:1 imaging telescope, whereas the roof mirrors RM$_1$ and RM$_2$ provide two-times folding (X=4) geometry. A 200×100-mm^2 grating with N=1740 lines/mm was considered for ray tracing. A half-inch flat mirror (M$_1$) steers the incoming beam, having a 1/e^2 diameter of ~6 mm, to the grating (G) which diffracts it towards a 4-inch planoconcave mirror (FM) with a focal length of 2.65 m. The beam is then focused, by changing its height slightly above the grating, on a 4-inch flat mirror M$_2$ positioned at the focal plane of FM. A small tilt of $\sim 0.4^\circ$ of the FM in the vertical plane is enough to guide the beam toward the flat mirror and avoiding beam clipping on the grating. This mirror redirects the beam back to the FM to repeat this sequence in reverse order but at slightly different height. The beam exits the stretcher assembly after the first pass vertically displaced from the incoming beam. At this point, it is sent back for a second pass through the stretcher by a roof mirror RM$_1$, displaced vertically downwards by ~10 mm. After the second pass the output beam is again

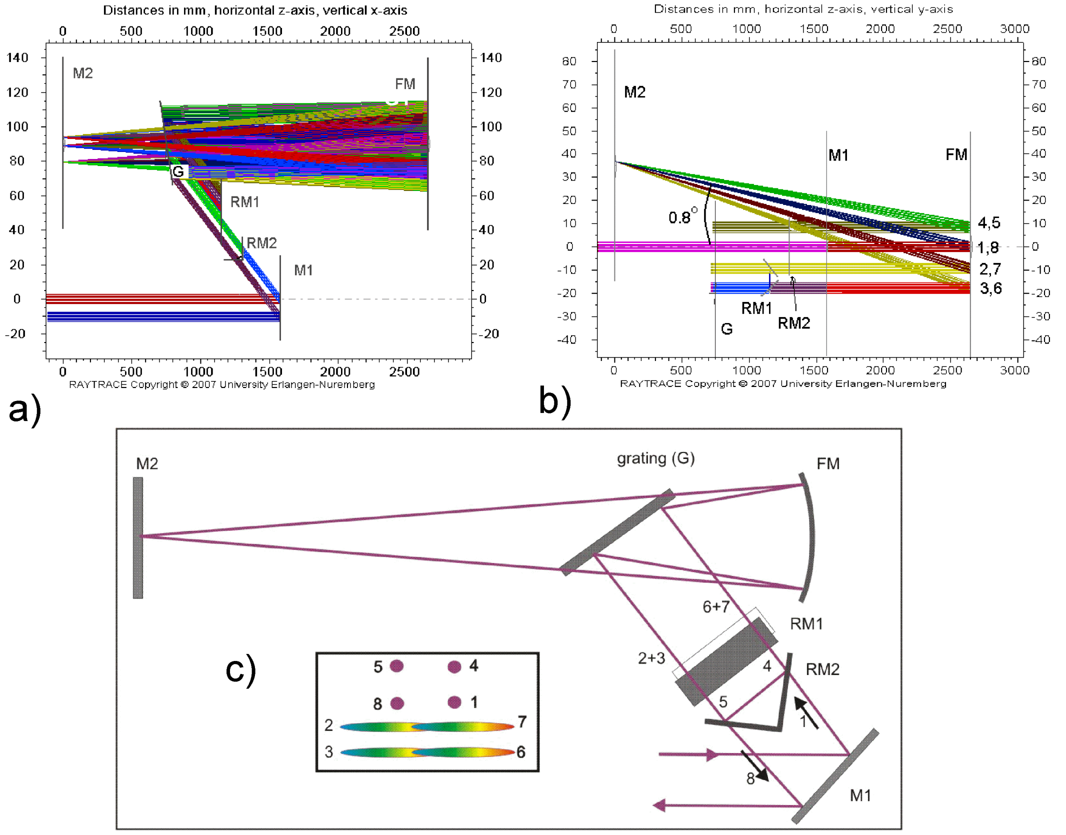
Distances in mm, horizontal z-axis, vertical x-axis
M2
FM
G
RM1
RM2
M1
RAYTRACE Copyright © 2007 University Erlangen-Nuremberg
a)
Distances in mm, horizontal z-axis, vertical y-axis
M2
M1
FM
0.8°
4,5
1,8
2,7
3,6
RM1
RM2
G
RAYTRACE Copyright © 2007 University Erlangen-Nuremberg
b)
M2
grating (G)
FM
6+7
RM1
2+3
4
RM2
5
1
8
M1
c)
5
4
8
1
2
7
3
6

Figure 2.5: The schematic layout of the CPA-seed stretcher with 4-times folding geometry, i.e. eight reflections off the grating as sketched by an optical ray-tracing software: RAYTRACE [91]. (a) Beam propagation in the xz-plane. (b) Beam propagation in the yz plane, where xz and yz denote the horizontal and vertical planes w.r.t the direction of propagation z of the beam. The sharp display of different optical components in (a) and (b) is due to the limitation of the RAYTRACE to resolve their orientations appropriately. The colour scheme of the RAYTRACE is such that for each optical element the incident and reflected ray is displayed with a different colour. (c) Top view of the stretcher: for illustration only the central wavelength (λ_0) is shown. The inset of c) shows the beam position on the grating surface after each pass. RM1: roof mirror for vertical displacement of spectrally dispersed beam; RM2: roof mirror (or retroreflector) for horizontal displacement; M1, M2: flat mirrors.

Table 2.1: Calculated coefficients of dispersion per unit effect grating separation (ℓ) in a Martinez-type stretcher at different angles of incidence (α) for X=2, N=1740 lines/mm and M=1 (Eqs. 2.9, 2.10):

α [degree]	GDD/ℓ [fs^2/m]	TOD/ℓ [fs^3/m]	ℓ for 6.14×10^8 fs^2 [m]
58	1.08×10^8	-2.93×10^9	-5.69
58.5	1.00×10^8	-2.51×10^9	-6.14
59	9.32×10^8	-2.19×10^9	-6.59
60	8.24×10^8	-1.71×10^9	-7.45
61	7.41×10^7	-1.38×10^9	-8.28
62	6.76×10^7	-1.15×10^9	-9.08
63	6.24×10^7	-9.82×10^8	-9.84

displaced in the vertical direction from the input, but to the opposite side as the first pass, which is then redirected to the stretcher for two more passes by a second roof mirror RM$_2$, horizontally displaced by $\sim$10 mm. After 8 passes the beam exits the stretcher assembly displaced in the horizontal direction.

The required distance ℓ in the described setup with two times folding geometry (X=4), for providing the design GDD of $+6.14 \times 10^8$ fs^2, is reduced to -3.05 m which correspond to $z_1 = z_2 = 1.8875$ m (Fig. 2.2) or a separation of 762.5 mm between the grating and the focal plane of the FM (Fig. 2.5(a)). The calculated TOD of the stretched pulse for this separation is -1.55×10^{10} fs^3 (Eq. 2.10).

As discussed in Chapter 1, the design of the PFS requires the stretched seed pulses, centred at 1030 nm, to be amplified to 50 J energy in a chain of CPA stages. This total energy of 50 J will be achieved in four beams each containing $\approx$ 12.5 J.[*] In the following a design of the pulse compressor is presented to re-compress the amplified stretched pulses.

2.2.3 Ray trace for the grating compressor

As described in the previous the section, a Treacy-type parallel grating pair can provide a dispersion matched with that of the Martinez-type stretcher. A separation of $L = 6.1$ m between the gratings along the wavelength component λ_0 is needed to provided a GDD of -6.14×10^8 fs^2 and a TOD of $+1.55 \times 10^{10}$ fs^3, as calculated from Eqs. 2.9 and 2.10 by substituting $|\ell| = -L$. The optical path of four beams through the compressor is shown Fig. 2.6. We adapt a diameter

---

[*] The design of these amplifiers is described in Ref. [2]. Additional details will be presented in the future PhD-dissertations of S. Klingebiel and C. Wandt, MPQ, Hans-Kopfermann Str.1, 85748, Garching, Germany

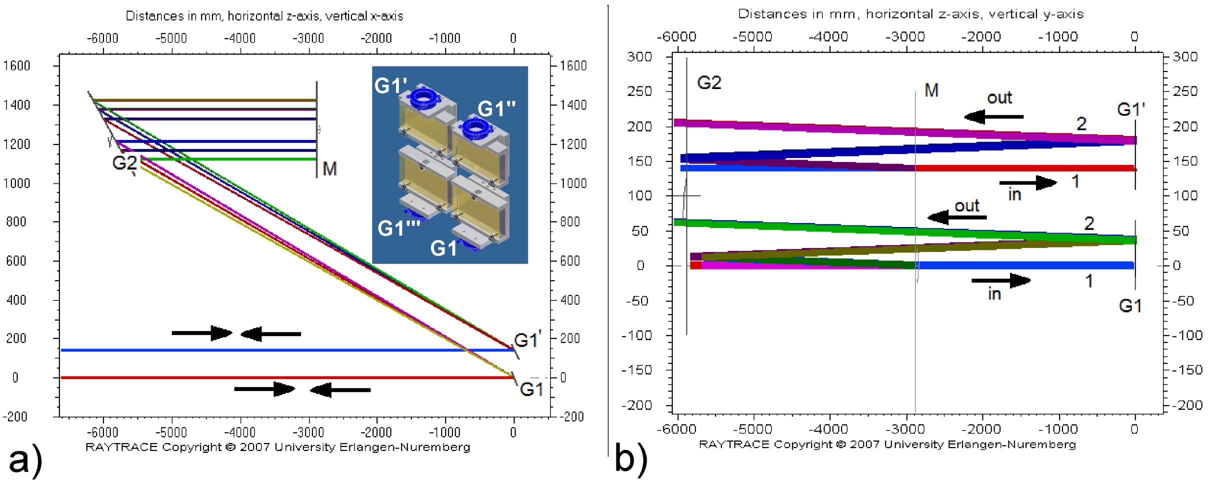
Distances in mm, horizontal z-axis, vertical x-axis
-6000
-5000
-4000
-3000
-2000
-1000
0
1600
1400
1200
1000
800
600
400
200
0
-200
G1'
G1"
G1'''
G1
G2
M
G1'
G1
RAYTRACE Copyright © 2007 University Erlangen-Nuremberg
a)
Distances in mm, horizontal z-axis, vertical y-axis
300
250
200
150
100
50
0
-50
-100
-150
-200
G2
M
out
in
out
in
1
2
2
1
G1'
G1
RAYTRACE Copyright © 2007 University Erlangen-Nuremberg
b)

Figure 2.6: The schematic layout of the CPA pulse compressor sketched by an optical ray-tracing software: RAYTRACE [91]. (a) Beam propagation in the xz-plane. (b) Beam propagation in the yz plane, where xz and yz denote the horizontal and vertical planes w.r.t the direction of propagation z of the beam. The inset in (a) depicts the designed assembly of four gratings at z=0 for four incident beams.

of $\sim$40 mm for the incident flat-top beams, equivalent to an energy fluence of < 1 J/cm^2 well below the reported damage threshold of 3-5 J/cm^2 for the MLD gratings [90, 92] for the parameters similar to the PFS pump laser. However, for clarity a beam diameter of 10 mm is depicted in Fig. 2.6. The incoming beams propagate along the z-axis with their centres displaced from each other by $\sim$140 mm in the xy-plane in the shape of a square. They strike on four separate 200×100-mm^2 gratings (denoted by G_1, G_1', G_1'', and G_1''') at z=0 arranged in the xy-plane in a fashion similar to the incoming beams with their edges having an offset of $\sim$ 40 mm from each other, see Fig. 2.6(a). After diffraction, all the beams impinge on a 800×400-mm^2 grating (G_2) separated by 6.1 m along the wavelength component $\lambda_0 = 1030$ nm in the xz-plane, which diffracts them towards a 500-mm diameter end mirror (M). This mirror redirects these beams to repeat the sequence in reverse direction for the second pass. At this position the beams are slightly tilted by $< 0.2^\circ$ in the upward direction (along the y-axis) in order to separate each beam from the incoming ones at the exit of the compressor (cf. Fig. 2.6(b)).

2.2.4 Alignment sensitivity

The grating-based stretcher and compressor pairs are very sensitive to the alignment. Slight mismatch of the angle of incidence or little difference of the effective grating separation from the designed values may lead to an uncompensated GDD, TOD and higher order dispersion, hence leaving an uncorrected spectral phase of the amplified pulses at the exit of the compressor.

Moreover even with the exact design, the material dispersion of the in-between laser amplifiers restricts the exact compensation of all orders of dispersion coefficients. The grating separation in the stretcher or compressor is slightly detuned to accommodate this extra dispersion in the setup. However owing to a mismatch between the TOD and higher-order dispersion coefficients of the material and that of the grating compressor, this single degree-of-freedom can only compensate additional GDD of the amplifier material. In order to correct the residual TOD, simultaneous tuning of both the grating separation as well as angle of incidence is required for getting close to the TL pulse duration after the compressor as shown in Fig. 2.7. Here, the zero values of ΔL and ΔD_3 correspond to the design angle of 58.5° at $L \approx 6$ m in the compressor for a GDD (or D_2) of -6×10^8 fs^2 and a TOD (or D_3) of $+1.5\times10^{10}$ fs^3 at $\lambda_0 = 1030$ nm (cf. Eq. 2.9, 2.10). As can be seen from this figure, changing the angle of incidence, for example, by $+0.02°$ and increasing the grating separation L in the compressor by ≈ 20 mm, an additional amount of TOD of $\Delta D_3 \approx -5\times10^7$ fs^3 can be obtained while keeping the GDD of -6×10^8 fs^2 unchanged. In this way an equivalent amount of TOD resulting from the alignment error or material dispersion can be corrected. The coefficients of uncompensated spectral phase after the compressor can be measured with substantial accuracy by some conventional techniques, such as Frequency Resolved Optical Gating (FROG [93]) or Spectral Phase Interferometry for Direct Electric-field Reconstruction (SPIDER [94]), hence this technique can provide correction of phase up to third-

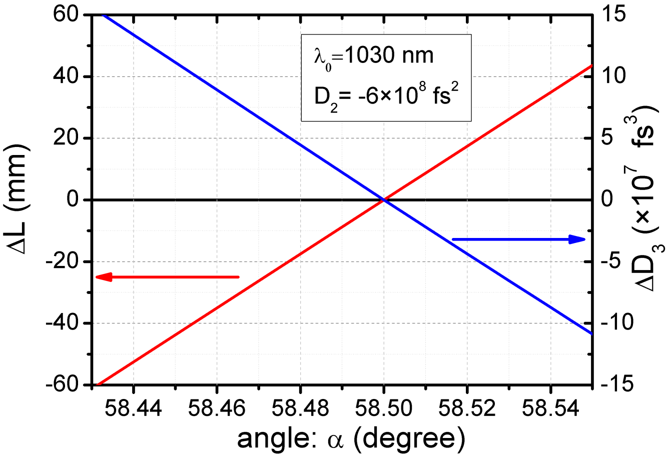

Figure 2.7: A scheme for compensating the extra TOD (ΔD_3) of the chirped amplified pulse resulting from the material dispersion of the amplifiers or incidence angle mismatch between the stretcher and compressor. The zero values of ΔL and ΔD_3 correspond to the design angle of 58.5° at $L \approx 6$ m in the compressor for a GDD (or D_2) of -6×10^8 fs^2 and a TOD (or D_3) of $+1.5\times10^{10}$ fs^3 at $\lambda_0 = 1030$ nm. By simultaneous tuning of the grating separation and angle of incidence in the compressor, ΔD_3 can be counterbalanced while keeping the GDD unchanged.

order coefficient of dispersion (D_3).

The grating compressor is also extremely sensitive to any relative angle between the gratings. For any non-zero relative angle of ξ_x between the gratings within their dispersion planes, i.e. around an axis (x) parallel to their grooves, the angular dispersion produced by the first grating is not fully compensated by the second one. This effect results in an angular spread $\theta(\lambda)$ of different wavelength components in the dispersion plane hence constituting a net angular chirp $C_{a,x}$ at the exit of the setup [95] given by

$$C_{a,x} = \left|\frac{d\theta(\lambda)}{d\lambda}\right|_{\lambda=\lambda_0} = \left|2\,\xi_x N \frac{\tan\beta_0}{\cos\alpha}\right|. \tag{2.12}$$

Moreover this alignment error induces a change ΔL_x in the grating separation over the cross-section of the beam, thereby resulting in a varying pulse duration in this plane. This effect for a pulse with Gaussian spectrum of width $\Delta\lambda$ can be calculated as follows [95]

$$\Delta\tau_x = \Delta\tau_0\sqrt{1+\left(\frac{\pi}{\ln 2}\frac{N^2(\Delta\lambda)^2}{\lambda_0(\cos\beta_0)^2}\cdot\Delta L_x\right)^2}, \tag{2.13}$$

where $\Delta L_x = \xi_x \frac{x-x_o}{\cos\alpha\cos\beta_0}$ and x is the transverse distance from a reference position x_0 over the beam. Although the single-grating stretcher (Fig. 2.5) with perfect imaging is, in principle, inherently free from the alignment error ξ_x [86], its output beam is still prone to the angular chirp if the folding mirror (M_2) is not precisely positioned at the focal plane of the focusing mirror (FM). If this mirror is misplaced from the focal point of the imaging element by a distance ξ_z, the incidence angles on the grating vary after each pass due to imperfect imaging from the telescope. Therefore the angular dispersion introduced by the first two-passes is not completely compensated by the third and fourth pass, and so on. The resulting angular chirp in the horizontal plane of the output beam after the stretcher due to this alignment error can be calculated using the Ref. [95] as

$$C_{a,x} \approx \left|2X\xi_z\frac{f-z_1}{f^2}\frac{N}{\cos\alpha}\right|, \tag{2.14}$$

where z_1 is the distance between the stretcher-grating and focusing mirror (see Fig. 2.2). In the near field, a slight angular wavelength chirp across the wave front will result in a pulse-front tilt, i.e. a tilt between the pulse front and a direction perpendicular to the beam propagation. A group delay component $\Delta T_g = \lambda_0\,(x_0 - x)\,C_{a,x}/c$ is introduced which varies transversely within the beam [95]. At the focus of the pulse (far field), the pulse will be both spatially and temporally larger than the one with no pulse-front tilt, resulting in a reduced peak intensity at focus. This effect for a laser pulse with a Gaussian intensity profile both spectrally and spatially with an assumption that the time-bandwidth product ($\Delta\lambda\Delta\tau$) is unaffected by the angular chirp can be calculated as [95]

$$\xi = \frac{\Delta\tau_F}{\Delta\tau_0} = \sqrt{1+\left(C_{a,x}\cdot\frac{\pi}{2\ln 2}\cdot\frac{\Delta\lambda}{\lambda_0}\cdot d_{FWHM}\right)^2}, \tag{2.15}$$

where $\Delta\tau_F$ is the pulse width of the focal spot, d_{FWHM} is the FWHM of the Gaussian intensity distribution in space. The elongated pulse duration and the enlarged focal spot produce a total intensity reduction in the focus center by a factor of ξ^2 [95]. Figs. 2.8 depict the severity of these effect in case of our setup. A misalignment angle of $\xi_x = 0.06^\circ \approx 1.0$ mrad, or $\xi_z = 7$ mm can produce an angular chirp of $C_{a,x} \approx 20$ μrad/nm, which can cause ≈ 4 times increase in the pulse duration and 16 times decrease in the peak intensity of the focal spot. The change in the pulse duration along the cross-section of spatial beam profile, for $x - x_0 = 25$ mm, is negligible. Therefore these facts demand a very high accuracy of grating alignment in the stretcher and compressor. One way to get such a high accuracy is to use an inverted-field autocorrelator [95] or a single-shot second-order autocorrelator [96] to correct the pulse front tilt of the beam at the exit of each setup. Under ideal conditions both the pulse front and phase front exhibit zero angle. The stretcher or compressor are, therefore, adjusted to correct the pulse front tilt across the entire beam.

In addition to the above discussed challenges another issue is the shot-to-shot beam pointing fluctuation inside the stretcher and compressor setups, mainly, arising from the air-turbulences or mechanical instabilities of the optomechanics . Our theoretical calculations, as will be presented in chapter 5, predict a significant pulse-to-pulse timing jitter, in terms of arrival time, of the compressed pulse after the compressor for μrad-scale fluctuations in beam pointing inside the stretcher or compressor. This timing fluctuation can affect the OPCPA gain for the design parameters of our setup, since the arrival time of the pump pulse changes from one pulse to the other relative to the OPCPA signal, hence requiring very stable optomechanics in the stretcher and compressor setups as well as isolation from air turbulences using airtight/vacuum enclosures.

2.2.5 Implementation of the stretcher and compressor

The fiber amplifier output pulses with a pulse energy of ~14 nJ and a FWHM spectral width of 10 nm were fed into the stretcher by maintaining a 1/e^2 beam diameter of 6 mm.[*] The assembly of different parts of the stretcher, discussed in Sec. 2.2.2, is shown in Figs. 2.9(a,b). Our designed optomechanics for the stretcher provide < 10 μm resolution for the translational motion and ~0.017° for the rotational motion. The incoming beam was guided into the stretcher by a mirror M$_1$. The N=1740-nm 200×100-mm^2 MLD grating [90] was aligned at an angle of incidence of 58.5° using the beam diffracted in the zeroth-order, however the first-order diffracted beam was adapted for the stretcher. Figure 2.9(c) shows the spectrum of the pulse at the input and output of the stretcher. The unused spectral components of the input pulse were cut in the stretcher to deliver a FWHM band of ~ 5 nm at the output. The width of the stretched pulse was

---

[*] The implementation of the stretcher-compressor setup was equally contributed by S. Klingebiel, MPQ, Hans-Kopfermann Str.1, 85748, Garching, Germany.

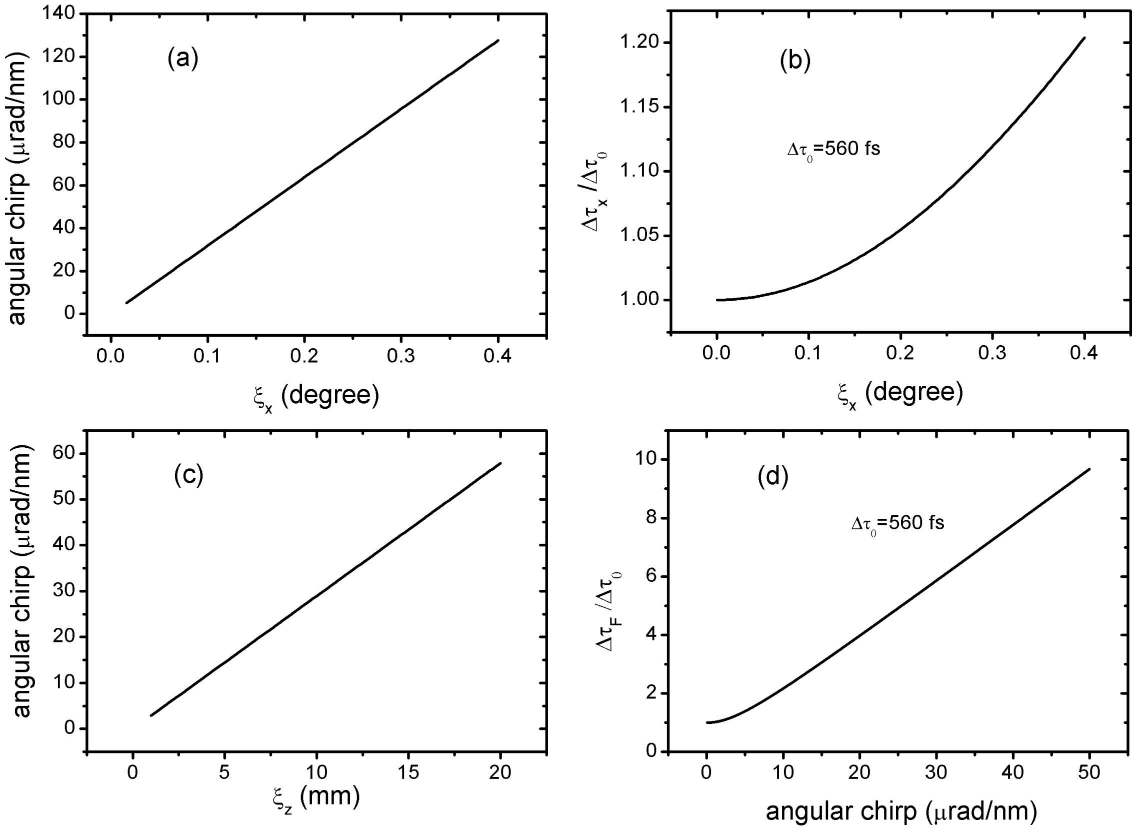

Figure 2.8: Alignment sensitivity of the grating based stretcher and compressor: a) Angular dispersion in the horizontal plane of the compressor output beam as a functions of relative angle ξ_x between the gratings within their dispersion planes (Eq. 2.12). b) Relative change of pulse duration ($\Delta\tau_x/\Delta\tau_0$), where $\Delta\tau_0 = 560$ fs denotes the TL pulse duration, across the cross-section of the compressor output beam versus ξ_x. c) Angular dispersion in the horizontal plane of the output beam of single-grating stretcher (Fig. 2.5) due to an offset ξ_z of the mirror (M_2) from the focal plane of the focusing mirror (cf. Eq. 2.14). Change of the relative pulse duration in the center of the focal spot as a function of angular chirp (Eq. 2.13).

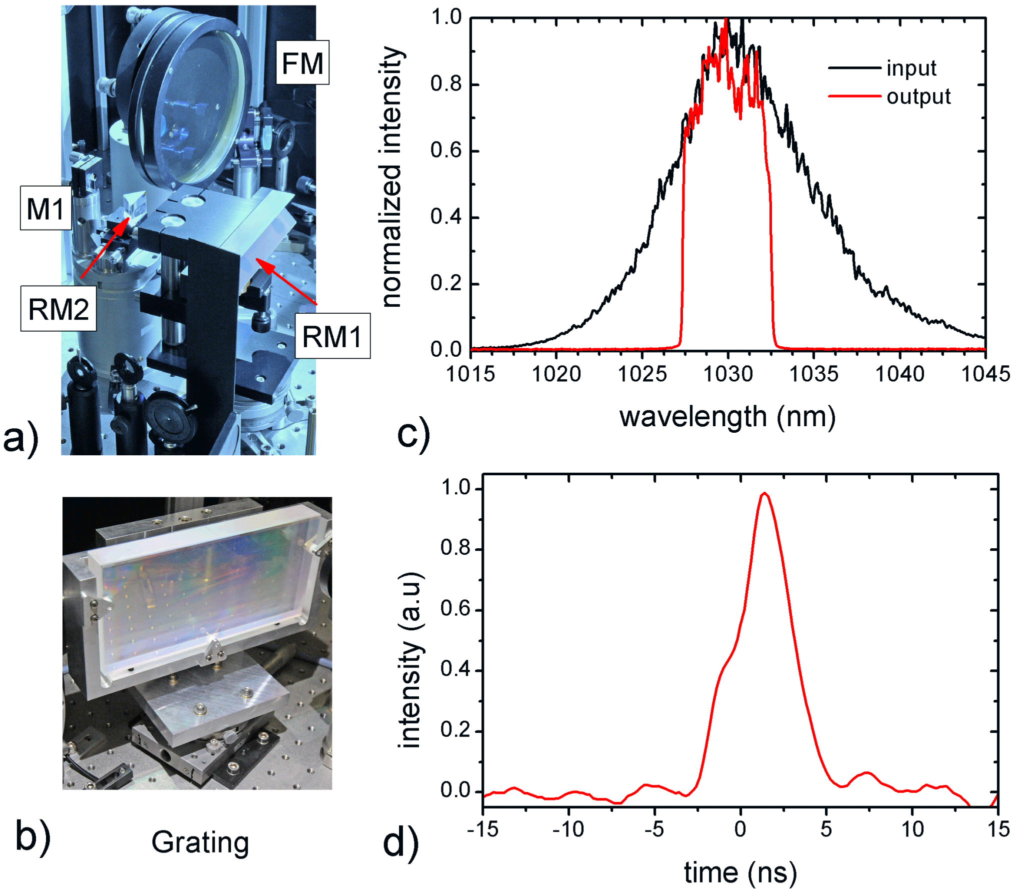

Figure 2.9: Assembly of input beam coupling mirror (M1), focusing mirror (FM), roof mirror (RM_1) and retroreflector prism (RM2) in the stretcher. b) Diffraction grating used in the setup. (c) The input and output spectra of the stretcher with a FWHM of 10 nm and 5 nm, respectively. The unnecessary part of the input spectrum is clipped off in the stretcher. (d) Output pulse with a FWHM $\sim$ 4 ns.

measured using an oscilloscope, showing a FWHM of intensity profile of $>$ 4 ns (Fig. 2.9(d)). The discrepancy between the measured and calculated widths of the stretched pulse is attributed to a rather broad and non-Gaussian output spectrum than that was assumed for the calculations.

The stretched pulses were subsequently amplified to 300 mJ at 10 Hz within a bandwidth of $\sim$3.5 nm in the first stage of the CPA pump laser consisting of an Yb:glass regenerative amplifier (RA) followed by a second Yb:YAG multipass amplifier both pumped with laser diodes, as presented in Ref. [71, 72]. After the amplifiers the pulses are recompressed in a grating compressor composed of diffraction gratings identical to that used in the stretcher. The design of this pulse compressor was discussed in section 2.2.3. Owing to the unavailability of the final amplifier stages, which were under construction during this work, we used only a single G_1 (at z=0, cf. Fig. 2.6) and G_2 for demonstration of the pulse compression. The large grating with

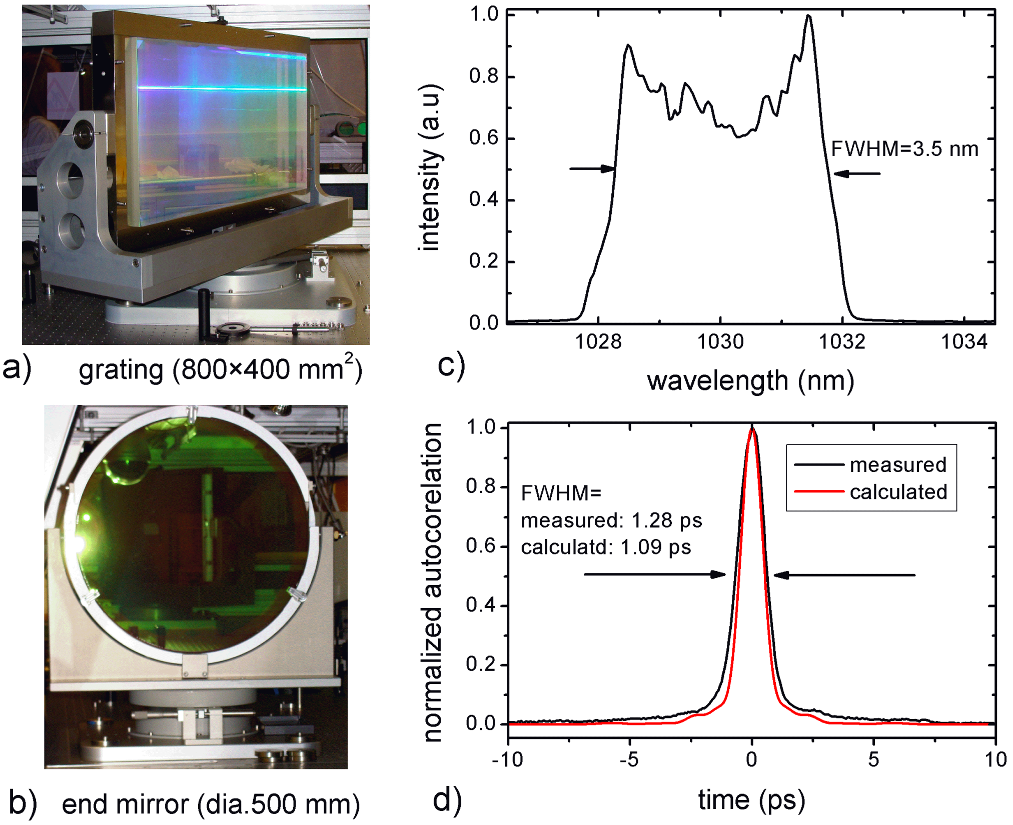

Figure 2.10: Picture of the large grating (a), and end mirror mirror (b) assembly used in the compressor. (c) Spectrum of the amplified pulse at the input of the compressor. (d) Measured and calculated autocorrelation functions of the compressor output pulse.

dimensions of 800 × 400 mm, assembled on a home-made† rotation stage (Fig. 2.10(a)) which can provide a resolution of $\sim 0.003^\circ$ for the relational motion about the vertical axis, was positioned at a distance of 6.1 m along the wavelength component $\lambda_0 = 1030$ nm. The diffracted beam after the second grating were redirected for the second pass by a 500-mm diameter end mirror (Fig. 2.10(b)) placed at a distance of ~ 3 m from the second grating. The gratings were further aligned to correct the pulse-front tilt due to the angular chirp, resulting from any relative angle between the two gratings as discussed in Sec. 2.2.4, using a home-built inverted-field autocorrelator [95]. This device can detect the pulse-front tilt in both the horizontal as well as in the vertical planes of the beam propagation axis, thereby provided a tool for the correction of the relative grating angle in these planes as discussed in Sec. 2.2.4.

The calculations of the dispersion introduced by the in-between amplifier by taking into account the physical thicknesses of all the optical materials (cf. Appendix A) revealed an additional amount of $+2.76 \times 10^5$ fs^2 of GDD and $+3.30 \times 10^5$ fs^3 of TOD for the stretched amplified pulse.

---

† at the MPQ, Hans-Kopfermann Str.1, 85748, Garching, Germany.

The extra GDD can be compensated by slightly increasing the grating separation in the compressor by ~ 3 mm. The resulting uncompensated TOD of $+2.52 \times 10^6$ fs^3 can be adjusted by fine tuning the grating separation and angle of incidence, as shown in Fig. 2.7.

The compressed pulses were characterized by a home-built single-shot second-order autocorrelator with a tuning window of 6 ps and a pixel resolution of 22 fs. This device is designed to measure 700 fs pulses with an accuracy of $\sim$6%. Under optimum conditions, we were able to get a FWHM of 1.28 ± 0.04 ps, averaged over 100 successive shots, of the autocorrelation function of the compressed pulse. In order to estimate the width of the compressed pulse, we calculated the TL pulse duration as well as the autocorrelation function from our measured spectrum. A deconvolution factor of 1.3518 was inferred from these calculations. Using this factor we can obtain a realistic estimate for our compressed pulse duration which turns out to be 947 fs, close to the calculated TL of 806 fs, with a measurement uncertainty of 40 fs. The compressor provides an overall thoughput of $\sim$66%, delivering the compressed pulses with an energy of 200 mJ. The probable reason for the difference between TL and measured pulse durations is the uncompensated higher-order dispersion of the amplified pulse, which can be improved by the installation of an acousto-optic programmable dispersive filter (AOPDF [97]). Another possibility is the spatio-temporal coupling caused by B-integral issues when the compressed pulse propagates in several meters air after the last grating.

2.3 Conclusion

We have developed a scheme for the generation of seed pulses for the CPA-chain of the PFS pump laser which is optically synchronized with the signal pulses for the OPCPA chain since both are derived from a common source. A part of the oscillator output was used for spectral shifting at 1030 nm by exploiting soliton self-frequency shift in a photonic crystal fiber. By using a rather compact and mechanically stable assembly along with an active fiber-alignment system we achieved an alignment free operation from this setup on everyday basis. We have also demonstrated the design and development of a stretcher-compressor setup for the CPA-chain of the PFS. By using a modified version of an all-reflective single grating stretcher, we have shown the stretching of sub-ps pulse to more than 3 ns for a spectral FWHM of ~ 3.5 nm centred at 1030 nm in a rather compact setup. The whole setup fits in a space of 35×300 cm^2. The implementation of the stretcher-compressor involved the designing of mechanical mounts for all the main optical components of the setups. Our grating compressor has been designed to recompress the 3-ns 50-J stretched amplified pulses, contained in four beams, to close to their original pulse duration of sub-ps. Our proposed compressor is a rather compact configuration delivering 50 J sub-ps pulses at 10 Hz rather than using four separate setups. As a proof-of-principle experiment we have demonstrated the compression of $\sim$ 300 mJ pulses in a single channel of this setup. Our single-shot autocorrelation measurements predict a 945 fs of the amplified spectrum, which is close to the TL pulse width of $\sim$800 fs. the last grating. The stretcher and compressor setups still need some fine adjustment of beam allignment to improve the spatial quality of the the output pulses. At present the spatial filtering of the output beam profiles were employed in both the stretcher and compressor setups each causing an additional loss of 5-10% of the pulse energy. Owing to high intensity of ($\sim$ 1 TW/cm^2) of the compressed pulses, B-integral of the compressed pulses exceed 1 for a propagation distance of few-meters, therefore vacuum tubing or relay imaging have to employed for preservation of spatio-temporal profile of the compressed pulses. Moreover our timing jitter calculations presented in chapter 5 suggest vacuum enclosures for the stretcher and compressor setups. In order to have a cost-effective design, particularly, for the compressor the optical distance of 6 m between the assembly of first and second grating can be folded. The work on this folded design is under way.

Chapter 3

Chirped pulse amplification of the oscillator output

The generation of a broadband spectrum appropriate for seeding the main OPCPA chain of PFS (700-1400 nm) is based on intensity dependent nonlinear effects, such as the production of a supercontinuum extending up to the near-infrared or idler generation using non-collinear optical parametric amplification. The details of these techniques will be discussed in the next chapter. Since such processes demand an intensity, and hence energy, that cannot be delivered by the few-nJ scale output of the master oscillator introduced in Chapter 2, a CPA scheme needs to be used. We amplified the part of the oscillator output which was dedicated for the OPCPA seed using a CPA-based Femtopower amplifier (Femtolasers GmbH). The commercial system comprises a double-prism pair compressor for compression of the amplified pulses.

In this chapter we discuss the drawbacks of pulse compression when only a prism compressor is used. A hybrid pulse compression (HPC) technique, i.e. a combination of high-dispersive negative mirrors (HDM's) and prism compressor, is demonstrated to cope with these challenges [49, 98]. We also present modification in the calculations of the dispersion of a double-prism compressor previously reported by Cheng et al., [50]. Here, the impact of the beam diameter of incident beam and bulk material of the prisms on the effective dispersion of the prism compressor is demonstrated. Moreover an alternative technique for the compression of TW-level pulses using a novel high-dispersive mirror compressor is presented, providing remarkable simplifications in dispersion management.

3.1 Femtopower amplifier upgrade

The schematic sketch of the experimental setup is shown in Fig. 3.1. A part of the oscillator output is injected into the Femtopower system which contains an SF57 glass-stretcher, an acousto-optical dispersive filter [97] (DAZZLER, FASTLITE) and a multi-pass Ti:sapphire amplifier [99]. The seed pulse in this setup is dominantly stretched by the material dispersion of SF57 glass and DAZZLER crystal (TeO_2), contributing positive chirp to the amplifier input pulse. Different optical media in the amplifier such as polarizers, Pockels cell, Ti:sapphire crystal etc. (cf. Table 3.1) also contribute to the dispersion of the amplified pulse. The TOD mirrors and programmable higher-order dispersion from the DAZZLER are used for fine correction of spectral phase during recompression of the amplified pulse. The amplifier is a 10-pass system operating at 1 kHz, pumped at 527 nm by the frequency-doubled output of a Nd:YLF laser (DM30, Photonics Industries). It delivers 2 mJ pulses with a FWHM spectral bandwidth of 62 nm centred at 790 nm. The output pulses are subsequently compressed in a LAK16 double-prism pair compressor. Using only the prism compressor for correcting the spectral phase of the mJ-scale femtosecond pulses results in self-phase modulation (SPM) in the prism material and consequently spectral narrowing as shown later in Fig. 3.5(b). An HPC technique, in which the amplified pulses are recompressed using HDM's in combination with the prism compressor, was developed to resolve this problem. In the scheme, the chirp of the input pulses is partially corrected by the negative group velocity dispersion of the prism compressor. The pulses pass through the prism material at reduced intensity, hence avoiding the SPM, by carrying some chirp and are finally compressed by the HDM's.

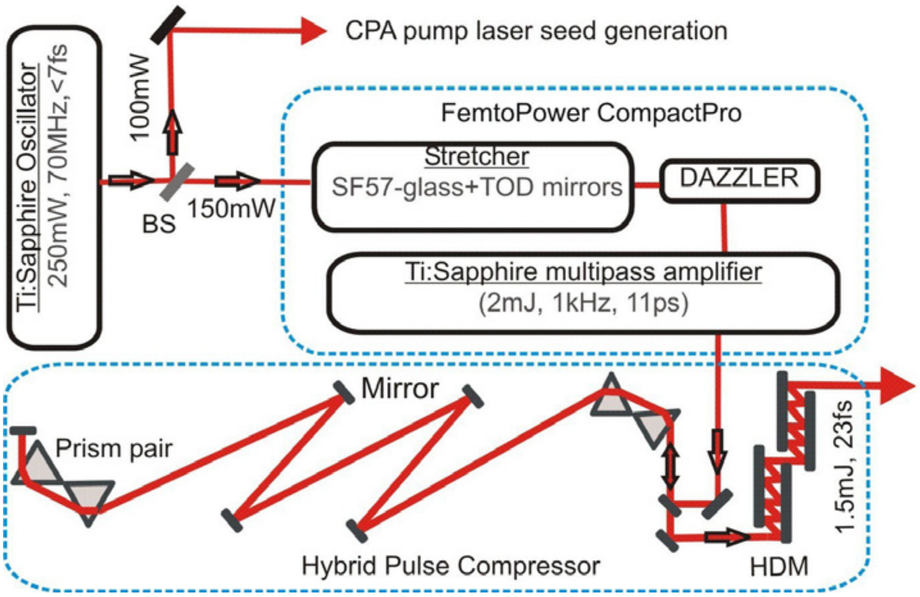
CPA pump laser seed generation
Ti:Sapphire Oscillator
250mW, 70MHz,<7fs
100mW
BS
150mW
FemtoPower CompactPro
Stretcher
SF57-glass+TOD mirrors
DAZZLER
Ti:Sapphire multipass amplifier
(2mJ, 1kHz, 11ps)
Mirror
Prism pair
1.5mJ, 23fs
Hybrid Pulse Compressor
HDM

Figure 3.1: Schematics of the Femtopower amplifier and hybrid pulse compressor. BS: beam splitter; TOD mirror: mirrors with third-order dispersion; HDM: high dispersive mirrors.

In the following, we first present the calculations of the dispersion of the amplified pulse. This is followed by the calculations of the dispersion introduced by the prism compressor to find the required separation for the pulse compression. In these calculations we evaluate the GDD as a function of angular frequency (or wavelength) which allows us to calculate the coefficients of dispersion, hence the spectral phase (cf. Eq. 2.4), of the pulse at any arbitrary angular frequency (or wavelength). Finally, the arrangement for the HPC is discussed.

3.1.1 Dispersion calculation of the amplified stretched pulse

As discussed in the previous section, the input pulses of our amplifier setup are temporally stretched by the material dispersion of different optical components. In this section we review a few formulae for calculating this dispersion, and hence the chirp of the amplified pulses in our setup.

The GDD has been defined as the coefficient of Taylor expansion of frequency-dependent spectral phase $\Phi(\omega)$ in Eq. 2.4. For an optical material with a thickness l_i and frequency-dependent refractive index $n_i(\omega)$ it can be written as [88]

$$\frac{\partial^2 \Phi_i(\omega)}{\partial \omega^2} = \frac{\partial^2}{\partial \omega^2}\left(\frac{\omega}{c} n_i(\omega) \cdot l_i\right) \tag{3.1}$$

Differentiating twice Eq. 3.1 with respect to ω we have

$$\frac{\partial^2 \Phi_i(\omega)}{\partial \omega^2} = \frac{l_i}{c}\left(2\frac{\mathrm{d}n_i(\omega)}{\mathrm{d}\omega} + \omega\frac{\mathrm{d}^2 n_i(\omega)}{\mathrm{d}\omega^2}\right). \tag{3.2}$$

Substituting $\frac{\mathrm{d}n_i(\omega)}{\mathrm{d}\omega} = \frac{-\lambda^2}{2\pi c}\frac{\mathrm{d}n_i(\lambda)}{\mathrm{d}\lambda}$ and $\frac{\mathrm{d}^2 n_i(\omega)}{\mathrm{d}\omega^2} = \frac{\lambda^3}{(2\pi c)^2}\left(2\frac{\mathrm{d}n_i(\lambda)}{\mathrm{d}\lambda} + \lambda\frac{\mathrm{d}^2 n_i(\lambda)}{\mathrm{d}\lambda^2}\right)$ in Eq. 3.2 we obtain

$$\frac{\partial^2 \Phi_i(\omega)}{\partial \omega^2} = \frac{\lambda^3}{2\pi c^2} \cdot l_i \frac{\mathrm{d}^2 n_i(\lambda)}{\mathrm{d}\lambda^2}. \tag{3.3}$$

Equation 3.3 describes the GDD introduced by an optical material as a function of wavelength. Summation over all the optical materials from our amplifier setup would yield the cumulative GDD of the amplified pulses, as follows

$$\mathrm{GDD}\,|_{amp.} = \frac{\lambda^3}{2\pi c^2}\sum_i \left(l_i \frac{\mathrm{d}^2 n_i(\lambda)}{\mathrm{d}\lambda^2}\right). \tag{3.4}$$

The calculated GDD of the amplified pulse in our setup is shown in Fig. 3.2(a). The GDD curve is obtained by taking into account the physical thicknesses of all the optical materials in our setup (cf. Table 3.1). It also includes an additional programmable dispersion of $+6800\ \mathrm{fs}^2$ (GDD) from the DAZZLER for the whole range of 735–845 nm of the amplified spectrum (see measured spectrum later in Fig. 3.8(a)). The calculated coefficients of dispersion of the amplifier output pulses at $\lambda_0 = 790$ nm are: $\mathrm{D}_2 = +41500\ \mathrm{fs}^2$, $\mathrm{D}_3 = +22000\ \mathrm{fs}^3$ and $\mathrm{D}_4 = -7000\ \mathrm{fs}^4$ (fourth-order dispersion: FOD), for definition see Eq. 2.4. The group delay (i.e. $\mathrm{GD} = \frac{\partial \Phi(\omega)}{\partial \omega}$), as derived by integrating the cumulative $\mathrm{GDD}(\omega)$ function with respect to ω, is shown in

Table 3.1: Optical thicknesses of different components of the laser amplifier in our setup

Optical component[a]	**Material**	**Thickness [mm]**
stretcher	SF57	60
DAZZLER	TeO_2 (Tellurium Dioxide)	25
Faraday rotator	$CaCO_3$ (Calcite)	2
	quartz	4
	TGG (Terbium Gallium Garnet)	21
multipass cavity	Ti:sapphire	10×4
	fused silica	20×1
Pockels cell	DKDP	20
	SK10	11×2
Bereck compensator	MgF_2	4
	fused silica	25
glass windows	fused silica	25
lenses	BK7	8
air	air	15 m

---

[a] The significance of most of these components can be found in [99].

Fig. 3.2(b). This curve provides a direct estimate of the relative time difference between different spectral components of the pulse. From this figure it can be deduced that the amplifier output pulse in our setup, with its spectrum ranging from 735–845 nm, extends up to ~15 ps.

3.1.2 Dispersion of the prism compressor

The schematic model of the double-prism pair compressor is shown in Fig. 3.3. Four prisms with an identical apex angle α_p are arranged for the angle of minimum deviation for the central wavelength λ_0. θ_i and φ_i $(i = 1 \cdots 8)$ denote the respective angles of incidence and refraction at the eight interfaces. The chirp introduced by the prism compressor is a cumulative effect of the angular dispersion and material dispersion [100]. The effective GDD of the prism compressor can be written as follows

$$\mathrm{GDD}\big|_{eff} = \left.\frac{\mathrm{d}^2\Phi(\omega)}{\mathrm{d}\omega^2}\right|_{ang} + \left.\frac{\mathrm{d}^2\Phi(\omega)}{\mathrm{d}\omega^2}\right|_{mat}. \tag{3.5}$$

Most of the optical materials exhibit positive GDD, in the spectral range of our interest (cf. Fig 3.2(a)), whereas the angular spread (refraction) after the prisms results in negative GDD.

The GDD due to the angular dispersion can be calculated using the optical construction

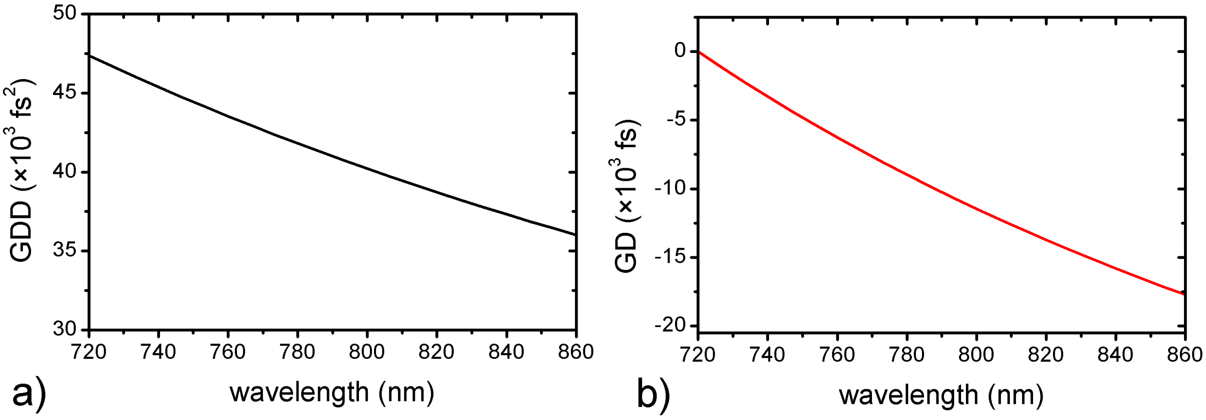

Figure 3.2: a) Calculated GDD, and b) GD of the stretched amplified pulse after the multi-pass laser amplifier

adapted by Fork et al. [47], and by Cheng et al. [50] for the so-called principle arrangement (see Appendix B). In this arrangement the spectral components at λ_0 travel through the vertices of all prisms i.e. along the curve *BCDEF* (Fig. 3.3(a)).

$$\left.\frac{\mathrm{d}^2\Phi(\omega)}{\mathrm{d}\omega^2}\right|_{ang} = 2\cdot\frac{\lambda^3}{2\pi c^2}\cdot\frac{\mathrm{d}^2P(\lambda)}{\mathrm{d}\lambda^2}, \tag{3.6}$$

where $P(\lambda)$ denotes the total optical path length (cf. Appendix B), while $\Phi(\omega)$ is the spectral phase delay introduced by the angular dispersion, and the factor 2 is for double pass configuration. For the apex-to-apex distances of ℓ_1, L, and ℓ_2 between the prisms P_1-P_2, P_2-P_3, and P_3-P_4, respectively $\frac{\mathrm{d}^2P(\lambda)}{\mathrm{d}\lambda^2}$ can be calculated as [50]

$$\begin{aligned}\frac{\mathrm{d}^2P(\lambda)}{\mathrm{d}\lambda^2} &= (\ell_1+\ell_2)\left\{\frac{\mathrm{d}^2\varphi_2(\lambda)}{\mathrm{d}\lambda^2}\sin[\theta_1-\varphi_2(\lambda)]-\left[\frac{\mathrm{d}\varphi_2(\lambda)}{\mathrm{d}\lambda}\right]^2\cos[\theta_1-\varphi_2(\lambda)]\right\}+\\ &L\left\{\frac{\mathrm{d}^2\varphi_4(\lambda)}{\mathrm{d}\lambda^2}\sin[\varphi_4(\lambda_0)-\varphi_4(\lambda)]-\left[\frac{\mathrm{d}\varphi_4(\lambda)}{\mathrm{d}\lambda}\right]^2\cos[\varphi_4(\lambda_0)-\varphi_4(\lambda)]\right\},\end{aligned} \tag{3.7}$$

where

$$\varphi_2(\lambda) = \arcsin\left[n_p(\lambda)\sin\alpha_p\cos\left[\arcsin\left(\frac{\sin\theta_1}{n_p(\lambda)}\right)\right]-\cos\alpha_p\sin\theta_1\right], \tag{3.8}$$

$$\varphi_4(\lambda) = \arcsin\left[n_p(\lambda)\sin\alpha_p\cos\left[\arcsin\left(\frac{\sin\Gamma(\lambda)}{n_p(\lambda)}\right)\right]-\cos\alpha_p\sin\Gamma(\lambda)\right], \tag{3.9}$$

and $\Gamma(\lambda)=\theta_3=2\theta_1-\varphi_2(\lambda)$.

Equation 3.7 is only valid for the principle configuration for which the spectral components at λ_0 travel through the vertices of all prisms, i.e. along the curve *BCDEF* (Fig. 3.3(a)), as discussed in Ref. [50]. In this arrangement, the wavelengths smaller than λ_0 (denoted by λ_s) are clipped off at the apex C of prism P$_2$, while the longer wavelengths (λ_ℓ) are cut at D. In order

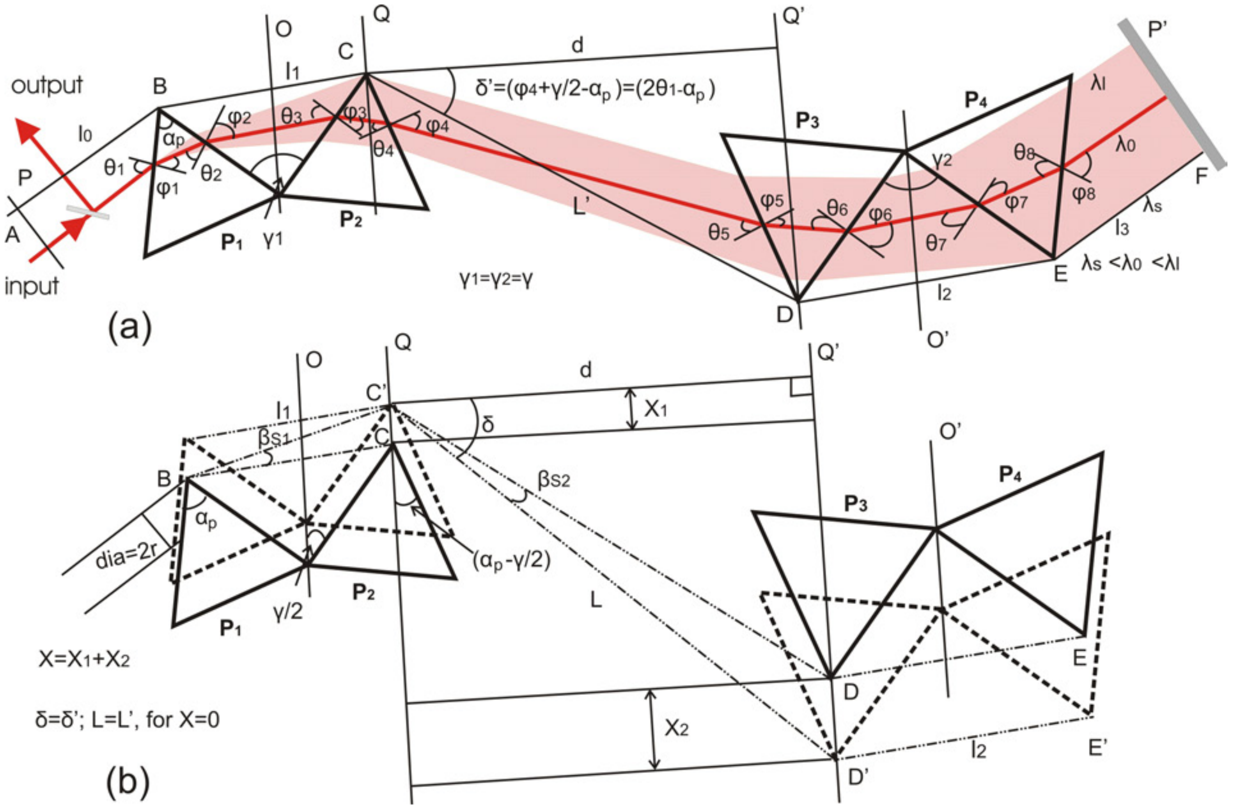
output
input
(a)
B
O
Q
C
d
Q'
P'
l1
l0
P
A
θ1
φ1
αp
φ2
θ2
θ3
φ3
θ4
φ4
P1
γ1
P2
δ'=(φ4+γ/2-αp)=(2θ1-αp)
L'
P3
P4
γ2
θ8
λl
λ0
φ5
θ5
θ6
φ6
θ7
φ7
φ8
F
λs
l3
E
λs <λ0 <λl
l2
D
O'
γ1=γ2=γ
(b)
O
Q
C'
C
d
Q'
X1
δ
l1
βS1
B
αp
dia=2r
βS2
(αp-γ/2)
P1
P2
γ/2
L
P3
P4
O'
E
D
X2
l2
E'
D'
X=X1+X2
δ=δ'; L=L', for X=0

Figure 3.3: Schematic diagram of the double-prism compressor. The optical construction is adapted from [50].

to accommodate the λ_s components, the prism P_2, hence P_1 (being paired), is translated along axis O, as shown in Fig. 3.3(b). Similarly, the prism pair P_3-P_4 is shifted parallel to the axis O' to capture the λ_ℓ wavelengths. The third such displacement of both prism pairs is caused by the spatial beam profile (beam diameter) of the incoming pulse. These effects contribute material dispersion to the input pulse which is calculated as follows.

The GDD introduced by the prism material can be written as (recalling Eq. 3.3)

$$\left.\frac{\mathrm{d}^2\Phi(\omega)}{\mathrm{d}\omega^2}\right|_{mat} = 2\cdot\frac{\lambda^3}{2\pi c^2}\cdot L_m\frac{\mathrm{d}^2 n_p(\lambda)}{\mathrm{d}\lambda^2}, \tag{3.10}$$

where L_m is the total optical material length for a single pass through all the four-prisms (P_1–P_4) corresponding to the wavelength λ_0. The factor 2 in Eq. 3.10 is for the double-pass configuration, as adapted in Eq. 3.6. L_m can be subdivided into the individual contributions from each prism pair as

$$L_m = L_{m12} + L_{m34}, \tag{3.11}$$

where $L_{m12} = 2(L_{md} + L_{m2})$ and $L_{m34} = 2(L_{md} + L_{m3} + L_{m4})$ are the material lengths through the prism pairs P_1-P_2 and P_3-P_4, respectively (see Appendix B for details). Here, L_{md} is the material length through each prism due to the input diameter ($2r$) given by

$$L_{md} = \frac{2r}{\cos\theta_1} \cdot \frac{\sin\alpha_p}{\cos\theta_2}, \tag{3.12}$$

where r is the beam radius. L_{m2} is an additional contribution to L_{m12} when P_2, hence P_1 (being paired), is translated parallel to the axis O by an amount X_1 in order to capture the λ_ℓ wavelength components of the input spectrum

$$L_{m2} = X_1 \cdot \frac{\cos(\theta_3 - \theta_1)}{\cos\theta_3} \cdot \frac{\sin\alpha_p}{\cos\theta_4}, \tag{3.13}$$

where $X_1 = \ell_1 \cdot \tan\beta_{s1}$ and $\beta_{s1} = |\varphi_2(\lambda_\ell) - \varphi_2(\lambda_0)|$. Similarly, L_{m3} is the material length when P_3, hence P_4, is translated by an amount X_2 in order to accommodate the λ_s wavelength components

$$L_{m3} = X_2 \cdot \frac{\cos\delta'}{\cos\varphi_4} \cdot \frac{\sin\alpha_p}{\cos\theta_6}, \tag{3.14}$$

where, $X_2 = d \cdot (\tan(\delta' + \beta_{s2}) - \tan\delta)$, $\delta' = (\varphi_4 + \gamma/2 - \alpha_p)$ and $\beta_{s2} = |\varphi_4(\lambda_\ell) - \varphi_4(\lambda_0)|$. The perpendicular distance d between the axes Q and Q' is related to L (Fig. 3.3(b)) for a total displacement $X = (X_1 + X_2)$ as

$$L = \sqrt{d^2 + (d\tan\delta' + X)^2}. \tag{3.15}$$

Owing to the symmetry of angular dispersion of P_1 and P_4, the second prism pair (P_3-P_4) will be translated by a distance X_1, contributing an additional material length $L_{m4} = L_{m2}$. By substituting the Eqs. 3.11–3.14 in Eq. 3.10, the contribution due to the prism material for the double-pass configuration can be calculated, which in combination with Eq. 3.6 can be used to evaluate the effective dispersion of the prism compressor in a real setup.

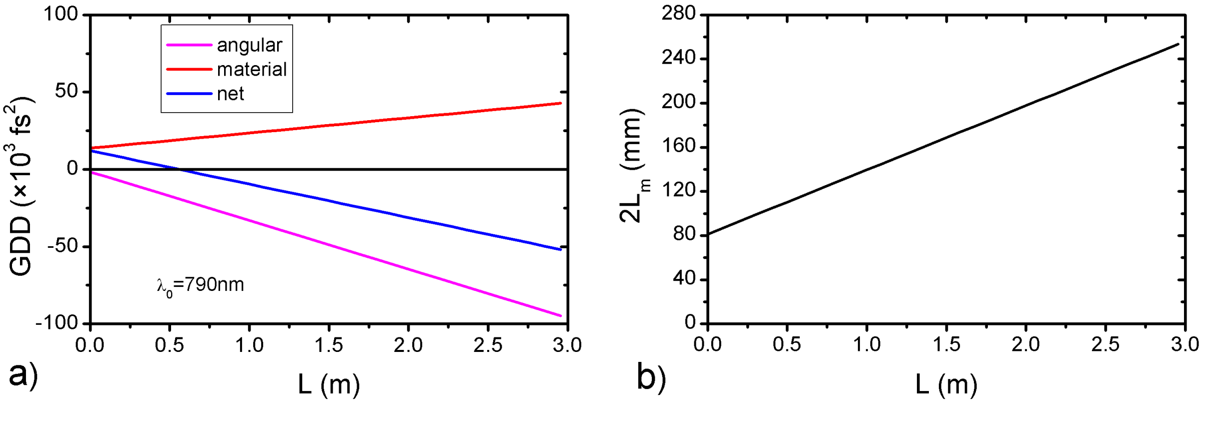

Figure 3.4: (a) Variation of the calculated GDD of the prism compressor at λ_0, and (b) the amount of total prism material (2L$_m$) with respect to the separation L (see text for more details).

We performed the calculations of the GDD for the prism compressor of our setup containing four LAK16 prisms each having an identical apex angle $\alpha_p = 60°$. The side lengths of the equilateral prisms for the pairs P_1-P_2 and P_3-P_4 were taken to be 45 mm and 90 mm, respectively. The input beam diameter was considered as 10 mm, as for our experiment setup. The results of the calculations are presented in Figs. 3.4 and 3.5. As can be seen from Fig. 3.4(a), the GDD of the prism compressor at $\lambda_0 = 790$ nm varies linearly with respect to the separation L. For the described parameters, the GDD introduced by the prism material has a slope of $+9.8$ fs^2/mm, whereas the angular dispersion contributes -31.5 fs^2/mm. Therefore the net GDD has a slope of -21.6 fs^2/mm when regarded as a function of prism separation. A prism separation of 2.45 m is required to compensate the GDD of $+41500$ fs^2 of the amplified pulse at $\lambda_0 = 790$ nm. The change of total amount of prism material ($2L_m$) as function of L can be realized from Fig. 3.4(b). It varies from 80 mm to 255 mm for a change of L from 0 to 3 m. Therefore the effect of such a large amount of material dispersion should be taken into account when dealing with femtosecond pulses.

Figure 3.5 presents the effective GDD of the prism compressor for the spectral range of the amplified pulse for L=2.45 m. The calculated GDD of the amplified pulse, previously shown in Fig. 3.2(a), is also presented for comparison. As can be seen, these curves do not match for the whole spectral range of the amplified pulse. The difference is due to a mismatch between the higher-order dispersion coefficients of the amplifier output pulse and that of the prism compressor. Therefore only the GDD could be exactly compensated with this arrangement. An additional source of dispersion, e.g. chirped TOD mirrors or DAZZLER, is required to compensate the residual dispersion of the compressor.

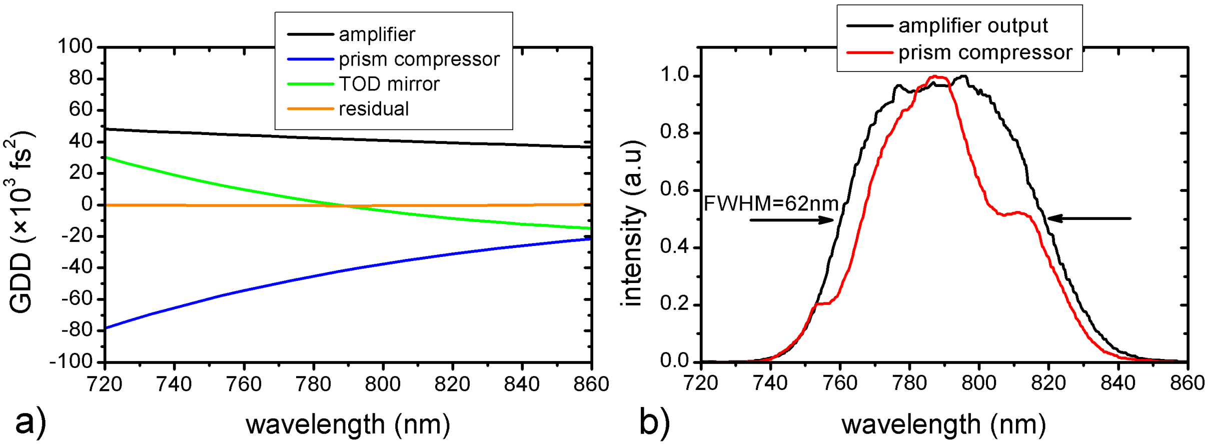

Figure 3.5: (a) Comparison of GDD of the amplifier output pulse (black) with that of the prism compressor (blue) at L=2.45 m. The rest of the dispersion (green) is compensated by the TOD mirrors and DAZZLER. The orange curve depicts the residual GDD after prism compressor. (b) The measured spectra at the output of the amplifier and prism compressor showing the effect of SPM.

Having determined the role of the prism material and angular dispersion, the methodology of pulse compression in a prism compressor can now be better understood from Fig. 3.6. Here, the GD of the amplified pulse and prism compressor are schematically shown as a function of angular frequency, assuming that the chirp is always linear. The input pulse enters the prism compressor positively chirped, i.e. the case when the GD increases with respect to the angular frequency. The prism introduces enough negative GDD to the incoming pulse so that it becomes slightly overcompressed (negatively chirped) before reaching the last prism (P_1) on the backward pass. The material of the last prism then introduces positive GDD to compensate the negative chirp and the pulses become maximally compressed. Because the final pulse-compression takes place inside the prism material, SPM can occur even at moderate pulse energies. In contrast to the well known spectral broadening effect due to the SPM, e.g. in hollow core fibers [57], the SPM in this case results in spectral narrowing owing to the negative pre-chirp of the laser pulses [98, 101].

Figure 3.5(b) shows the spectrum of the amplified pulse at the output of the laser amplifier with a FWHM of 62 nm. The pulse after the amplifier was injected into the prism compressor. A GRENOUILLE device (Swamp Optics) was used to characterized the compressed pulses. The separation L between the prisms was adjusted to get maximum compensation of the GDD of the input pulse. The uncompensated higher-order dispersion was measured by the GRENOUILLE and precompensated by the TOD mirrors and DAZZLER (Fig. 3.1). At a prism separation L of 2.25 m, a compressed pulse duration of $\sim$30 fs was achieved. This distance is 8% higher than our calculation. The discrepancy can be attributed to some additional GDD introduced by the TOD mirrors, not considered in our calculation owing to the unavailability of its exact data, or to a slightly different beam diameter of the input pulse of the compressor. The spectrum of the compressed pulses is depicted in Fig. 3.5(b), showing a significant spectral narrowing caused by the SPM. This SPM can deteriorate the spatio-temporal profile of the compressed pulses hence reducing the intensity at targets. In the following section a technique is presented to overcome this problem.

3.1.3 Hybrid pulse compression (HPC)

An HPC technique to overcome the problem of the SPM in prism compressors was proposed by Cavalieri et al. [98] by using positive-dispersive mirrors (PDM) after prism compressor. Here, the pulses after the amplifier are overcompressed by increasing the prism separation. They still maintain a negative chirp after the last prism, thereby reducing the peak intensity inside the prism material to avoid SPM, and are finally compressed by the PDM. However, the use of PDM's in this HPC scheme has the drawback that the pulses pass through the last prism with negative chirp. For high energy (and hence intensity) pulses, ever more negative chirp is required to avoid SPM.

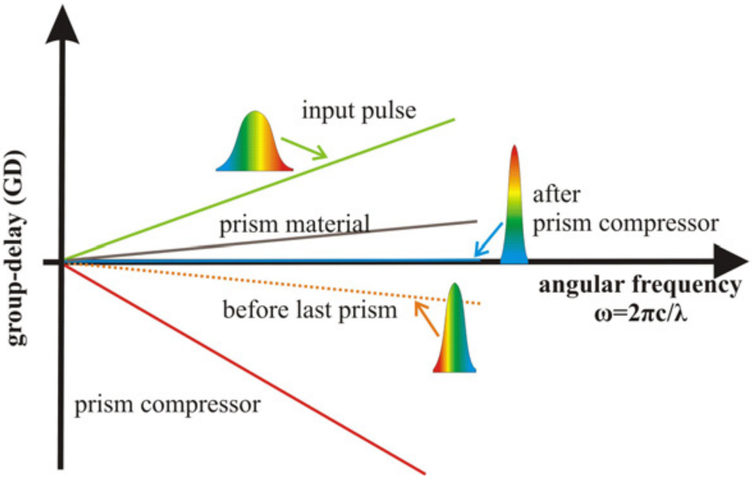

Figure 3.6: Schematic compression of a positively chirped input pulse using a prism compressor in terms of the group delay (GD): For illustration the GD introduced by each components is assumed to be a linear function of angular frequency (ω). The GD of the positively chirped input pulse is shown in green. The negative dispersion introduced by the prism compressor (red) is more than that required for the compression of input pulse. The pulse therefore becomes slightly negatively chirped before reaching the last prism of the compressor (GD shown in yellow). This chirp is finally corrected by the material dispersion (grey) of the last prism.

Therefore the required prism separation quickly becomes inconveniently large and may even lead to spectral clipping in the second pair of prisms. Moreover, changing the prism separation also results in changing the higher-order dispersion components, which in turn requires additional dispersion management. Negatively chirped mirrors, on the other hand, may be exploited to compress high-energy pulses in a straightforward way without inverting the sign of their GDD in the prism compressor, i.e. maintaining their positive chirp after the prism compressor and finally compressing them with negatively chirped mirrors. However, the implementation of these mirrors, with a reasonable number of reflections and acceptable throughput, requires high dispersion and low loss per bounce since they have to overcompensate the positive dispersion of the last prism. In order to realize this scheme we employed negatively chirped high-dispersive mirrors (HDM's), developed by Pervak et. al [49, 102], providing a nearly flat GDD of $-500\ \mathrm{fs}^2$ per reflection for a wavelength range of 735–845 nm ($\Delta\lambda = 110$ nm) as shown in Fig. 3.7(a). A GD of 160 fs per bounce in the described spectral range can be inferred for these HDM's, using the relation

$$\Delta GD = -\frac{2\pi c}{\lambda_0^2}\Delta\lambda \cdot GDD. \tag{3.16}$$

An HDM utilizes a combined effect of two most commonly used technologies in multilayer mirror technology to provide high dispersion [49]; i) penetration effect (conventional chirped mirror CM) [103], and ii) optical standing-wave resonance effect (Gires-Tournois interferometer dispersion mirrors (GTIDMs) [104]. In a conventional CM, the optical thickness between different coating layers in the dielectric mirror structure changes in a specified order. This causes the light at different wavelengths to penetrate to different extent, as governed by the Bragg's law, hence experiencing a different group delay, see Fig. 3.7(b). On the other hand, in GTIDM, the dispersion is obtained by resonant trapping of selected wavelengths in a spacer layer between the upper surface reflection and the underlying high reflector (HR), as schematically depicted in Fig. 3.7(c). Two interfaces separated by an optical distance corresponding to the half wavelength of the incident radiation resonantly enclose the impinging wave. Such nanoscale Fabry-Perot-interferometers embedded in the multilayer structure can introduce large group delays at selected wavelengths. Combining both effects has allowed for achieving unprecedently high dispersion while keeping the losses at a minimum. The detailed design and structuring of the HDM are discussed in [49].

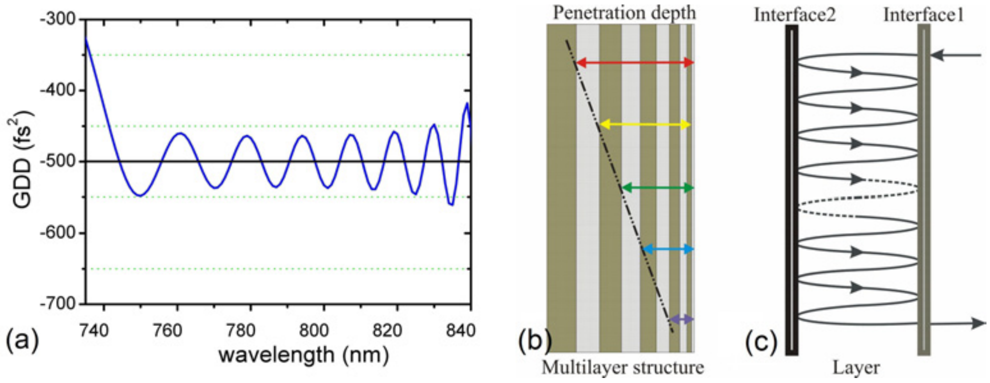

Figure 3.7: (a) Design GDD per reflection of HDM for an angle of incidence of 10° as a function of wavelength. GDD via wavelength-dependent penetration (b) and resonant storage (c) See text for explanation.

The schematic arrangement of our hybrid compressor is shown in Fig. 3.1. An additional amount of 35 mm of SF57 glass, exhibiting a GDD of $+227$ fs^2/mm at 790 nm, was inserted into the stretcher while keeping the prism separation unchanged. This method is more convenient in terms of higher-order dispersion management than reducing the prism separation prism. The pulses after the prism compressor carry a positive GDD of $\sim$8000 fs^2 which is equivalent to a GD of $>$2.66 ps for 735–845 nm or a FWHM pulse width of $>$1 ps. The peak intensity of the input pulses inside the last prism is therefore reduced by a factor of 40 compared to the case when only the prism compressor was used for compression. At this intensity level no effects of SPM were observed in the output spectrum as shown in Fig. 3.8(a). A total of sixteen 1-inch-diameter HDM's were used after the prism compressor at an angle of incidence of $10 \pm 1^\circ$ in a single-pass configuration for final compression. The higher-order dispersion coefficients of 35 mm of SF57 glass, i.e. TOD of +5000 fs^3 and FOD of +1850 fs^4, are compensated by the DAZZLER. Unlike the traditional broadband chirped mirrors, the HDM's are

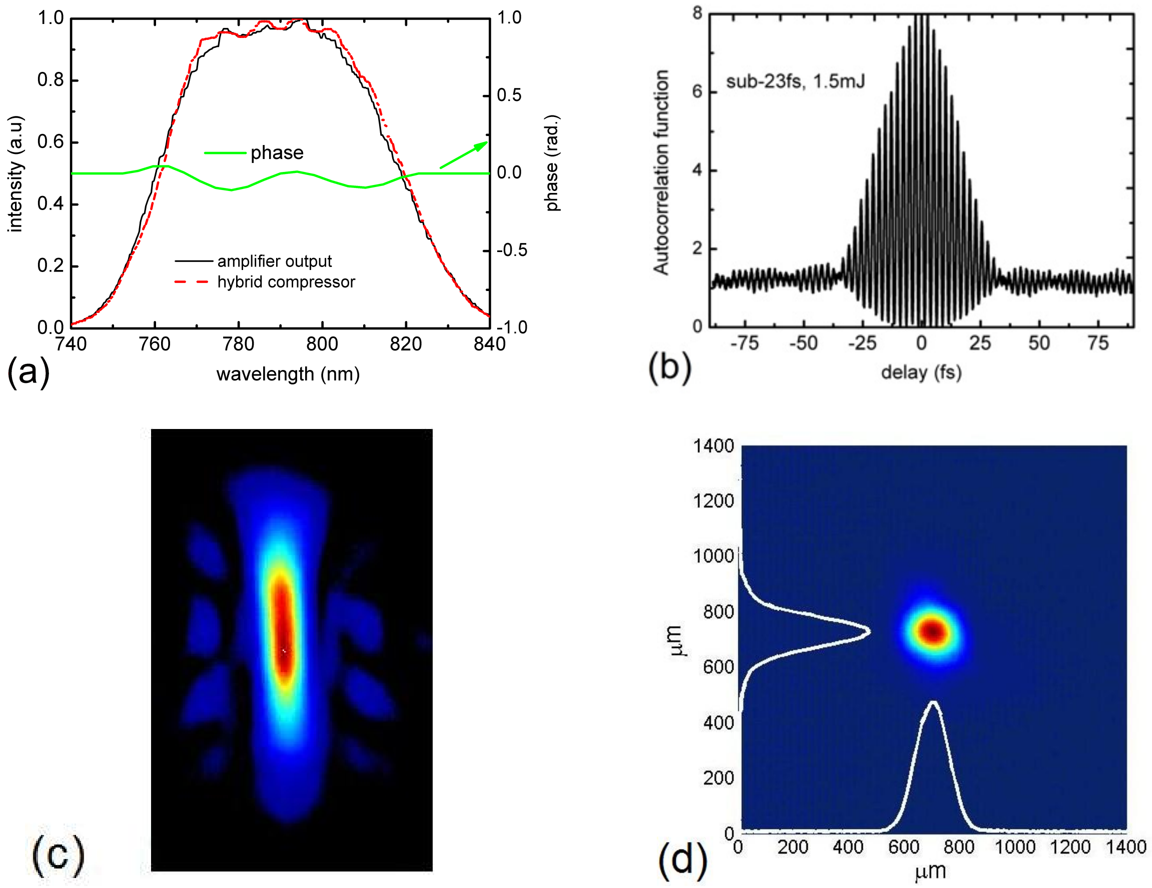

Figure 3.8: (a) Spectrum after the amplifier (black) and HPC (red). The retrieved phase of the compressed pulse (< 23 fs, FWHM, sech) by the GRENOUILLE after the HPC is shown in green. (b) The measured second-order interferometric autocorrelation (FWHM 15 fringes) of the compressed pulse after the HPC. (c) Retrieved frequency-resolved optical-gating (FROG) trace of the compressed pulse after the HPC, (d) beam profile in the far field of an f=2m lens with a $1/e^2$ diameter of 230 μm.

not designed in complementary pairs [105] to cancel out each other's inherent phase oscillations. This results in accumulation of ~1 rad of phase oscillations in the pulses after the compressor, as measured by the GRENOUILLE device. A phase file derived from this measurement was loaded into the DAZZLER to pre-compensated these phase oscillations, resulting in a nearly flat GRENOUILLE-retrieved spectral phase of the compressed pulse (Fig. 3.8(a)). The measured second-order interferometric autocorrelation function of the compressed pulse after the hybrid compressor is shown in Fig. 3.8(b). It yields sub-23 fs FWHM, for sech pulse profile, which is ~ 20% higher than the calculated TL duration of ~ 19 fs from the measured spectrum. This discrepancy can be attributed to some residual higher-order spectral phase traces as depicted in the retrieved frequency-resolved optical-gating (FROG) trace (Figs. 3.8(c)) of the GRENOUILLE.

Starting from the amplifier with 2 mJ pulse energy, we measured 1.5 mJ at the output of the hybrid compressor with an overall throughput of 75%. The HDM provided a high reflectivity of $> 99.8\%$ per bounce. The measured beam profile of the hybrid compressor output in the far-filed of a 2-m focal length lens (Fig. 3.8(d)) shows a nearly Gaussian spatial beam profile. It indicates the capability of the hybrid compressor to transmit the compressed pulse without spatial distortions.

In the following section we discuss an alternative compression based purely on the HDM's used in the hybrid scheme.

3.2 All-dispersive mirror compressor

3.2.1 Stretcher-compressor setups of conventional CPA systems

As discussed briefly in Chapter 1, conventional CPA systems use diffraction gratings [45] or prism pairs [47, 50] as the stretcher and/or compressor setups. In these setups the wavelength dependent delays are dominantly achieved by the angular dispersion. The alignment sensitivity of these components poses a serious challenge in the day-to-day operation of CPA systems. As discussed in Sec. 2.2.4, minute deviations of such dispersive elements from optimum orientations lead to angular chirp and pulse front tilt (PFT), due to the uncorrected angular chirp which results deterioration of the pulse profile in focus, both spatially and temporally, and hence reducing the intensity at the targets [95]. Moreover, dispersion management in these systems has always been a challenge to get compressed pulses close to the Fourier limited duration after amplification due to a mismatch between the higher-order coefficients of the dispersion of the optical material of the system and that of the compressor. Some specially designed third and fourth order dispersion chirped mirrors are needed in addition to the prisms or gratings [50, 51] in order to compensate the residual dispersion, which increases the complexity of these systems. The bulky prism compressors though provide a throughput higher than the grating compressors, but they suffer from the problem of the SPM, as discussed in the previous section. Dispersive mirrors offer the potential for eliminating these drawbacks owing to their capability of providing tailored dispersion over unprecedented bandwidths without spatial separation of spectral components. The wavelength-dependent delay originates from short propagation through virtually lossless, highly dispersive multilayered media. CPA implemented with dispersive mirrors is therefore intrinsically free from the angular chirp, PFT and nonlinear effects with the added benefit of higher-order dispersion control. The HDM's can be designed to provide GDD of either sign and hence compensate material dispersion both in the visible/NIR and the mid-infrared spectral range, where the GDD of most materials changes its sign.

We have employed our HDM's, also used for the HPC discussed in Sec. 3.1.3, to demonstrate the implementation of sub-20 fs, mJ-scale CPA using a rather simple and efficient all-dispersive mirror compressor (ADMC). This experiment was performed on the same setup which was already demonstrated in Fig. 3.1. However some necessary changes in the overall dispersion management were performed for this work. The Femtopower system was operated at relatively low power compared to its nominal output of 2 mJ at 1 kHz due to the available number of HDM's available during this experiment. The details of the experiment are described as follows.

3.2.2 Implementation of the ADMC

Figure 3.9(a) depicts the experimental setup. The seed pulses from the oscillator were stretched by 30 mm of SF57 glass and by the DAZZLER. Here, the TOD mirrors, which were previously used for the precompensation of higher-order dispersion of the prism compressor, are removed. The Femtopower amplifier was operated to deliver 1.4 mJ pulses at its nominal repetition rate of 1 kHz. The output pulses were recompressed using purely the HDM's (i.e. ADMC).

The dispersion of the amplified pulses was calculated by taking into account the physical thicknesses of all the optical components in the stretcher as well as in the amplifier in a similar way to that discussed in Sec. 3.1.1. The coefficients of dispersion of the amplified pulses at $\lambda_0 =$ 790 nm, in this modified setup, without any programmed-dispersion from the DAZZLER are $\mathrm{D}_2 = +34700\ \mathrm{fs}^2$ (GDD), $\mathrm{D}_3 = +22000\ \mathrm{fs}^3$ (TOD) and $\mathrm{D}_4 = -7000\ \mathrm{fs}^4$ (FOD). The DAZZLER is programmed to provide a GDD of $-8700\ \mathrm{fs}^2$ and to compensate the higher-order dispersion (D_3 and D_4) of the amplified pulses. Therefore the pulses exit the amplifier with a dispersion of $+26000\ \mathrm{fs}^2$ for the whole spectral range of the amplified pulse. This dispersion is equivalent to a GD of $\sim$8.6 ps between 735-nm and 845-nm spectral components. Our Fourier transform calculations, by assigning this dispersion to the bandwidth-limited pulse of the amplifier output spectrum, predict the FWHM duration (τ_p) of 4.8 ps of the stretched pulse. These conditions correspond to a peak fluence $F_0 = \frac{2E_p}{\pi w_e^2}$ [106, 107] of $\sim$0.6 J/cm^2, for a Gaussian beam with 1/e^2 radius (w_e) of 400 μm and pulse energy (E_p) of 1.4 mJ, inside the amplifier crystal. This is close to the required saturation fluence (F_{sat}) of 0.9 J/cm^2 for efficient extraction from the Ti:sapphire crystal [44, 108], and is well below the surface damage threshold of 5-10 J/cm^2 for Ti:sapphire for $\tau_p \sim 4.8$ ps [107]. Under these conditions the pump-to-signal extraction efficiency is 9.1%. Although it is lower by a factor of 2 than the existing systems of such characteristics [99], it can be improved with better spatial mode matching of the pump and seed beams in the crystal which was not carefully controlled during this experiment.

The described fluence of 0.6 J/cm^2 corresponds to a peak intensity (I_0) of $\sim$ 117 GW/cm^2

for the last pass in our multipass amplifier, as calculated by the following relation assuming Gaussian profile of the seed pulses

$$I_0 \approx 0.939 \frac{F_0}{\tau_p} \tag{3.17}$$

where τ_p is the FWHM pulse duration (cf. Appendix C). At such a high intensity the refractive index (n) of an optical material may become intensity dependent as

$$n = n_0 + n_2 I(r,t) = n_0 + \Delta n(I), \tag{3.18}$$

where n_0, n_2, and $I(r,t)$ denote the linear refractive index at λ_0, nonlinear refractive index, and radial- and time-dependent intensity of the pulse, respectively ($n_0 = 1.76$ [88] and $n_2 = 3.2 \times 10^{-16}$ cm^2/W [107] for Ti:sapphire at $\lambda_0 = 790$ nm). Due to the spatial variation of the laser beam intensity, this effect modifies the beam wave front generally described as B-integral [88],

$$B = \frac{2\pi}{\lambda_0 n_0} \int_0^Z n_2 I(z) dz \tag{3.19}$$

where B represents the amount of wavefront distortion due to the intensity-dependent index of refraction, accumulated by the beam over the length Z of the optical medium. For a perfectly Gaussian beam, B can cause the whole beam to self-focus, during its further propagation through the optical medium, above a critical power [58, 109] given by

$$P_{cr} = \frac{3.77 \lambda_0^2}{8\pi n_0 n_2}. \tag{3.20}$$

B less than 1 is generally considered safe to avoid bulk damage of the amplifiers [88]. However the accumulation of spatio-temporal phase distortions can happen well below the damage threshold. A tolerable value of B therefore depends on the focusability of the amplified beam, distortions in the output spectrum caused by the SPM, and its compressibility etc. Our calculated B-integral for the last amplifier pass, corresponding to the peak intensity $I_0 = 117$ GW/cm^2 and Ti:sapphire crystal length $Z = 4$ mm, is $\sim$0.6. This allows us to operate the amplifier safely at 1.4 mJ without any prominent distortion in the spatial and spectral phase of the amplified pulse.

Pulse compression and characterization

The schematic sketch of the ADMC for compression of the amplified pulses is shown in Fig. 3.9(a). The beam diameter of the amplifier output is magnified to $\sim$7 mm by using a 1:1.5-telescope. This beam size corresponds to the peak fluence of < 8 mJ/cm^2 which is well below the measured damage threshold of > 80 mJ/cm^2 for the HDM [110]. A D-cut mirror (D-mirror) is used to couple the beam into the compressor. Since the HDM's are designed to provide -500 fs^2 per reflection (see Fig. 3.7(a)), therefore a total of 52 reflections are needed for compression. We used twenty-six 1-inch-diameter HDM's separated by 96 mm for an angle of incidence of $10 \pm 1^\circ$ in a

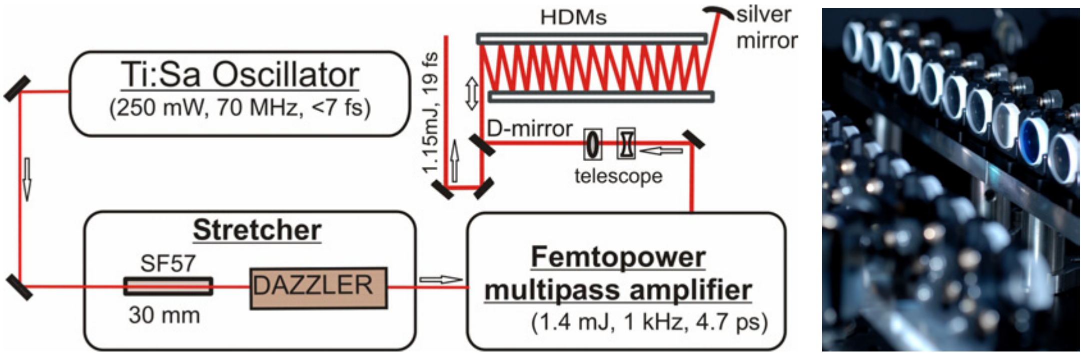

(a) (b)

Figure 3.9: (a) Schematic layout of the experimental setup. (b) Picture of the all-dispersive mirror compressor.

2-pass configuration. After the first pass, an f = 3.5 m silver mirror is used to fold the beam path for the second pass and to collimate the beam. It is coupled out by changing the height on the D-mirror in order to keep the angle of incidence identical for both passes. In this configuration, we achieve an overall ADMC throughput of 90%.

Figure 3.10 shows the results of the pulse characterization, as performed using a second order interferometric autocorrelator and the GRENOUILLE device. Residual GDD oscillations in our ADMC imprint a (maximum-to-minimum) spectral phase oscillation of ∼1.4 rad on the compressed pulses, as shown by the red curve in Fig. 3.10(c), which has been retrieved from the FROG trace in Fig. 3.10(a). These oscillations were largely removed by the DAZZLER by introducing a phase file. Since the introduced corrections are small, this did not compromise its throughput. The result is a nearly flat spectral phase (blue curve in Fig. 3.10.(c), retrieved from Fig. 3.10(b)) and a near Fourier-limited compressed pulse with a duration of 19.1 fs (FWHM), see Fig. 3.10(d). This value only differs by 0.5% from the calculated transform limited pulse duration of 19 fs for the experimentally determined spectrum. The spatial characterization of the amplified and compressed pulses yield nearly ideal Gaussian beam profiles both in the near and the far fields (see Fig. 3.11) demonstrating the capability of the ADMC to transmit the compressed femtosecond beam without a distortion of its spatial properties.

3.2.3 Outlook

An all-dispersive mirror compressor, being intrinsically free from the nonlinear effects, spatial and angular chirps, eradicates all main hurdles of CPA-systems in reaching near bandwidth-limited compressed pulses with excellent spatial quality. It provides remarkable simplifications in dispersion management. This development opens the way towards simple, alignment insensitive, compact and user-friendly TW-scale prism/grating-free femtosecond laser systems. The

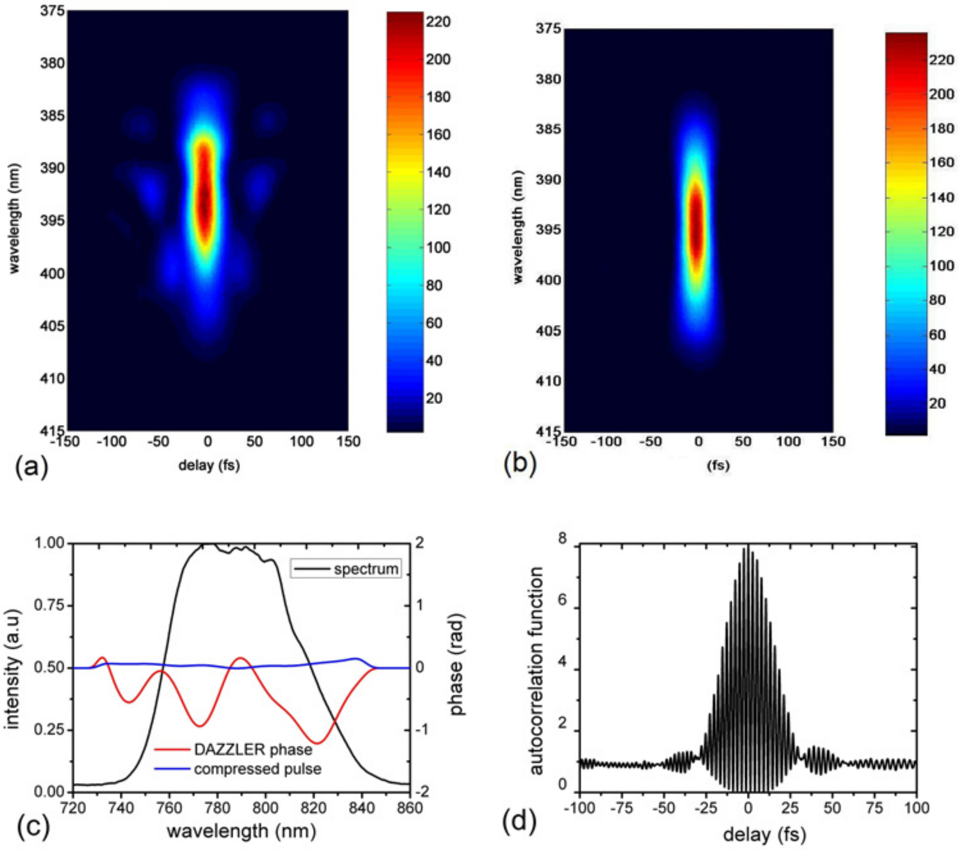

Figure 3.10: Temporal characterization of the compressed pulses: (a) The frequency-resolved optical-gating (FROG) trace without phase file in the DAZZLER, showing satellite pulses due to uncompensated phase oscillations. (b) The FROG trace of the compressed pulses after DAZZLER compensation. (c) The spectrum (black) and the phase of the compressed pulse (blue). The residual phase oscillations after 52 reflections on HDM's (red) before compensation by the DAZZLER (see text). This fine correction reduces the pulse duration by approximately 3 fs. (d) The measured 2nd order interferometric autocorrelation trace of the compressed pulse with a FWHM duration of 19.1 fs.

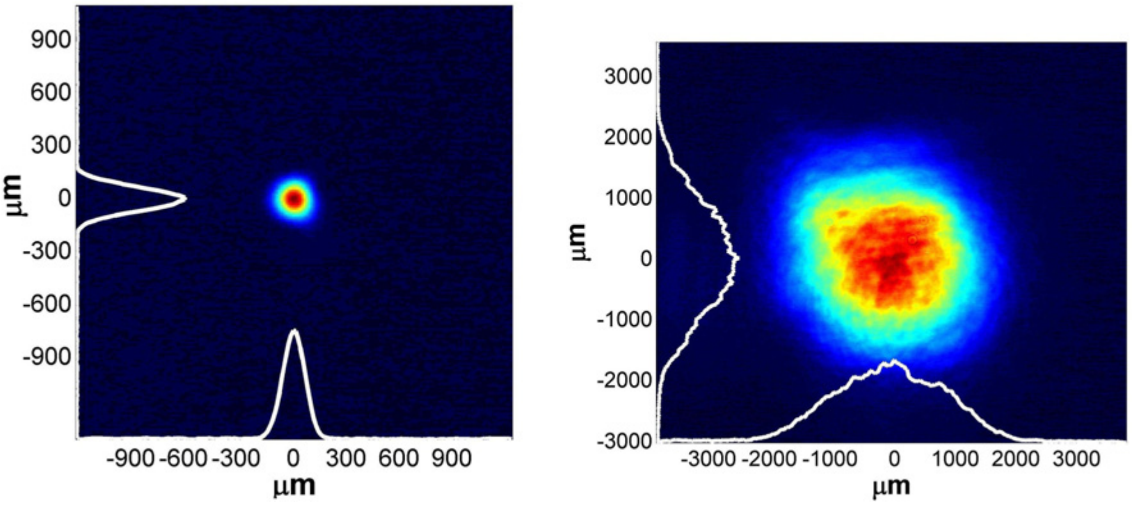

(a) (b)

Figure 3.11: Beam profile of pulses compressed after the all-dispersive mirror compressor. (a) The beam profile in the far-field of a 1.5 m focal length lens showing an excellent beam quality for a 1/e^2 spot size of 250 μm. (b) The near-field beam profile with a 1/e^2 spot size of 3.5 mm.

state-of-art ADMC based CPA calls for multilayer dispersive structures with high GDD and low loss (denoted by $\mathfrak{L}$) over a spectral range of several tens of THz. The figure of merit, FOM $= \frac{|\mathrm{GDD}|}{\mathfrak{L}}$, determines the loss at the expense of which a certain amount of dispersion for a certain stretching factor can be realized. The scalability of the ADMC-based CPA can be presumably determined by considering an overall loss of $\approx$30% as the upper limit for possible number of reflections for compression, comparable to that of a conventional grating compressor or HPC [111]. By taking into account the characteristics of the HDM's presented in this work, a total GDD of $\pm$75000 fs^2 in 150 bounces can be achieved. This is equivalent to a GD of $\pm$24000 fs for the spectral range of 735-845 nm. Such dispersion is, in principle, enough for damage-free amplification up to TW-level power using a Ti:sapphire crystal. By selecting a 1/e^2 diameter of $\sim$2.6 mm inside the crystal for $\sim$26 mJ seed pulses, we can achieve an energy fluence of the order of F_{sat} for efficient extraction of deposited pump energy. This fluence can be maintained up to a crystal length of $\sim$10 mm while keeping B$<$1. For compression of these pulses a beam diameter of $\sim$11 mm can be safely adapted for the ADMC while keeping the peak energy fluence less than 70% of the measured threshold for damage of the HDM. The present coating technology, available in house, can handle round mirror substrates of 4 inch diameter and rectangular ones with dimension of 80×60 mm^2 [112]. Therefore only three pairs of such rectangular HDM can easily provide the required 150 reflections in a 4-times folded geometry to deliver TW-level compressed pulses. One of the main limitations of the present design of an HDM is its GDD oscillations (cf. 3.7(a)) which significantly influence the contrast of the compressed pulses. The present ADMC approach inevitably requires the DAZZLER for compensating this unwanted effect. Therefore the design of the HDM should be improved in a way to have more fine control on these GDD oscillations or the complementary mirror approach should be adapted as discussed in [113, 114].

3.3 Conclusion

In conclusion, the oscillator output which was dedicated for the OPCPA seed generation is amplified to 2 mJ using a commercial Ti:sapphire chirped pulse amplifier. A hybrid pulse compression scheme, consisting of double-prism pair and high-dispersive negatively chirped mirrors, is demonstrated to overcome the problem of self-phase modulation in the prism compressors when used alone in this application. By using 16 high-dispersive negatively chirped mirrors in combination with a pair of double prisms we have demonstrated compression of 1.5 mJ pulses down to sub-25 fs pulse duration. Moreover we have demonstrated a novel implementation of chirped-pulse amplification by using high-dispersive multilayer mirrors for chirp control. Our prototypical dispersive-mirror compressor designed for a kHz Ti:sapphire amplifier, yielded — in a proof-of-concept study— millijoule-energy, sub-20-fs, 790-nm laser pulses with an overall throughput of $\sim$90% and unprecedented spatio-temporal quality. This scheme permits a dramatic simplification of dispersion management in high-power lasers and affords promise for their advancement to shorter pulse durations, higher peak powers, and higher average powers with user-friendly systems.

Chapter 4

Broadband seed generation for OPCPA chain

As discussed in Chapter 1, the design of the PFS system requires 700–1400-nm broadband seed pulses for the OPCPA chain which are optically synchronized with the pump laser. For optical synchronization we derive both of theses from the master oscillator. Using a fraction of this oscillator output power, a scheme for pump laser seed generation was discussed in Chapter 2. In Chapter 3, we have discussed the CPA-based amplification of the oscillator output in Ti:sapphire delivering 1.5 mJ, 25 fs pulses for the OPCPA seed generation. In the following we will present different schemes for shifting and broadening these pulses to the desired wavelength range of the OPCPA seed.

First, we will discuss a scheme for idler generation using non-collinear OPA (NOPA) in a BBO crystal, which is pumped by the second harmonic of the Ti:sapphire output pulse and seeded by a spectrally broadened version of its fundamental. Second, we will detail a cascaded spectral broadening scheme for generating an ultrabroadband supercontinuum using again the Ti:sapphire output. Finally, the feasibility of this supercontinuum for seeding the OPCPA chain of the PFS will be discussed. We will present two types of setups for supercontinuum generation: i) a hollow core fiber (HCF) followed by filamentation in gas cell (HCF-filament), and ii) a two-stage HCF (cascaded-HCF). Thirdly, a comparison of these three methods will be presented to select the most suitable scheme for our conditions. Lastly, the design of the OPCPA seed stretcher and compressor will be discussed.

Before discussing the details of the idler generation scheme, we review a brief introduction of the OPA process from the literature [60, 100, 115].

4.1 Optical parametric amplification

In optical parametric amplification a high frequency, high intensity beam, the pump, amplifies a low frequency, lower intensity beam, the signal. This interaction leads to the spontaneous generation of a third beam, the idler. This process is governed by the laws of conservation of energy

$$\hbar\omega_p = \hbar\omega_s + \hbar\omega_i \tag{4.1}$$

and momentum

$$\hbar\vec{k_p} = \hbar\vec{k_s} + \hbar\vec{k_i}. \tag{4.2}$$

Here $\omega_{p,s,i}$ and $\vec{k}_{p,s,i}$ are the frequencies and wave vectors of the pump, seed and signal, respectively. k is related to the ω- and frequency-dependent refractive index $n(\omega)$ as

$$|\vec{k}| = k = n(\omega)\frac{\omega}{c} = n(\lambda)\frac{2\pi}{\lambda}. \tag{4.3}$$

Eq. 4.2 is also known as the phase matching condition and is the key requirement that needs to be satisfied to allow for efficient energy transfer between pump and signal/idler waves. The phase matching is generally characterized by the wave vector mismatch Δk. For a collinear geometry, i.e. the case when the signal, pump, and idler beams are parallel inside the nonlinear medium, Δk can be written as

$$\Delta k = k_p - k_s - k_i \neq 0. \tag{4.4}$$

In practice, the phase matching condition can only be satisfied for a finite crystal length and limited spectral bandwidth. The spectral phase difference (Δkz) between the three waves increases with increasing interaction length (z). A change of phase of π among the parametric waves causes the energy flow to reverse back to the pump wave. The corresponding interaction length for which Δkz equals to π is termed as coherence length [115]. $\Delta k = 0$, on the other hand, refers to an ideal case when the pump energy is completely depleted.

In the case of NOPA, the pump and signal beams cross at an angle (α_{int}) inside the nonlinear crystal. The phase matching bandwidth of the signal wave in this case, for a given pump wavelength and nonlinear crystal, can be higher than that of the collinear OPA if α_{int} is selected appropriately [60]. Moreover, at an optimum α_{int}, the largest phase matching bandwidth in NOPA is possible with the type-I phase matching scheme [60]. In this scheme the polarization for the pump wave is orthogonal to that of the signal and idler. In the case of a uniaxial negative crystal it can follow the $o_s + o_i \rightarrow e_p$ scheme, where the signal and idler have ordinary (o_s, o_i) polarizations, i.e. in the principle plane (which contains the optical axis and the wave vectors), and the pump has extraordinary (e_p) polarization, which is perpendicular to the principle plane.

Figure 4.1 shows the wave vectors of the pump, signal and idler in a non-collinear geometry. In this arrangement the pump and signal wave vectors form an angle α_{int} and the idler is emitted at an angle $\Omega = (\alpha_{int} + \Theta_{int})$ with respect to the signal inside the crystal, where Θ_{int} is the internal angle between the pump and idler. θ_c represents the angle between the pump wavevector and the

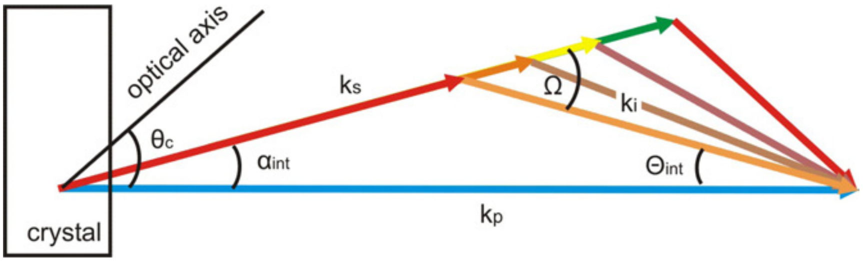

Figure 4.1: Scheme of an OPA in non-collinear geometry (NOPA): pump, signal and idler fulfill energy and momentum conservation inside a nonlinear crystal resulting in an angular chirp of the emerging idler beam. Here α_{int}, θ_c and Ω $(= \alpha_{int} + \Theta_{int})$ represent the pump-signal internal non-collinear angle, internal phase matching angle, and internal signal-idler angle, respectively.

optical axis, which defines the refractive index $n_{ep}(\theta_c)$ for the extraordinary pump wave as

$$\frac{1}{n_{ep}^2(\theta_c)} = \frac{\sin^2\theta_c}{n_{ep}^2} + \frac{\cos^2\theta_c}{n_{op}^2}, \tag{4.5}$$

where n_{ep} and n_{op} are the principal extraordinary and ordinary refractive indices at the pump wavelength [60]. The angle α_{int} is constant for all signal wavelengths, whereas Θ_{int}, hence Ω, depends on the signal wavelength. For a broadband signal spectrum, the corresponding wave vectors will be angularly dispersed as shown in Fig. 4.1. The phase matching condition in this case becomes a vector equation, $\vec{k_p} = \vec{k_s} + \vec{k_i}$, so that, when projected on directions parallel $(\|)$ and perpendicular $(\perp)$ to the signal wave vector, it reads

$$\begin{aligned} \Delta k_\perp &= k_p \cos\alpha_{int} - k_s - k_i \cos\Omega \\ \Delta k_\| &= k_p \sin\alpha_{int} - k_i \sin\Omega \end{aligned} \tag{4.6}$$

If the signal frequency increases by $\Delta\omega$, the idler frequency decreases by $\Delta\omega$ and the wavevector mismatches along the two directions can be approximated, to first order, as

$$\Delta k_\perp \cong -\frac{\partial k_s}{\partial \omega_s}\Delta\omega + \frac{\partial k_i}{\partial \omega_i}\cos\Omega\,\Delta\omega - k_i \sin\Omega\,\frac{\partial\Omega}{\partial\omega_i}\Delta\omega \tag{4.7}$$

$$\Delta k_\| \cong \frac{\partial k_i}{\partial \omega_i}\sin\Omega\,\Delta\omega + k_i\cos\Omega\frac{\partial\Omega}{\partial\omega_i}\Delta\omega \tag{4.8}$$

To achieve broadband phase matching, both $\Delta k_\perp$ and $\Delta k_\|$ must vanish. Upon multiplying Eq. 4.7 by $\cos\Omega$ and Eq. 4.8 by $\sin\Omega$ and adding the results, we get

$$\frac{\partial k_i}{\partial \omega_i} - \cos\Omega\,\frac{\partial k_s}{\partial \omega_s} = 0 \tag{4.9}$$

which is equivalent to

$$v_{gs} = v_{gi}\cos\Omega, \tag{4.10}$$

where $\frac{\partial k_s}{\partial \omega_s} = v_{gs}$ and $\frac{\partial k_i}{\partial \omega_i} = v_{gi}$ are the group velocities of the signal and idler pulses, respectively. This is the condition for broadband phase matching NOPA for first order. Similarly the Eqs. 4.7 and 4.8 can be further expanded to the second order in order to find a condition for unltrabroadband phase matching as detailed in [115].

Equation 4.10 allows us to determine the signal-idler angle Ω required for broadband phase matching; from a practical point of view, however, it is more useful to know the corresponding pump-signal angle α_{int}, which is given by

$$\alpha_{int} = \arcsin\left(\frac{1 - v_{gs}^2/v_{gi}^2}{1 + 2\,v_{gs}\,n_s\,\lambda_i/v_{gi}\,n_i\,\lambda_s + n_s^2\,\lambda_i^2/n_i^2\,\lambda_s^2}\right)^{1/2} \tag{4.11}$$

4.2 Idler generation using NOPA

Figure 4.2 shows the calculated phase matching angles ($\theta_c = \theta_{pm}$) as a function of signal wavelength for type-I NOPA in the BBO at $\lambda_p = 395$ nm. It reveals a broadband amplification (approx. 550–900 nm) for a value of α_{int} in the range of 3.5–3.7 degree and $\theta_c \approx 31^\circ$. The resulting idler, for this case, can reach the desired NIR spectral range we are aiming for in our system (cf. Eq. 4.1). These calculations of phase matching angle, however, can only provide an estimate of the bandwidth that can be achieved under first order approximation. In order to do a complete characterization of OPA dynamics the coupled-wave equations (cf. [60, 116]) have to be solved for the real experimental scenario taking into account all possible phenomena which may affect the OPA process. As a first approximation we performed 1-D simulations* for the NOPA

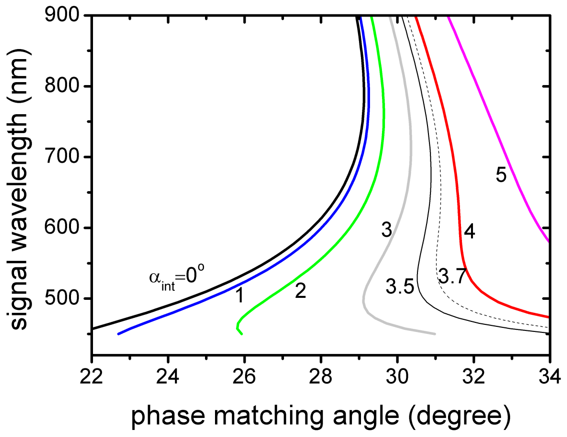

Figure 4.2: Phase-matching curves for a non-collinear type-I BBO OPA pumped at 395 nm, as a function of the pump-signal internal non-collinear angle α_{int}.

---

*Courtesy of Stefan Karsch and Zsuzsanna Major, MPQ, Hans-Kopfermann-Str. 1, 85748 Garching, Germany; Department für Physik, Ludwig-Maximilians-Universität München, Am Coulombwall 1, 85748 Garching, Gerby solving the three coupled-wave equations [60] taking into account the depletion of the pump energy and the phase mismatch between the three waves. However other effects, e.g. group velocity dispersion, spatial walk-off between the interacting beams and beam-profile effects etc. are not considered (therefore 1-D). This approximation provides a rough estimate of the amplification behaviour in our system. The OPA is pumped with the second harmonic of the Ti:sapphire source, which is centred at 395 nm, and the seed beam is assumed to be of Gaussian shape in frequency space resulting in a bandwidth ranging from 500 to 900 nm. The available pump energy was assumed to be $\sim$300μJ; the pulse duration of the pump was taken to be 100 fs. Using a seed energy of $\sim$50 μJ in $\sim$80 fs, our OPA calculations in a 350-μm-thick BBO crystal yielded the following results. While the broadband amplified spectrum is shown in Fig. 4.3(a), Fig. 4.3(b) shows the corresponding idler intensity spectrum, which clearly covers the spectral range we are aiming for. According to our calculations, the idler pulse energy can be up to $\sim$50 μJ. The best amplification conditions could be obtained for $\alpha_{int} = 3.5°$ and a corresponding phase-matching angle of 31.2°.

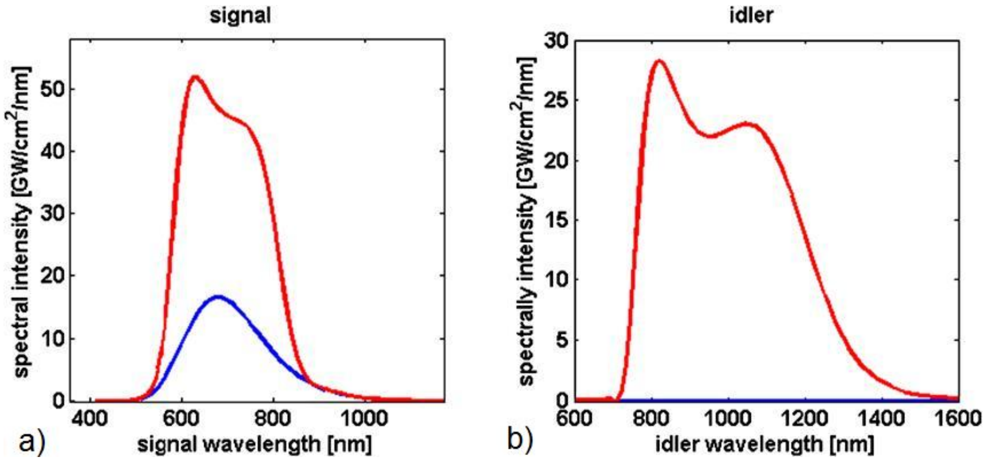

Figure 4.3: Calculated spectral intensity of the amplified signal (**a**) and the corresponding idler (**b**) resulting from NOPA in a BBO crystal, pumped at 395 nm. The blue curves represent the input spectra, the red curves are the spectra after amplification (picture courtesy of [65]).

Although the calculated energy is enough for seeding the OPCPA chain of the PFS, the generated broadband idler exhibits significant angular chirp due to the law of conservation of momentum as shown schematically in Fig. 4.1. Full compensation of this angular chirp is required if this beam is to be used for further amplification. Since, on one hand, with a widespread distribution of exit angles it is impossible to propagate this beam. On the other hand, when focused, it can lead to a significant distortion of the spatio-temporal beam profile in the far field (as discussed in Chapter 2), hence inefficient gain. In order to compensate this angular chirp a

---

many.

telescope–grating scheme was demonstrated by Shirakawa et al. [63]. Here the exit face of the OPA crystal is imaged on a diffraction grating (Fig. 4.4). The magnification factor (M) of the imaging telescope as well as the grating parameters are adjusted such that the angular dispersion of the idler beam could match with that of the grating, to get a collimated beam after diffraction.

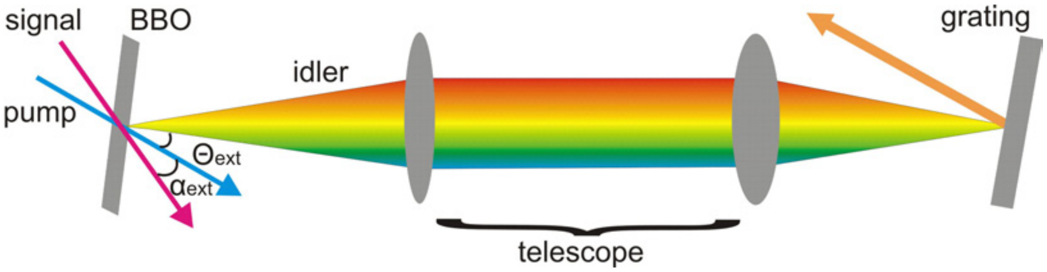

Figure 4.4: Principle of an angular dispersion compensator based on a telescope and a grating. For clarity the imaging optics of the telescope are represented by lenses in this schematic picture, although in our setup they are mirrors as will discussed later in the text. α_{ext}: pump-signal non-collinear external angle; Θ_{ext}: external angle between the ilder and pump wave vectors.

In the following we present the design consideration of this compensator. We will also discuss the extent of angular chirp compensation of the scheme used in [63]. A method for further improvement of this design will also be discussed. Based on this design, the results of our preliminary experimental observations will be presented, as were earlier reported in [65].

4.2.1 Design considerations

As can be seen from Fig. 4.1, the generated idler angle Θ_{int} is related to α_{int} as

$$k_s \sin\alpha_{int} = k_i \sin\Theta_{int}. \tag{4.12}$$

This yields

$$\Theta_{int} = \arcsin\left(\frac{n_s\lambda_i}{n_i\lambda_s}\cdot\sin\alpha_{int}\right), \tag{4.13}$$

where n_s, n_i are the refractive indices in the nonlinear crystal of signal and idler beams, respectively. Using Snell's law to determine the required external idler angle (Θ_{ext})

$$\Theta_{ext} = \arcsin\left(n_i \sin\Theta_{int}\right) = \arcsin\left(\frac{n_s}{\lambda_s}\lambda_i \sin\alpha_{int}\right) \tag{4.14}$$

Substituting $\omega = 2\pi c/\lambda$ in Eq. 4.1 we get

$$\frac{\lambda_i}{\lambda_s} = \frac{\lambda_i}{\lambda_p} - 1 \tag{4.15}$$

The Eq. 4.14 can therefore be rewritten as

$$\Theta_{ext} = \arcsin\left(\frac{n_s}{\lambda_p}\sin\alpha_{int}\cdot\lambda_i - n_s\sin\alpha_{int}\right) = \arcsin\left(B_0\,\lambda_i + B_1\right), \tag{4.16}$$

where $B_0 = \frac{n_s}{\lambda_p}\sin\alpha_{int}$ and $B_1 = -n_s\sin\alpha_{int}$.

The external angular distribution of the idler in the plane of propagation of the interacting beams is then given by

$$\frac{\partial\Theta_{ext}}{\partial\lambda_i} = \frac{B_0}{\left(1-(B_0\lambda_i+B_1)^2\right)^{1/2}} \tag{4.17}$$

Figure 4.5 shows the resulting external angular distribution as a function of wavelength of the idler beam for our experimental case where the pump wavelength is 395 nm and the non-collinear angle is close to α_{int} = 3.7°.

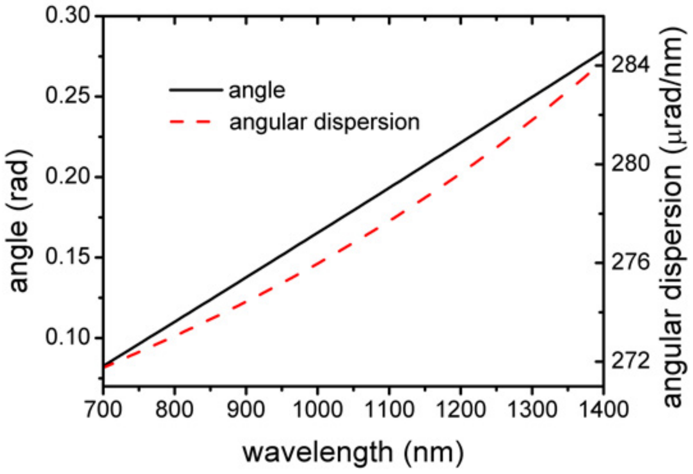

Figure 4.5: Idler angle (Θ_{ext}) and angular dispersion $\left(\frac{\partial\Theta_{ext}}{\partial\lambda_i}\right)$ from NOPA in a BBO crystal pumped at 395 nm. For our spectral range of interest (i.e. 700–1400 nm) an average angular chirp of 278 μrad/nm corresponds to a deviation in the propagation direction of up to 10° ($\sim$0.17 rad).

The angular distribution of an initially collimated beam after a diffraction grating of line density N, for the first-order of diffraction (m=1), can be obtained from the grating equation (recalling Eq. 2.2)

$$\beta(\lambda) = \arcsin\left(N\lambda - \sin\alpha\right) \tag{4.18}$$

where α and $\beta(\lambda)$ are the incident and diffracted angles, respectively. By equating the resulting angular distribution from the NOPA (Eq. 4.16) with that from the diffraction grating (Eq. 4.18) we can obtain the residual angle R after the compensator as

$$R(\lambda_i) = \Theta_{ext}(\lambda_i) - M\cdot\beta(\lambda_i) + \text{constant}. \tag{4.19}$$

The residual angular chirp after the compensator can be written as a Taylor series expanded around the central wavelength of the idler spectrum, λ_{io}. Considering terms up to second order in the Taylor series and diffraction by the grating into the first order (n = 1), these expressions read

$$\begin{aligned} R(\lambda_i) \approx R(\lambda_{i0}) &+ \left(\left.\frac{\partial \Theta_{ext}}{\partial \lambda_i}\right|_{\lambda=\lambda_{io}} - M \cdot \left.\frac{\partial \beta}{\partial \lambda_i}\right|_{\lambda=\lambda_{io}} \right) (\lambda_i - \lambda_0) \\ &+ \left(\left.\frac{\partial^2 \Theta_{ext}}{\partial \lambda_i^2}\right|_{\lambda=\lambda_{io}} - M \cdot \left.\frac{\partial^2 \beta}{\partial \lambda_i^2}\right|_{\lambda=\lambda_{io}} \right) \frac{(\lambda_i - \lambda_0)^2}{2!} + \text{constant}; \end{aligned} \tag{4.20}$$

where

$$\left.\frac{\partial^2 \Theta_{ext}}{\partial \lambda_i^2}\right|_{\lambda=\lambda_{io}} = \left.\frac{B_0^2 (B_0 \lambda_i + B_1)}{\left(1 - (B_0 \lambda_i + B_1)^2\right)^{3/2}}\right|_{\lambda=\lambda_{io}}, \tag{4.21}$$

$$\left.\frac{\partial \beta}{\partial \lambda_i}\right|_{\lambda=\lambda_{io}} = \left.\frac{N}{\left(1 - (N \lambda_i - \sin\alpha)^2\right)^{1/2}}\right|_{\lambda=\lambda_{io}}, \tag{4.22}$$

$$\left.\frac{\partial^2 \beta}{\partial \lambda_i^2}\right|_{\lambda=\lambda_{io}} = \left.\frac{N^2 (N \lambda_i - \sin\alpha)}{\left(1 - (N \lambda_i - \sin\alpha)^2\right)^{3/2}}\right|_{\lambda=\lambda_{io}}. \tag{4.23}$$

In the above calculation of the expansion coefficients, we have assumed the dependence of n_s on λ_{io} to be constant, which allows us to neglect the partial derivatives of n_s. With the external idler angle Θ_{ext} (Eq. 4.16), we can see from Eq. 4.20 that for a given grating (N and the corresponding incident angle α), the linear term of the angular chirp vanishes if the magnification of the telescope is chosen appropriately. If we allow for an arbitrary grating constant, M and N can be chosen at a given α so that both the linear and the quadratic terms vanish in the above expressions. However, this analysis does not account for any higher-order terms, since there are only two free parameters (M and N), allowing for the control of at most two orders. This is also the reason why our series expansion is truncated at the second order. The residual angular spread resulting from these first two terms amounts to a few mrad, which can be obtained by inserting the parameters from our experimental design into Eq. 4.19. For applications that target a small overall bandwidth this purely analytical approach might be sufficient, but for our ultra-broadband case the residual errors are too large. Hence, we applied an alternative approach to find the optimum values for the magnification factor of the telescope and the grating constant, for which also the higher-order terms are reduced. Using a least-squares fit we minimized Eq. 4.20 and thereby obtained optimum values for M and N, for which all orders have a combined minimum contribution to the residual angular spread. Note that the shapes of the resulting residual angular dispersion curves sensitively depend on the wavelength range used for the fitting. In our calculations, we chose the wavelength range to be 700–1550 nm, which corresponds to the signal wavelength range of 530–900 nm.

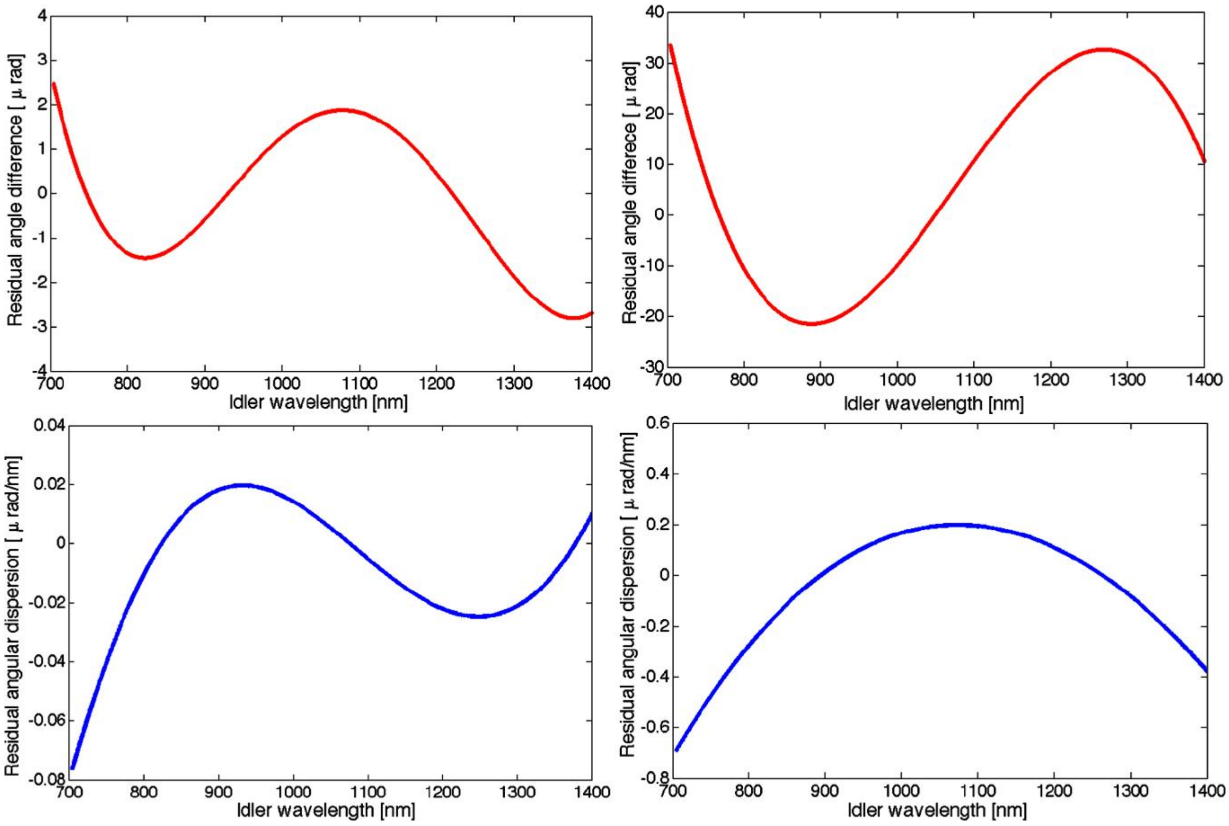

Figure 4.6: Residual angular spread (top) and angular dispersion (bottom) resulting from the least-squares fitting. The left-hand column shows the results of the best fit when the grating constant is also a fit parameter, the right-hand column shows the results when the grating line density (N) is kept fixed at 300 lines/mm, (courtesy [65]).

For our idler with a central wavelength of 1100 nm and a 600-nm spectral bandwidth, the fitting results in an optimum groove density of 221 lines/mm for the grating and a magnification factor of 1.22 for the telescope. The corresponding angle of incidence is $\alpha = -2^\circ$. The residual angle difference is at most $\sim$3 μrad and the corresponding angular dispersion is less than 0.04 μrad/nm as shown in the left-hand column of Fig. 4.6. This optimized residual angular dispersion is two orders of magnitude smaller than that reported in Ref. [63]. However, such a specialized grating may be hard to come by. We have therefore investigated the case of a commercial grating with 300 lines/mm. For this fixed grating constant the optimum magnification of the telescope is 0.91, the angle of incidence is $\alpha = 6.7^\circ$ and the calculated residual angular spread and angular dispersion curves are depicted in the right-hand column of Fig. 4.6. From these we can see that the residual angular dispersion is $\sim$50 μrad, and thus still one order of magnitude below than that in Ref. [63].

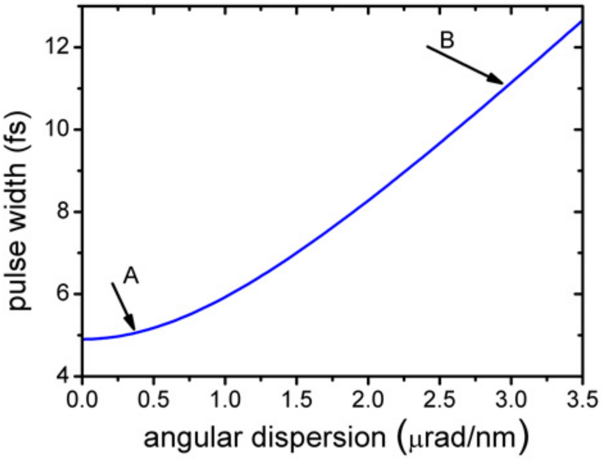

Figure 4.7: Effect of angular dispersion on the pulse duration in the focus according to Eq. 2.15. 'A' indicates the case of 0.4 μrad/nm residual angular chirp with the 300 lines/mm grating, 'B' corresponds to the case reported in [63] using a grating with 600 lines/mm. A transform-limited pulse with 300-nm spectral bandwidth, 1-mm beam size in FWHM, at the central wavelength of 1000 nm is considered in the calculation.

As discussed in Chapter 2 (Sec. 2.2.4), when an angularly chirped pulse is focused, even a small angular chirp can lead to a significant temporal broadening of the pulse as well as a reduction of the peak intensity at the focus spot. Using Eq. 2.15, we can now estimate the effect of the residual angular chirp for the different cases we have investigated. In Fig. 4.7 the resulting pulse duration is shown as a function of angular chirp in the beam. We have assumed a pulse with a Gaussian spectrum with 300-nm bandwidth, i.e. 4.9-fs transform-limited pulse duration, a beam size of 1 mm in FWHM (Gaussian) and a central wavelength around 1000 nm. With 0.4 μrad/nm angular dispersion (corresponding to the 300 lines/mm grating) the pulse duration increases by 4% to ∼5.1 fs as marked by 'A'. However, the same pulse is stretched to ∼11-fs duration if the angular chirp is one order of magnitude higher as in the case reported in Ref. [63], indicated by 'B'. We have also verified the validity of our fitted results using the 221 and 300 lines/mm gratings for a realistic experimental situation modelled by ray-tracing analysis using the code RAYTRACE [91].

This rather simple angular dispersion compensation scheme based on a telescope and a diffraction grating cannot exactly compensate the entire angular chirp of the idler beam. However, for cases when 0.4 μrad/nm residual angular dispersion, corresponding to a few tens of μrad in angular spread, is still too large for the respective applications, this remainder can be compensated using a deformable mirror placed in the Fourier plane of the telescope. The necessary deformation could be achieved in practice with a commercial mirror (e.g. [117]), which can introduce a maximum correction angle around ±320 μrad with a maximum stroke of 8 μm, resulting in a maximum correctable gradient of 0.2 μm. Thereby, this simple scheme could easily be extended such that even higher orders of the angular dispersion can be fully compensated.

4.2.2 Experimental setup for idler generation using NOPA

Figure 4.8 shows the schematic experimental setup for the idler generation in the NOPA followed by the angular chirp compensation. We used the Femtopower output after HPC (cf. Sec. 3.1.3), delivering up to 1.5-mJ pulses with a duration of around < 25 fs centred around 790 nm. After passing through a focusing lens L (f = 1.5 m) the beam was divided into two parts by a beam splitter BS (65/35). The reflected part propagated through a vacuum spatial filter (VSF) and was collimated by a spherical silver mirror SM1 (f = 1 m) after its exit. A reflective type telescope (T) was used to change the beam size. After a thin BBO crystal (120 μm) cut for Type-I frequency doubling at 800 nm ($\theta_c = 29.2°$), four dielectric mirrors (DM1–4) coated for maximum reflectivity at 400 nm were used to separate the fundamental beam from the second harmonic, which was then used to pump the NOPA stage. The fraction of the pulse, which was transmitted through the beam splitter, was spectrally broadened in a filament in a gas cell (GC) filled with argon at a pressure of 2 bar. An iris was used to select the central part of the beam after having formed a single filament. After collimation by a spherical silver mirror (SM2) with f = 1.25 m and a delay line (DS), the white light was used to seed the NOPA. We used a 500-μm thick Type

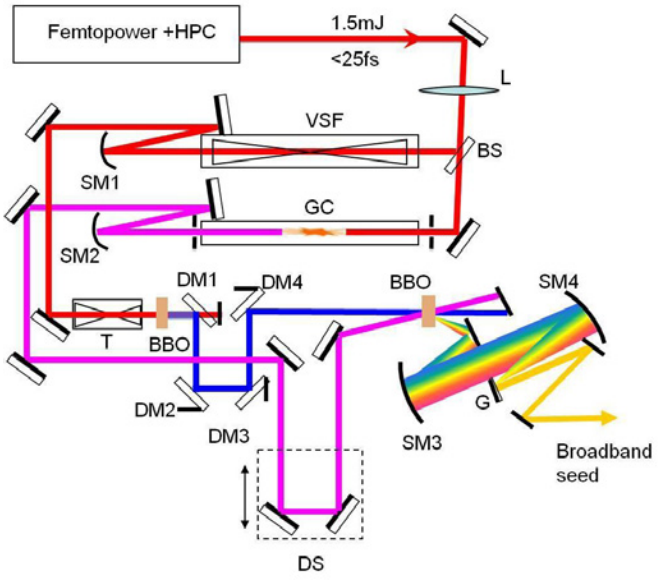

Figure 4.8: Schematic layout of the experimental setup. HPC: hybrid pulse compressor; L: lens; BS: beam splitter; VSF: vacuum spatial filter; SM1–4: spherical mirrors; T: telescope; DM1–4: dielectric mirrors; GC: gas cell; DS: delay line; G: diffraction grating. See text for details.

I BBO crystal ($\theta_c = 31^\circ$) and an internal non-collinear angle of around 3.7° between the pump and seed directions. In addition to the amplified broadband pulse, an angularly dispersed idler was generated. The idler was first deflected by a silver-coated rectangular mirror guiding it into an imaging telescope which consisted of two spherical silver mirrors SM3, 4 (radius of curvature = 400 mm, 365 mm). The telescope imaged the NOPA crystal onto an N=300-lines/mm diffraction grating (G), which was used to compensate the angular dispersion. After the compensator the collimated idler was picked out by another flat silver mirror.

We measured a total pulse energy of 3 μJ of the idler after passing through the compensator setup, with a pump energy of $\sim$160 μJ and an input seed energy of 40 μJ. The seed pulse was amplified to 60 μJ. Although we get more $\sim$15 μJ of idler after the crystal, the major loss is contributed by the lossy grating. The typical spectra for the input seed signal, amplified signal and compensated idler are shown in Figs. 4.9, measured with a combined visible-NIR

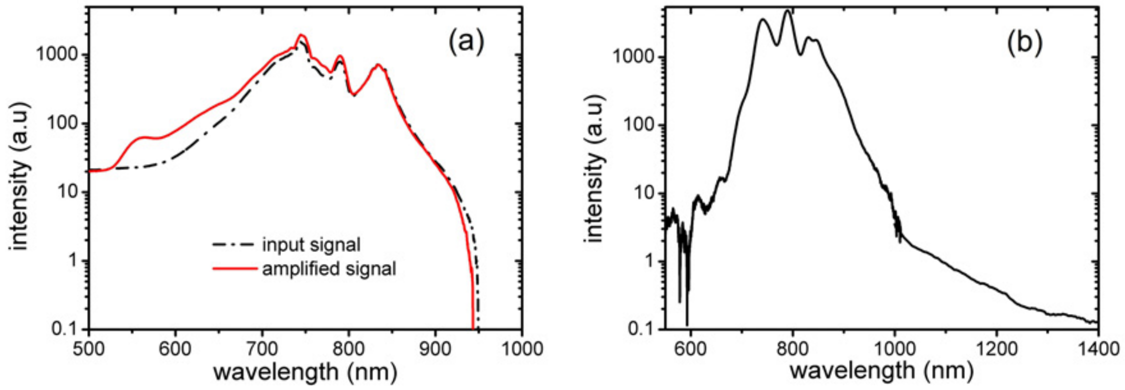

Figure 4.9: (a) Measured spectrum of the seed pulse before (black) and after (red) amplification in the NOPA; (b) Measured spectrum of the idler after the angular dispersion compensator.

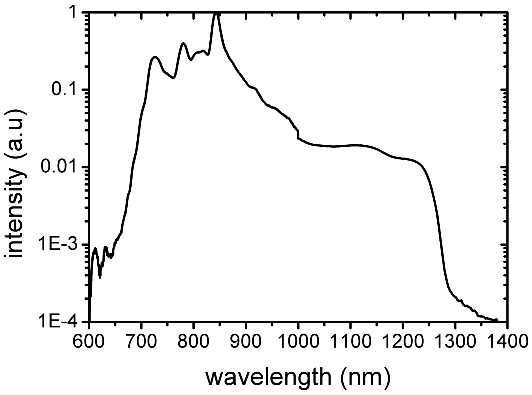

Figure 4.10: Measured spectrum of the idler before the angular dispersion compensator, by replacing the Ar-filament cell (GC in Fig. 4.8) with an Ar-filled hollow core fiber.

spectrometer (AvaSpec-NIR256-1.7). Note that the ‘kink’ in the idler spectrum originates from the overlapping region between the ranges of the two spectrometers. From Fig. 4.9(b) we can see that the generated idler ranges from below 700 nm up to around 1400-nm wavelength. However, the spectral intensity in the NIR tail of the idler spectrum is up to four orders of magnitude lower than its peak around 800 nm, originating firstly from the amplification process itself and secondly from the diffraction efficiency of the grating. In an improved experimental setup the first issue could be overcome by increasing the spectral intensity of the seed at lower wavelengths, where the filament only provides an exponential tail, by using an HCF instead of a filament for spectral broadening. Alternatively, or in addition, the amplification in the NOPA stage can be tuned such that the low-intensity, low wavelength part of the seed experiences a very high gain, while the rest of the spectrum is already in saturation as shown in a similar setup in [118]. This would result in an increase in the long-wavelength part of the idler and thereby lower the intensity variations across its entire spectral range. As a preliminary test of this claim, we replaced the Ar-filament cell with an Ar-filled HCF with the similar input energies. This improvement resulted in a significantly better seed spectrum in the spectral tail below 650 nm than that of the filament. We were able to amplify the 70 μJ input seed energy to ~95 μJ, with the idler energy similar to that of the previous case. However the idler spectrum before compensator was significantly improved in terms the energy of its NIR-tail (Fig. 4.10).

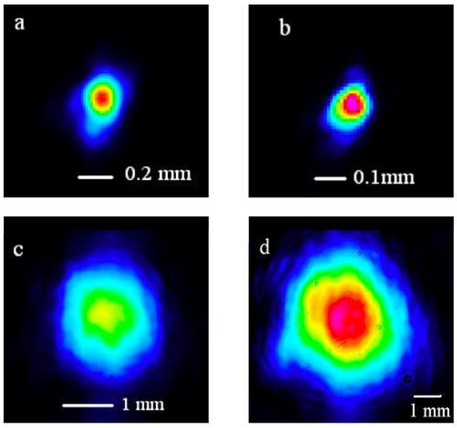

Figure 4.11: Beam profiles of seed and compensated idler: (a) the focused beam pattern from the modified Femtopower Pro; (b) the compensated idler at the focus; (c) and (d) the patterns at near field and far field at 1-m distance without focusing.

In order to assess the capability of our optimized angular dispersion compensation setup the beam profiles were recorded with a CCD camera (WinCamD) device after passing through the compensator and are shown in Fig. 4.11. For comparison, Fig. 4.11a shows the focal spot of the output of the PFS front end measured at the VSF. Fig. 4.11b shows the focus of the idler beam with ∼2-mm diameter after the compensator when focused by a lens with f = 12.5 cm. After the compensator, when the residual angular chirp seems to be minimized, the beam is divergent. The profiles of the near field and the far field (after 1 m of propagation) of this beam are shown in Fig. 4.11c and d, respectively. Although the silicon-based chip of the CCD camera which was used is not sensitive to spectral components above ∼1000 nm, and in spite of the low intensity of the NIR tail of the idler spectrum, we can conclude from the observed beam profiles that the angular chirp of the idler has been compensated in the detected range of the spectrum. For an uncompensated angular dispersion we would observe a significant broadening along one dimension of the beam profile after some propagation, even for the limited bandwidth that we are able to detect with this method. However, with this equipment it is not possible to quantitatively determine and therefore minimize the residual angular chirp after compensation. For this, additional measurements would be necessary, such as quantitatively measuring the angular dispersion of the idler using a technique based on spectrally resolved interferometry [119].

In the following we discuss the schemes of cascaded direct spectral broadening by self-phase modulation (SPM) in gases, using the Femtopower output pulses. The results of the NOPA idler generation will be compared with that of the cascaded spectral broadening.

4.3 Broadband seed generation using cascaded spectral broadening

We have used the Femtopower output pulses with an energy of ∼1.5 mJ and pulse duration of < 25 fs centred at $\lambda_0 = 790$ nm to generate a broadband supercontinuum using SPM as the dominant process. Since the required seed spectrum, ranging from 700–1400 nm, is difficult to achieve with such pulses in a single spectrum broadening stage, therefore we adapted a cascaded spectrum broadening scheme. The first stage is used to generate few-cycle pulses from the Femtopower output by spectral broadening in the HCF and subsequent compression using chirped mirrors. The few-cycle pulses are then used to generate an ultrabroadband supercontinuum using filamentation in argon (named HCF-filament) or a second HCF (Cascaded HCF).

First, a brief overview of different processes contributing to spectral broadening in the gaseous media is presented. This is followed by the description of few-cycle pulse generation with the Femtopower output. Finally, we present the broadband supercontinuum generation with few-cycle pulses by filamentation in an argon cell (HCF-filamentation) as well as in a second HCF (cascaded-HCF).

4.3.1 Spectral broadening in gaseous media

As discussed in Chapter 3, the refractive index of a medium in the presence of an intense electromagnetic field depends not only on its frequency, but also on the space and time dependent intensity $I(r,t)$ of the laser according to the Eq. 3.18. For a typical non-uniform intensity profile with a maximum on axis, this intensity dependent refractive index $\Delta n(I)$ causes the intense beam to collapse to reduced size, which in turn results in enhancing its peak intensity to even higher level, and so on. This self-focusing effect therefore acts like a succession of increasingly converging lenses as shown in Fig. 4.12(a). In the absence of any defocusing effect, this would quickly lead to a beam collapse when the peak power exceeds a critical power P_{cr} as defined in Eq. 3.20. However, in addition to this self-focusing effect, there is a defocusing phenomenon due to the combined effect of natural diffraction and the refraction from the electron plasma created by the ionization of the gas atoms at such high intensities. The generation of a plasma involves a local reduction in the refraction index [120, 121], which in a linear approximation is given by $\Delta n_\rho = -\frac{\rho(r,t)}{2\rho_c}$, where $\rho\,(r,t)$ denotes the density of free electrons; $\rho_c = \varepsilon_0 m_e \omega_o^2/e^2$, the value of the critical plasma density above which the plasma becomes opaque; m_e, the electron mass; and e, the electron charge. This reduction in refractive index acts as a divergent lens (cf. Fig. 4.12(b)), hence preventing the complete collapse of the beam on itself. According to the simple model of Braun et al. [122], a stable balance between these focussing and defocusing effects results in self-channelling through the medium. This phenomenon is generally referred as optical filamentation. In this picture, unbalance eventually occurs due to the nonlinear energy losses during the generation of the plasma, terminating the self-channelling at a finite length. The length of the optical filament depends on a number of parameters: e.g. nature of the gas, gas pressure, input pulse width, initial chirp of the pulse, spatio-temporal beam profile of the input pulse etc., see [58] for more details. The length of the optical filament under given condition can be further extended using artificial guiding media such as HCF [57].

The temporal variation of the laser intensity $I(r,t)$ under such circumstances causes a temporal variation of the refraction index, which in turn results in the appearance of new frequencies in the spectrum of the laser pulse. This effect is called self-phase modulation (SPM). The simplest model describing this phenomenon relates the instantaneous frequencies $\omega\,(t)$ to the pulse intensity as follows [58]

$$\omega\,(t) = \omega_0 - \frac{n_2 \omega_0 \ell_{SPM}}{c} \frac{\partial I\,(r,t)}{\partial t}. \tag{4.24}$$

The generation of new frequencies thus depends on the slope of the pulse intensity $I\,(r,t)$, the propagation distance ℓ_{SPM} in the optical medium and its nonlinear index coefficient n_2. Since the intensity exhibits positive slope for the front half of the pulse in time domain, therefore the redder frequencies are generated during this part of the pulse, while the blue ones are created in the second half. The SPM plays a significant role in generating a broadband continuum covering

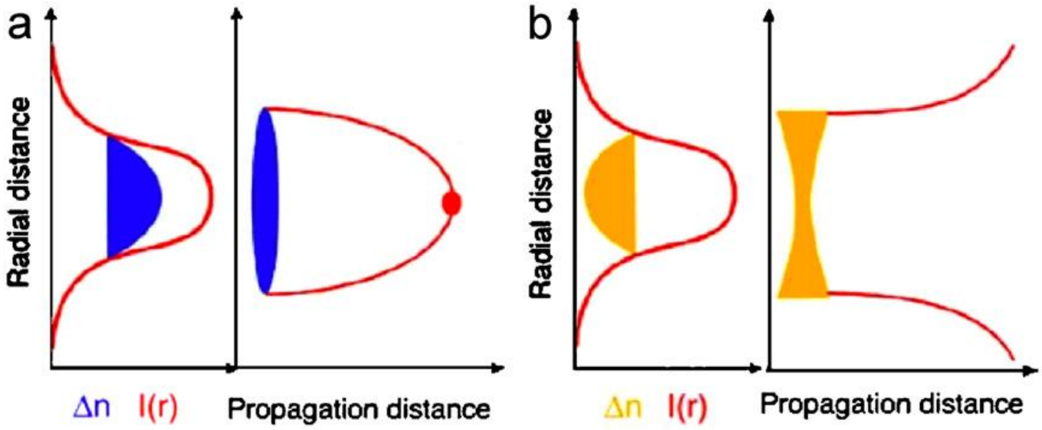

Figure 4.12: (a) *Self-focusing of an intense beam by the optical Kerr effect*: When the power of a beam exceeds critical power P_{cr} (Eq. 3.20), it leads, in the absence of other nonlinear effects, to a collapse on itself. (b) *Plasma defocusing*: The ionization of a medium creates an under-dense plasma which decreases its local index, hence causing the beam to defocus. This picture is the courtesy of [121].

the visible and extending towards the infra-red spectral domain. Within a simple approximation described in [123, 124] the spectral broadening due to the SPM during filamentation is proportional to the inverse of the pulse duration, meaning the shorter the pulse, the broader the generated spectrum. However in addition to the SPM there are several other effects contributing to the spectral broadening [58], e.g. self-steepening, ionization of the medium, four-wave mixing etc. Laser pulse self-steepening [125] occurs because the velocity of the peak intensity of the pulse is smaller than that of the trailing edge of the pulse, due to the intensity dependent change of refractive index $\Delta n(I)$. For $\Delta n(I)$ positive and instantaneous, the light velocity decreases with increasing laser intensity. Starting from a Gaussian pulse, the peak is slowed down with respect to the pulse group velocity while the trailing part catches up with the peak, leading to the formation of a steep edge in the trailing part of the pulse. This effect leads to a faster self-focusing of the trailing part of the pulse (in comparison with the leading part) and to an increase of the bluer frequencies generated in the steep trailing part [126]. Self-steepening may eventually lead to asymmetric pulse splitting [109, 127]. This pulse splitting in turn results in steepening of the leading part particularly for few-cycle incident pulse, owing to their comparatively higher sensitivity on the GDD, hence generating new redder spectral components [82, 128]. In case of four-wave mixing process, the intermixing of at least two different spectral components of the pulse in a nonlinear medium generates a new frequency [129]. Depending upon the frequencies of the interacting waves this process may contribute the blue shift or red shift (or both) to the pulse spectrum, e.g. $2\omega + \omega \to 3\omega$, $2\omega_1 - \omega_2 \to \omega_3$ etc. For detailed realization of basic mechanisms of spectral broadening in optical filamentation see [58].

From literature, e.g. [58, 121, 124, 130, 131, 132, 133, 134, 135, 136], it can be seen that the input pulses of few-10 fs with carrier frequency at $\sim$ 800 nm does not show significant broadening into the infrared. This asymmetry in the broadband spectra is due to the fact that in addition to the classical SPM effect other processes such as pulse-steepening, ionization of gas atoms etc. also contribute to the blue shift. Most recent theoretical analysis of Luc Bergé* reveal that for sub-two cycle pump pulses at high enough power the redshift in filamentation first develops in a classical SPM broadening stage, followed by a second enhancement induced by sharp leading edges that marks the temporal pulse profile. Initiated by plasma defocusing and strong group velocity dispersion effects, this two-peaked profile preserves a focused front over a long distance, which is associated with the largest redshift in the spectrum (cf. Appendix D). Furthermore, these calculations predict that the phase of the broadband supercontinuum pulse is a single-valued function of angular frequency. Therefore it is expected to be compressible close to the transform-limit, and it can be potentially employed for seeding the OPCPA chain. We therefore use sub-two-cycle to generate the required broadband supercontinuum suitable for seeding the OPCPA-chain of the PFS.

4.3.2 Experimental setup

The schematic layout of the OPCPA seed generation setup is shown in Fig. 4.13(a). The Femtopower output, exhibiting 1.5 mJ pulse energy and a pulse duration of <25 fs, was focused by a 2-m focal length lens (L_1) into a 300 μm-inner diameter and 1 m-long Ne-filled HCF (HCF1). The pulses are spectrally broadened in the HCF1 due to the intensity dependent nonlinear effects as discussed above. The broadband spectrum after the HCF1 is compressed down to approx. 5 fs in a chirped mirror compressor (CMC). These pulses are then coupled into an Ar-cell for the HCF-filament scheme, or a second Ne-filled HCF (HCF2) for the cascaded-HCF setup, in order to generate an ultrabroadband supercontinuum. The long-wavelength part of the spectrum (700–1400 nm) is subsequently stretched with negative dispersion in a prism pair stretcher (OPCPA seed stretcher).

In every laser system the direction of the output beam is subject to some beam pointing fluctuations, mainly, arising from the air turbulences, mechanical instability of the optomechanics and the long-term thermal drift of the laser cavities. Since the coupling of the laser beams into an HCF is very sensitive to the beam direction, such fluctuations may result in an instability of its output in terms of its beam profile, overall throughput and output spectrum [138]. Therefore, before coupling into the HCF1 we performed a beam pointing analysis of the output of the Femtopower system.

---

*CEA-DAM, DIF, F-91297 Arpajon, France

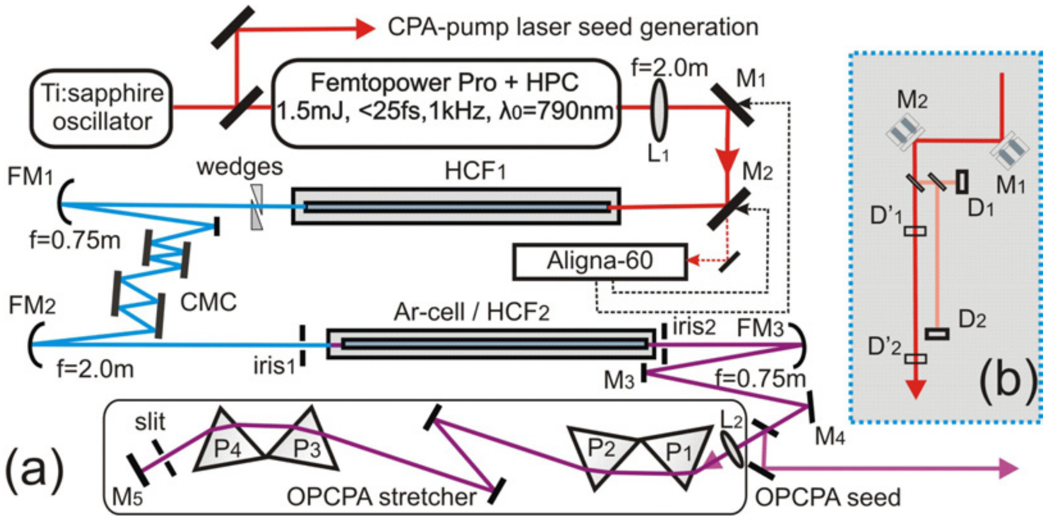
CPA-pump laser seed generation
Ti:sapphire oscillator
Femtopower Pro + HPC
1.5mJ, <25fs,1kHz, λ0=790nm
f=2.0m
M1
L1
M2
FM1
wedges
HCF1
f=0.75m
Aligna-60
FM2
CMC
Ar-cell / HCF2
iris2
FM3
f=2.0m
iris1
M3
f=0.75m
M4
slit
P4
P3
P2
P1
L2
M5
OPCPA stretcher
OPCPA seed
(a)
M2
M1
D1
D'1
D2
D'2
(b)

Figure 4.13: (a) Experimental setup for OPCPA seed generation using cascaded spectral broadening techniques. (b) Principle of 4D beam pointing stabilization: The mirrors M_1 and M_2 are mounted on two motor/piezo-actuated mirror holders. Four actuators control four degrees (4-D) of freedom, i.e. two translational, two angular. The electronics keeps the beam exactly at the center of the 2-D photosensitive detectors D_1 and D_2, which represent two points D_1' and D_2' of the laser beam, respectively [137]. FM: focusing mirror; Aligna-60: beam pointing stabilization system; P: prism; CMC: chirped mirror compressor; HPC: hybrid pulse compressor; HCF: hollow core fiber; L: lens; M: mirror.

Femtopower output beam pointing: measurements and stabilization

The beam pointing fluctuations of the Femtopower output have been measured using a WinCam-UCD12 (RayOptics Inc.) device in the far-field of the 2 m-focal length lens (Fig. 4.13(a)). The root mean square (RMS) deviations of the laser spot from its mean position were recorded for the time intervals of 5-10 second or 20 min. Each measurement was repeated for 10 times to calculate the mean RMS and standard deviation (σ). Our measurements show the RMS short-term pointing fluctuations of 3.2 ± 0.3 μrad (mean-RMS $\pm\sigma$) for a time scale of 5-10 sec and long-term drift of 6.75 ± 0.5 μrad for about 20 min. Under these conditions we observed noticeable changes in the spectrum shape and spatial beam profile at the output of the HCF for a time scale of few-minutes. A similar instability of the HCF-output spectrum originating from beam pointing fluctuations was reported by Kanai et al. [138]. Moreover it was impossible to couple the whole energy of our Femtopower system into the fiber for more than few minutes without damage to the entrance face.

In order to reduce these fluctuations, we used a commercial laser beam pointing stabilization system (Aligna-60, TEM-Messtechnik GmbH) as shown in Fig. 4.13. This system provides both the position and angle locking of the laser beam with four degrees (4-D) of freedom in space

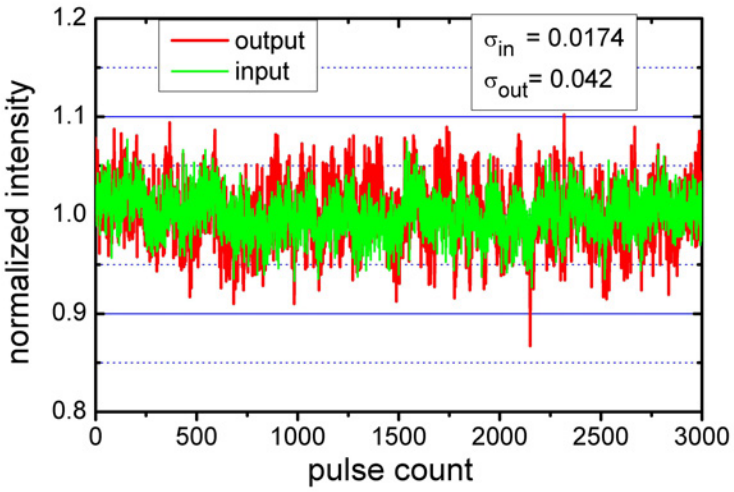

Figure 4.14: Measured shot-to-shot input and output powers of the HCF1.

using two position sensitive detectors via an active feedback loop control for the mirror M_1 and M_2, see Fig. 4.13(b). The mirrors M_1 and M_2 are driven by piezo actuators for fine control and by stepper motors for coarse alignment. This system provides both short- and long-term stability of the beam pointing at a level of less than 1 μrad. Figure 4.14 depicts the shot-to-shot stability of the HCF1 output after stabilization of the input beam pointing. For comparison, the shot-to-shot stability of the input pulses is also presented. These measurements have been taken by synchronously recording the input and output signals using two photo-diodes. The results reveal that the output power of the HCF1 remains stable for the whole course of the measurement. The calculated standard deviation of the input and output (σ_{in} and σ_{out}), averaged over a set of 3000 measured shots, is 0.042 and 0.017, respectively. The residual fluctuations do not exhibit any prominent change of output spectrum.

4.3.3 Generation of few-cycle light pulses

The pressure of the Ne in HCF1 was adjusted in a way to get maximum broadening in a stable output mode. Very fine adjustment of the programmable dispersion from the DAZZLER, which optimizes the chirp of the incident pulse, improved the throughput as well as the spectral broadening [139]. At an optimum pressure of 2.3 bar, an overall throughput of 650 μJ with the central mode containing more than 85% of the total energy was obtained. The broadband spectrum is shown in Fig. 4.16(a). The output of HCF1 was collimated by a 0.75 m focal length silver coated mirror (FM_1) and then compressed using the CMC. The CMC consists of specially designed double-angle dispersive mirrors (DADM's) to fine control the dispersion of broadband spectrum generated in HCF1. Since we demonstrated the implementation of these DADM's for few-cycle pulse compression for the first time, therefore before showing the pulse compression a brief introduction of these mirrors is presented as was reported in [140].

Double-angle dispersive mirror compressor for few-cycle pulses

Owing to their high control of GDD for an unprecedented bandwidth, chirped mirrors (CM) [103] are generally used to produce few-cycle pulses. The conventional CM, however, suffers from unavoidable spectral oscillations of the GDD which may adversely affect the quality of the few-cycle laser pulses being controlled with the CM. Generation of few-cycle nearly TL pulses using CM demands suppression of such oscillations as well as fine control of the dispersion for the whole spectral range of the chirped pulses. Among many schemes developed to dampen such oscillations [105, 141, 142, 143], or to minimize their influence on the pulse quality, the complementary-pair approach [105] is commonly employed. The mirrors in this approach are used in pairs with one having the GDD oscillations anti-phase to the other, hence resulting in a smooth dispersion when equal number of reflections are applied. Such complementary-pairs are manufactured in two separate coating runs, therefore a high precision of layer deposition is required during both runs in order to achieve the desired characteristics of the CM's. This drawback makes this approach more time consuming for manufacturing and costly compared to the mirrors for pulse compression that could be manufactured in a single run. In addition these complementary-pairs require very high accuracy of angle of incidence during pulse compression.

The newly developed DADM technology [140] rely on a single coating run for manufacturing. The GDD oscillations of a DADM changes their phase in spectral domain with respect to the angle of incidence [140, 144]. In this way two identical DADM's can be aligned at two different angles of incidence to achieve anti-phase GDD oscillations. Moreover a DADM relaxes the strict requirement of a very precise angle of incidence for pulse compression, as imposed by the complimentary-pair design, because here a slight deviation of the angle of incidence of one pair can be compensated by fine-tuning the angle of incidence of the other. For detailed realization of the design of these mirrors see [140]. The schematic sketch of this approach is depicted in Fig. 4.15(a), whereas the design curve of the DADM's is shown in Fig. 4.15(b). As indicated by the blue and red curves in Fig. 4.15(b), the phase oscillations of the same mirror for two different angles $\theta_1 = 5^\circ$ and $\theta_2 = 20^\circ$ exhibit a phase-shift of π, while the reflectivity remains more than 99% for the entire required spectral range. The effective GDD and reflectance of the DADM is the geometric mean of the GDD and reflectances, respectively for the described incidence angles. The optimum effective GDD exhibits residual oscillations which are an order of magnitude lower than those of a single reflection for each incidence angle. These residual oscillations show an insignificant influence on the pulse durations. The mirrors were designed

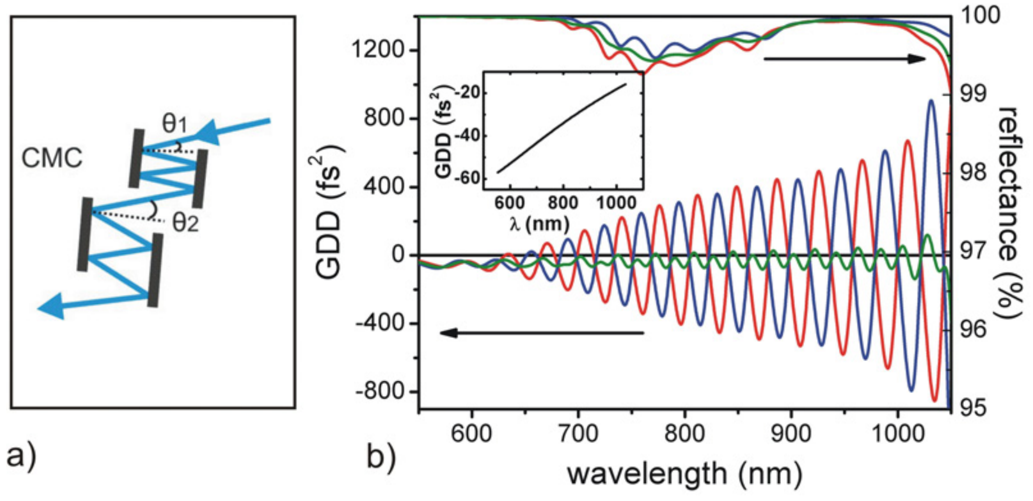

Figure 4.15: (a) Schematic of the double-angle dispersive mirror compressor. (b) Designed dispersion the DADM: Red and blue curves correspond to angles of incidence $\theta_1 = 5$ and $\theta_1 = 20$ degrees, respectively. Green curves show the effective GDD and reflectance. The inset depicts the target GDD of the double-angle DM, picture courtesy of Pervak et al. [140].

to roughly compensate the dispersion of two 0.5 mm fused-silica (FS) Brewster windows of the HCF1, 0.5 mm of (FS) wedges, and 1.7 m of air (or gas). The target design curve of the DADM for one bounce is shown in the inset of Fig. 4.15(b), which corresponds to the GDD and TOD of -35 fs^2, and -30 fs^3, respectively, at a central wavelength of $\sim$770 nm.

Figure 4.16(a) depicts the output spectrum of HCF1 for a Ne-pressure of 2.3 bar. In order to compress this spectrum we used a total of eight reflections on the DADM's. The compressor exhibited an overall throughput of $> 85\%$. The pulses after the compressor were characterized by a second-order interferometric autocorrelator (Femtolasers GmbH). The measured autocorrelation function is presented in Fig. 4.16(a). This corresponds to a FWHM of 4.3 fs, for sech^2 pulse shape, and is very close to the transform limited (TL) pulse duration of 4.2 fs, as calculated from the measured spectrum for the range of 550-1100 nm. The good agreement between the measured and calculated widths of the compressed pulses indicates that this new scheme of pulse compression is capable of delivering high quality few-cycle pulses by compensating their dispersion in a more simple and accurate way than other conventional techniques [105, 141, 142, 143].

These high quality few-cycle pulses after the chirped mirror compressor were used to generate the broadband supercontinuum by i) filamentation in argon, and ii) broadening in a second HCF. We call the former scheme “HCF-filament” since it follows prior broadening in an HCF (HCF1), similarly the latter is termed “cascaded-HCF”. In the following the details of our experimental findings for these two schemes are presented.

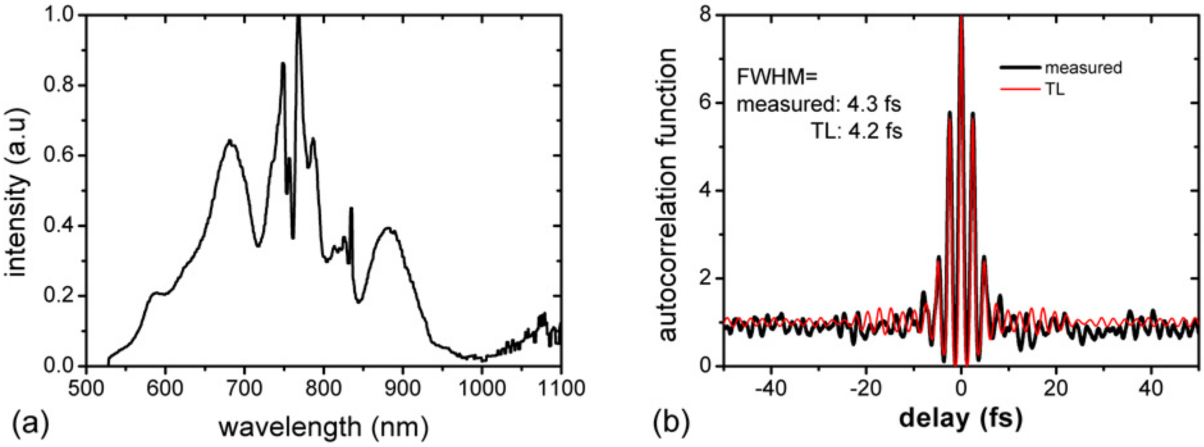

Figure 4.16: Few-cycle pulse generation: (a) HCF1 output spectrum at 2.3 bar. (b) measured and calculated autocorrelation of the compressed pulse.

4.3.4 HCF-filament

The sub-5-fs pulses with an energy of 450 μJ after the CMC were focused into a 158-cm long argon-cell (Ar-cell) by using a 2-m focal length silver coated mirror (FM$_2$) with a 1/e^2 beam diameter of 550 μm at the focus position (see beam profile in Fig. 4.17(a)). The focal plane of FM$_2$ was adjusted to the middle of the gas cell to maximize the beam size in the 0.5-mm-thick fused-silica (FS) entrance and exit windows and therefore avoid non-linearities. An iris was placed into the input beam of the Ar-cell in order to fine-control the spatial beam profile at the output of the Ar-cell. We observed the onset of multiple-filamentation at a pressure of >2 bar of Ar for the pulse energy of ~450 μJ. Fine adjustment of the iris at reduced pressure of 1.8 bar helped in obtaining a good quality spatial beam profile in a single filament. Under these conditions we were able to couple more than 400 μJ of the input pulse energy into the Ar-filament. A broadband supercontinuum containing 100 μJ energy in the central mode was observed at output of the cell (see Fig. 4.17(b)). The resulting broadband supercontinuum at the Ar-cell output was measured using the HR2000 (Ocean Optics), AvaSpec-3648 and AvaSpec-NIR256-1.7 (Avantes) spectrometers. Spectra were recorded at 1 m beyond the cell after an iris has been used to limit the beam to its central spot and cut its conical emission. This spot was then coupled into the entrance of the spectrometer. The generated spectrum is presented in Fig. 4.17(b), displaying evidence of a supercontinuum spanning more than two octaves and of a significant buildup of long wavelengths. A 2.3-fs TL pulse duration can be inferred from this spectrum, centered around 600 nm. About 55% of the supercontinuum energy is contained in the spectral range of 700-1400 nm. We further analysed the dependence of the spectral broadening of the infrared on the energy and gas pressure for sub-5 fs pulses.

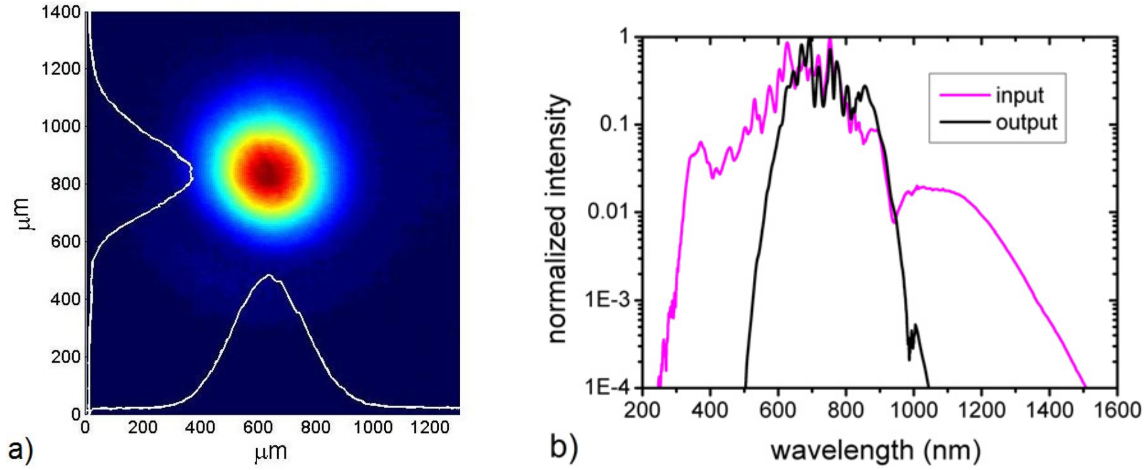

Figure 4.17: (a) Beam profile after the CMC in the far-field of the 2-m focal length silver mirror FM_2 with a 1/e^2 beam diameter of 550 μm. (b) Broadband supercontinuum generated by the filamentation of <5 fs 400 μJ pulse at 1.8 bar argon.

Pulse-energy dependence

In this part of the experiment we used the sub-5 fs pulse with different energies at fixed Ar-pressure of 1 bar. The pulse energy at the input of the Ar-cell was varied by placing an iris into the incident beam (Fig. 4.13(b)). The NIR-parts of the supercontinua are shown in Fig. 4.18(a), where an increase in the NIR tail with respect to the pulse energy can be realized. We can define a long-wavelength cut-off, where the spectral intensity drops to the 10^{-4} level of the normalized peak value. As shown in the inset of Fig. 4.18(a), the cut-off wavelengths increase with the pulse energy at fixed pulse duration and pressure. They shift from 1100 nm to 1300 nm when the energy is varied from 170 μJ to 450 μJ, respectively. The energy dependence of the cut-off wavelengths levels off around 400 μJ input energy, indicating that no further spectral broadening towards the NIR domain occurs. Since above this input energy multiple filamentation sets in, we can infer that the maximum NIR broadening for a single filament propagating over meter-range distances, at given pressure and focusing conditions, is obtained just below this threshold.

Ar-pressure dependence

Here the sub-5 fs pulses with fixed energy of 400 μJ are used to study the effect of pressure variation on the spectra generated by filamentation. The argon pressure was changed from nearly zero to 2.5 bar. Figure 4.18(b) depicts the NIR-tail of the resulting supercontinua. The inset shows the cut-off wavelengths of the NIR-part of the spectra at the levels 10^{-4} of the normalized peak values. While increasing the pressure, we observe a nearly linear increase of the cut-off

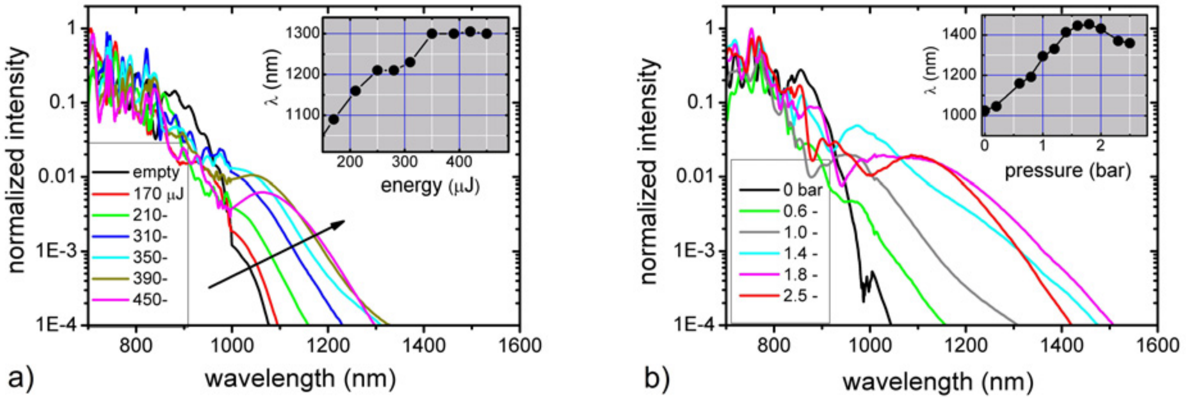

Figure 4.18: a) Dependence of the long wavelength part of the supercontinuum on the energy of sub-5 fs incident pulses at fixed Ar-pressure of 1 bar. b) Dependence of the long wavelength part of the supercontinuum on Ar- pressure for sub-5 fs pulses at fixed energy of 400 μJ. Insets show the cut-off wavelengths of the NIR-part of the spectra at the level 10^{-4} of the normalized peak values.

wavelength, which reaches a maximum, then decreases at even higher pressure. A maximum occurs at a pressure of 1.8 bar, around which the cut-off wavelength extends to ~1500 nm. This pressure dependence can be attributed to the fact that the nonlinear focus (z_c) shifts towards the focusing mirror with an increase in the gas pressure [128, 139] hence contributing more broadening due to the increase in the length of the filamentation, until it reaches an optimum and then declines again before reaching the threshold of multiple-filamentation.

In following we discuss an alternative scheme for spectral broadening using the HCF1 output after CMC.

4.3.5 Cascaded-HCF

As an alternative approach, we replaced the Ar-cell by a Ne-filled HCF2 of 1 m length with an inner diameter of 250 μm (Fig. 4.13(a)). In this case we used different focusing conditions than the filamentation in order to have efficient coupling into the HCF2. The focusing mirror FM$_2$ after the CMC was replaced by an $f = 1$ m planoconcave silver mirror. In addition the position of the FM$_1$ was slightly varied in order to have a divergent beam after the CMC. With theses changes we obtained a 1/e^2 beam diameter of 170 μm of the focus spot after FM$_1$. The HCF2 output was optimized for higher throughput as well as higher infrared broadening. Under optimum conditions an overall throughput of ~45% was obtained at a Ne pressure of 3.3 bar using ~5-fs 450-μJ incident pulses. At the output of HCF2, the high-energy supercontinuum (200 μJ) extends up to nearly three octaves (~250–1600 nm) as shown in Fig. 4.19(a). A simple

Fourier transform calculation shows that this broadband spectrum supports a pulse width of 1.3 fs centred at 550 nm. About 25% of the total energy is contained in the spectral range (700-1400 nm) required for seeding the main OPCPA chain in the PFS. Figure 4.19(b) depicts the output beam profile with 1/e^2 diameter of 4.5 mm at a distance of 0.5 m from the output end of the capillary of HCF2. The beam profile was measured using a WinCam-UCD12-1310 (RayOptics Inc.) device which has enhanced sensitivity in the NIR domain. A 3-mm thick Schott RG1000 bandpass filter which exhibits more than 5 orders of magnitude attenuation for a spectral range of 200–800 nm was used to suppress the intense spectral part of the supercontinumm below 800 nm for beam profile measurement. The depicted beam profile therefore corresponds to the infrared tail of the supercontinumm.

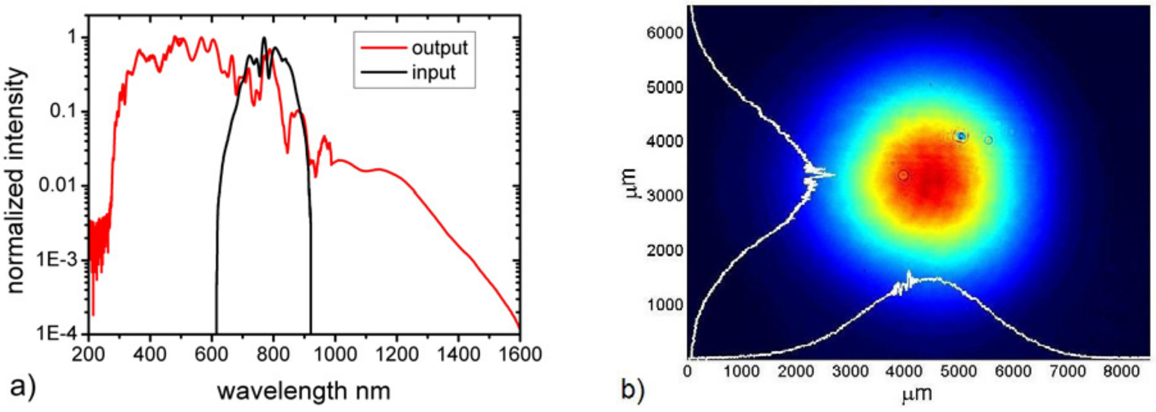

Figure 4.19: a) HCF2 input and output spectra. b) Beam profile of the NIR tail (above 800 nm) of the HCF2 output.

In the following the dependence of the NIR part of the supercontinuum after the HCF2 on the incident pulse energy and gas pressure is described. The day-to-day reproducibility of the NIR-tail is also presented.

Pulse-energy dependence

In this part of the experiment we used ∼5-fs pulses with different energies at fixed Ne-pressure of 3.3 bar in the HCF2. The input energy of the HCF2 is changed by two effects: i) by the iris (Fig. 4.13(b)), and ii) change of coupling efficiency of the fiber. The NIR-parts of the supercontinua are shown in Fig. 4.20(a). In the inset is depicted the cut-off wavelengths of this spectral domain. The energy dependence of the cut-off wavelengths levels off around 200 μJ input energy, indicating that no further spectral broadening towards the NIR domain occurs. The cut-off wavelengths increase with the pulse energy at fixed input pulse-width and Ne-pressure. It changes from 1000 nm to 1400 nm when the energy changes from 100 μJ to 300 μJ.

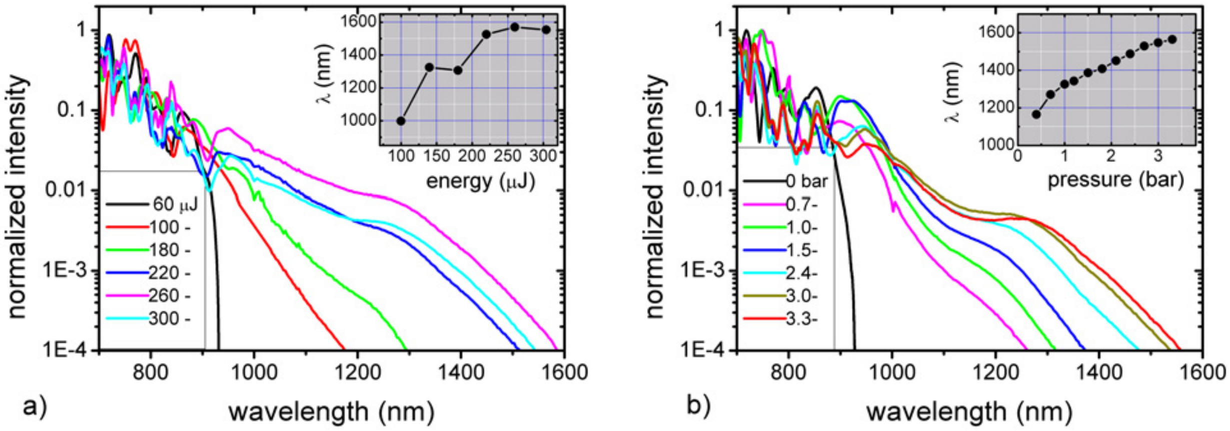

Figure 4.20: Dependence of the long-wavelength part of the supercontinuum after HCF2 on: a) energy of the incident pulses at fixed Ne-pressure of 3.3 bar; b) Ne- pressure at fixed energy of 310 μJ. The insets show the cut-off wavelengths of the NIR-part of the spectra at the level 10^{-4} of the normalized peak values.

Ne-pressure dependence

Here the ~5-fs pulses with a fixed energy of 310 μJ are used to study the effect of the gas pressure variation on the spectra at the output of HCF2. The Ne pressure was changed from nearly zero to 3.3 bar. Fig. 4.20(b) depicts the NIR-tail of the resulting supercontinua. In the inset is shown the cut-off wavelengths of the NIR-part of the spectra of the normalized peak values. While increasing the pressure to 3.3 bar we observe a nearly linear increase of the cut-off wavelength. At 3.3 bar of Ne the cut-off wavelength attains nearly 1600 nm. This might increase with further increase of pressure, however owing to the risk of damage of 0.5 mm thick entrance windows of the HCF2 this measurement was limited to 3.3 bar.

Reproducibility analysis of the HCF2 output spectrum

Shot-to-shot reproducibility:

In order to investigate the stability of the long-wavelength part of the supercontinuum after HCF2, we performed shot-to-shot spectrum measurements by synchronously triggering the spectrometer with the HCF input pulses. The output beam after the HCF2 was confined to the central spot by an iris and coupled into the spectrometer. A 1-mm thick RG-850 (SCHOTT) colour long-pass filter was used to suppress the high spectral peak below 800 nm. The spectra of 200 successive pulses were recorded. The spectrum shown in red in Fig. 4.21(a) represents the mean ($\bar{X}(\lambda)$), while the green curves depict the standard deviation ($\sigma(\lambda)$) of the measured spectra. The blue curve presents the percentage fluctuations $\left(\frac{\sigma(\lambda)}{\bar{X}(\lambda)} \times 100\right)$ of the intensities of different spectral components. We observe less than 1% of fluctuations of the intensity of the spectral components for the whole spectral range of 700-1400 nm, which indicates that the spectrum does not change significantly from one shot to the other.

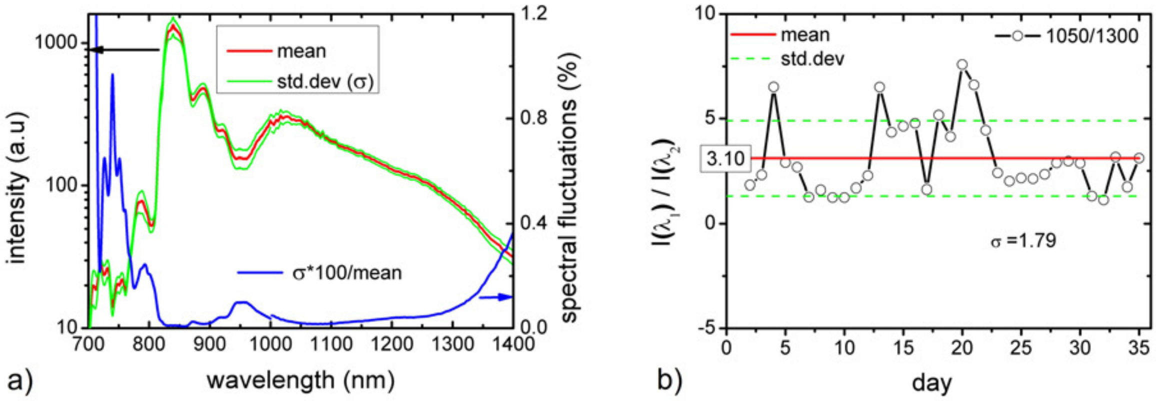

Figure 4.21: (a) Shot-to-shot and (b) day-to-day reproducibility of the NIR-tail of the HCF2 output spectrum (see text for explanation).

Day-to-day reproducibility:

The analysis is based on the HCF2-output spectra recorded for more than 30 days. In each of these days the HCF2 was aligned with an overall throughput of 45±5%. It can be seen from Figs. 4.20(a,b), as the NIR tail of the supercontinuum shifts to higher wavelengths a plateau appears in a range of 1050–1300 nm. Our day-by-day experience of alignment revealed that this feature is well reproducible. The flatter the plateau, the better was the thoughput and the NIR tail of supercontinuum. For every day alignment we specified the slope of this plateau, i.e. the ratio of the spectral intensities $(I(\lambda_1)/I(\lambda_2))$, to be less than 10 for $\lambda_1 = 1050$ nm and $\lambda_2 = 1300$ nm. This slope is adjustable by the energy of the input pulse, fine alignment of the HCF2, and gas pressure. Moreover fine-tuning of the wedges before the CMC (see Fig. 4.13(a)) or changing the GDD of the DAZZLER by ± 100 fs^2, which mainly affects the temporal width of the incident pulses, also helps to adjust the slope of the plateau. From the recorded spectra of more than 30 days we calculate the mean value of these ratios as 3.1 with a standard deviation $\sigma = \pm 1.79$ as shown in Fig. 4.21(b), which is an indication of well reproducible NIR tail of the supercontinuum.

4.4 Comparison of different OPCPA seed generation methods

Figure 4.22 shows that the comparison between the infrared parts of the spectra obtained by the NOPA-idler (Sec. 4.2.2), HCF-filamentation (Sec. 4.3.4), and cascaded-HCF (4.3.5) schemes.

The presented spectra have been normalized to their respective spectral energies in the range of 700–1600 nm. As shown, the spectrum of the NOPA generated idler, from our preliminary experimental setup, is more than 1 orders of magnitude weaker above 1200 nm (green curve) compared to that obtained from the HCF-filament or cascaded-HCF. Although the idler can have significantly better spectrum as predicted by the calculations, its angular chirp compensation is still very complicated requiring a special grating, telescope as well as a deformable mirror to reduce the residual angular difference to the sub-μrad range for a broadband spectrum of 700–1400 nm. The HCF-filament technique, on the other hand, is attractive due to the ease of alignment and its rather simple construction. However, it requires careful control of the gas pressure, input pulse energy and beam profile. Here, maximum broadening is obtained near the threshold of multiple-filamentation (Sec. 4.3.4). Operating well-below the threshold of multiple-filamentation can result in stable operation but in this case the NIR-part of the output spectrum will be weaker compared to that of the cascaded-HCF scheme (see Figs. 4.18 and 4.20 for comparison). Moreover our experience on the filamentation while operating near the threshold reveal that the day-to-day reproducibility of the NIR-tail is very poor, with the ratio $I(1050)/I(1300)$ changing by nearly 2 orders of magnitude with similar input parameters, owing to its relatively high sensitively on spatial beam-profile of incident pulses. Comparison of the optimized spectra

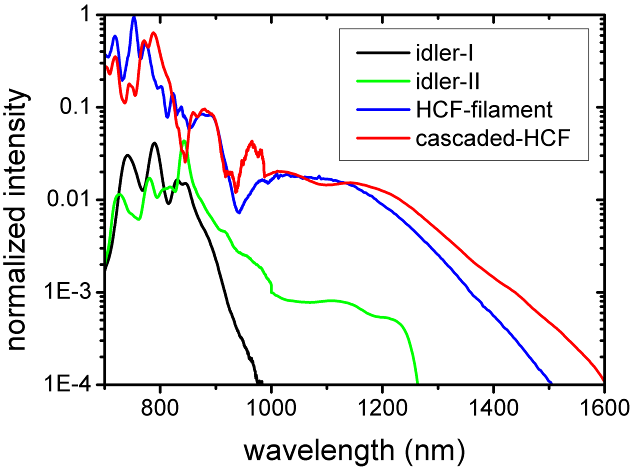

Figure 4.22: Comparison between the infrared spectral parts of the NOPA-idler (Fig. 4.9(b), 4.10), HCF-filament (Fig. 4.17), and cascaded-HCF (Fig. 4.19) outputs. idler-I: the case when the seed pulse for the NOPA was generated using Ar-filament, and idler-II: idler spectrum when the Ar-filament cell was replaced with an Ar-filled HCF. The spectra are normalized to their respective output energy of 3 μJ, ~3 μJ, 55 μJ, and 50 μJ in the 700–1600-nm spectral ranges. For idler-II we assume a value of 3 μJ keeping in view similar losses through the compensator as that of idler-I.

of the two schemes shows that the slope of the HCF-filament output spectrum, between 1050-1300 nm, is $\approx$3 times more steep than that from HCF2 (Fig. 4.22). The cascaded-HCF scheme exhibits reproducible spectra both on shot-to-shot as well as day-to-day basis as discussed in Sec. 4.3.5. It is also more attractive due to its higher output energy. This high stability of the HCF2 generated supercontinuum compared to the filamentation can be attributed to the fact that the former has a fixed nonlinear interaction length defined by its HCF while for the latter it depends on operating conditions, such as input energy, beam profile, pulse width etc. These features make cascaded-HCF scheme better suited for OPCPA amplification in the NIR. Therefore we adapted this scheme for seeding the OPCPA chain in PFS. Since the laser beam path between the two HCF's is very short (i.e. $\sim$2 m) and that this path is enclosed in a housing, it does not introduce any prominent thermal drift and beam pointing fluctuations at the entrance of HCF2. Therefore no additional beam pointing stabilization is needed before HCF2. The reproducible shot-to-shot spectrum of the HCF2 also supports this claim.

4.5 OPCPA seed stretcher

In order to make the OPCPA process efficient, the seed pulse should have approximately the same pulse duration as that of the pump pulse [2]. The exact ratio of the pulse widths however depends upon the relative timing jitter between these pulses as well as their temporal characteristics. In case of spectral broadening by an HCF or optical filamentation the pulse duration of the broadband supercontinuum is generally considered to be of the order of the width of input pulse [133, 134], i.e. 5–10 fs for our case. Therefore in order to match with the 1-2 ps pulse duration of the pump, the OPCPA seed has to be temporally stretched. As discussed in Chapter 1, the design of the PFS requires the seed pulses to be stretched in a way that it can be finally compressed by bulk material to ensure high throughput of the setup [2]. In this scheme the beam diameter of the amplified beam has to be adjusted such that the B-integral and hence the nonlinear effects such as SPM can be can be kept low (cf. Eqs. 3.19, 4.24). The stretching of the OPCPA seed pulse is thus done in a double-prism pair stretcher (Fig. 4.13(a)) which provides negative GDD. The design calculations for the stretcher follows the equations from Sec. 3.1.2. Since the higher order dispersion of the stretcher is different from that of the bulk material (cf. Sec. 3.1.2), we need broadband chirped mirrors (BBCM) to compensate the residual dispersion. In these calculations we analyse different commercially available materials for the prisms in our stretcher, in order to select a material which provides the most linear GD curve, in the presented materials, and therefore the smallest higher order dispersion (e.g. TOD). In this way, a minimum number of reflections will be required for compensating the residual higher-order dispersion of the compressor. Figure 4.23 presents the comparison of the calculated GD and TOD for the BK7,

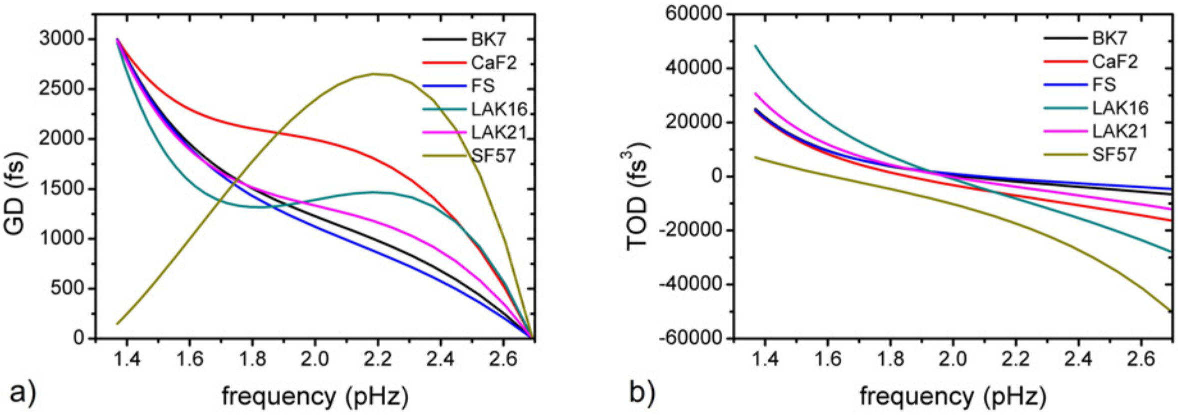

Figure 4.23: a) The GD, and b) the TOD introduced by the stretcher for different prism materials (like BK7, CaF_2, FS, LAK16, LAK21, and SF57 with L= 35, 340, 40, 30, 28, and 0.2 cm respectively) as a function of frequency $(\omega = 2\pi c/\lambda)$.

CaF_2, FS, LAK16, LAK21, and SF57 prisms. The separations L between the prism pairs was adjusted in a way to introduce nearly the same GD (Eq. 3.16) between 700–1400 nm. The prism dimensions used in these calculations were the same as for Sec. 3.1.2. As it is evident that the FS prisms exhibit a comparatively more linear GD curve and less high-order group-velocity dispersion (e.g. TOD) than other materials, we therefore choose FS prisms for setting up the OPCPA seed stretcher. We further performed the calculations for GD introduced by the FS prism pair stretcher at different values of L. These results are shown in Fig. 4.24. The prism separation L of 10, 20, and 40 cm results in a GD of 1, 1.75, and 3 ps, respectively between 700–1400 nm.

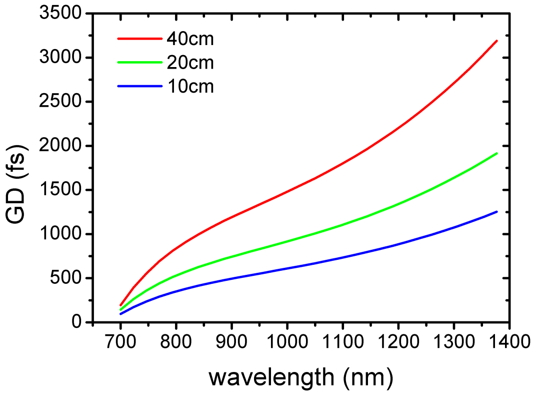

Figure 4.24: Calculated GD of the FS double-prism pair for L= 40 cm (red), 20 cm (green), 10 cm (blue).

4.5.1 Characterization of the stretched seed-pulses

In order to compare the results of our simulations with the experiment the prism separation was set at 40 cm. The desired part of the spectrum in the range of 700–1400 nm was separated from the supercontinuum by clipping the dispersed spectrum on the second prism pair (Fig. 4.13(a)) at a wavelength of 680 nm. This technique seems to be a convenient way of precisely controlling the amount of dispersion for our broad spectral range on a day-to-day basis. The position of the resulting spectral clip is easily monitored and is a good indication for the amount of inserted prism material. Similarly, the first prism of the stretcher is adjusted so that the input beam will just pass through its apex without being clipped. The output spectrum of the stretcher is presented in Fig. 4.25(a).

The stretched pulses are characterized by a modified frequency-domain phase measurement (FDPM) scheme [145] by measuring their cross-correlation with a fraction of the Femtopower output (60 μJ, 25 fs) as the reference. The principle of this technique is explained in Fig. 4.25(b). In case of a stretched pulse, the spectral slices, cut out from its whole spectrum, at different

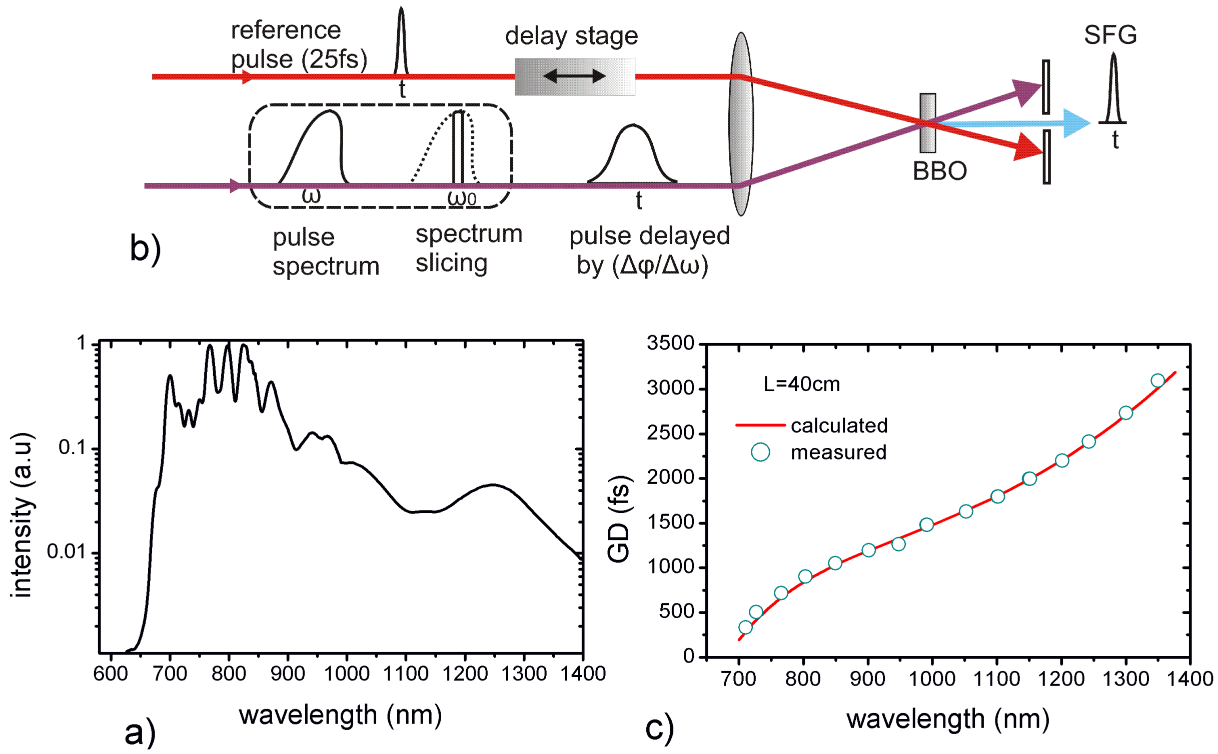

Figure 4.25: (a) OPCPA stretcher output spectrum. (b) Schematic of modified frequency-domain phase measurement. (c) Measured GD (small circles) using modified FDPM scheme for an apex-apex separation (L) of 40 cm. Calculated GD of the FS double-prism pair for L= 40 cm (red curve).

central wavelengths ($\lambda_0 = 2\pi c/\omega_0$) exhibit different group-delay $(\Delta\varphi/\Delta\omega)|_{\omega_0}$ with respect to the reference pulse. The relative delay of the peaks of the sum-frequency-generation (SFG) signals, obtained through the cross-correlation of these spectral slices with the reference pulse, provide a direct measure of the frequency-resolved GD.

In order to retrieve this frequency-dependent GD information, we performed successive measurements with narrowband spectral slices with $\sim$10 nm FWHM. This high spectral resolution was achieved by inserting a slit, at the focus position of the lens L_2, in the spectrally dispersed beam after the prism (P_4) as shown in Fig. 4.13(a). The central wavelength of these spectra was tuned by changing the horizontal position of the slit. We monitored the peak positions of the SFG signal corresponding to the narrowband spectra with varying central wavelengths with respect to the reference pulse in a 10 μm thick BBO crystal. The crystal was aligned for best phase matching at 1000 nm, and was sufficiently thin to observe the SFG for the whole spectral range without realignment. The results of the GD measurements by FDPM are shown in Fig. 4.25(c). It provided a very nice agreement between the measured and calculated GD for L= 40 cm and allows for calculating the GD of prism stretcher for any arbitrary value of L.

4.5.2 Scheme of final compression

The seed pulses in the OPCPA chain of PFS will maintain a total GD of 1.0–1.5 ps between 700–1400 nm. The exact dispersion, however, depends upon the temporal characteristics of the pump laser system which is under-development and will be specified in the future. In order to present a scheme for final OPCPA pulse compression, we assume a total GD of 1.5 ps for the entire spectral range of the seed pulse. The design dispersion of the OPCPA stretcher, broadband OPCPA seed and compressor is presented in Fig. 4.26. We choose CaF_2 as an optical material for the compressor because of its significantly smaller nonlinear refractive index ($n_2 = 1.42 \times 10^{-20}$ m^2/W [146]) compared to that of other commercially available glasses, e.g. SF57 [147], BK7 [148], fused silica [149] etc., to reduce the risk of SPM (Eq. 4.24) at J-scale OPCPA amplified pulse. It is commercially available in high laser grade quality. The CaF_2 provides a GD of 30 fs per mm for the whole spectral range of the OPCPA seed pulse. The target dispersion for the seed pulses can therefore be equivalent to the dispersion introduced by 50 mm of CaF_2 with opposite sign as shown in red (Fig. 4.26). The calculated dispersion of the prism stretcher is shown in green in the same figure, whereas the difference of these curves (shown in blue) will be compensated by the BBCM before amplification. In addition to the BBCM, a deformable mirror can be used in the spectrally dispersed beam after P_4 (Fig. 4.13(a)) in the prism stretcher for fine-tuning of the pulse dispersion [150]. Moreover owing to a very broadband spectrum of the seed pulses we cannot ignore the dispersion introduced by the OPA crystals (such as DKDP) and air. Knowing the length of the crystals and air propagation distance it can easily be implemented in the target dispersion of the BBCM. Our plan is to include the dispersion of such

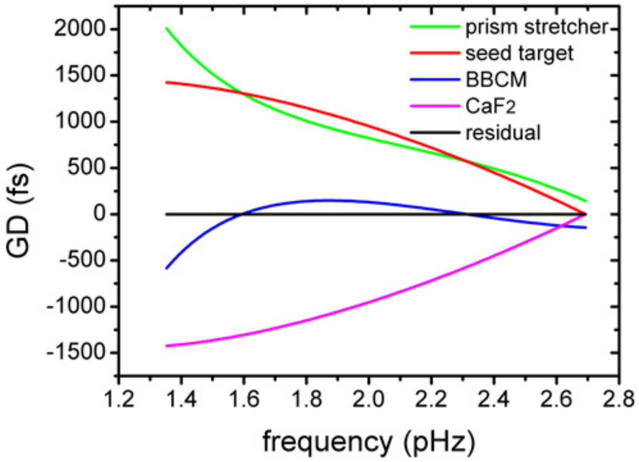

Figure 4.26: Scheme for dispersion management of the OPCPA seed: The green curve denotes the GD as a function of frequency $(\omega = 2\pi c/\lambda)$ introduced by the prism stretcher for L=20 cm. Target dispersion of the broadband chirp mirrors (BBCM) is shown in blue. The GD of the OPCPA seed for amplification is presented in red. After amplification this will be compressed with 50 mm of CaF_2 whose total dispersion is shown in pink. The residual dispersion after compressor in shown in black.

elements from the first OPCPA stage in the target design of the BBCM (This will slightly change the target dispersion of the BBCM compared to what is presented in Fig. 4.26). Moreover, the dispersion introduced by the crystal material and air propagation in the next OPCPA stages will be adjusted separately with another set of chirped mirrors.

4.6 Summary

In summary we have studied three schemes for broadband OPCPA seed generation: NOPA-idler, HCF-filament, and cascaded-HCF. In the case of the NOPA, we have proposed an improved scheme for compensating the inherent angular chirp of the idler pulse based on the combination of a telescope and a diffraction grating. By optimizing the magnification factor of the telescope and by choosing the appropriate grating constant, our analysis showed that the residual angular dispersion of the idler can be reduced to a value at least one order of magnitude below that achieved to date [63]. For few-cycle pulses it is crucial to minimize the residual angular chirp, since it can lead to a significant temporal broadening and therefore a reduced intensity in the focus of the pulse. For the remaining higher-order terms of the angular dispersion we propose to apply a deformable mirror in the compensator setup. In our experiments we have demonstrated that the NOPA pumped at the second harmonic of a Ti:sapphire source and seeded by the spectrally broadened output of a filament is capable of generating an idler beam in the desired wavelength range of 700–1400 nm. Our preliminary measurements resulted in a output of $\sim$3 μJ after the angular chirp compensator. The setup and the amplification process can still be optimized for a more uniform spectral intensity distribution across this large spectral range.

The other schemes for OPCPA seed generation discussed in this chapter relied on production of a broadband supercontinuum using few-cycle pulses. The theoretical investigation for the source of required broadening into the infrared for sub-two cycle pulses showed that this effect first develops in a classical SPM broadening stage, followed by a second enhancement induced by a sharp leading edges of the pulse front. Initiated by plasma defocusing and strong dispersion, this two-peaked profile preserves a focused front over a long distance, which is associated with the largest redshift in the spectrum. Furthermore, our calculation predict that the phase of the broadband supercontinuum pulse is a single-valued function of angular frequency. Therefore it is expected to be compressible close to the transform-limit, and it can be potentially employed for seeding the OPCPA chain.

In experiment, in the first part of this cascaded spectral broadening scheme we have shown pulse compression down to the sub-5 fs regime. It has been achieved by spectral broadening of the Ti:sapphire amplifier output in a Ne-filled hollow core fiber followed by its recompression using double-angle dispersive mirrors which were developed by Pervak et al. [140]. The inherent phase oscillations of the chirped/dispersive mirrors, which may adversely affect the pulse quality in the few-cycle regime and that usually require a matched pair of CM's for compression, can be compensated by using the same mirrors at two different angles of incidence. In this way the unwanted phase-oscillations can be reduced by more than two orders of magnitude from their original value [140]. Using these mirrors, the compression of $\sim$0.5 mJ pulses down to nearly transform limited FWHM duration of 4.3 fs was demonstrated. Subsequently, by using these few-cycle pulses broadband supercontinua spanning up to nearly three octaves were obtained by exploiting self-phase modulation via filamentation in argon (HCF-filament) as well as a second hollow core fiber (cascaded-HCF). Under optimum conditions the former showed a broadening into the infrared by $\sim$500 nm, i.e. from nearly 1000 nm to $\sim$1500 nm, while the latter $\sim$700 nm (900 nm to 1600 nm). The output energy of the broadband supercontinua after the HCF-filament and cascaded-HCF was measured to 100 μJ and 200 μJ, respectively. The infrared tails of both spectra contained nearly 50 μJ of the energy between 700–1400 nm. Our day-to-day monitoring of cascaded-HCF output supercontinuum for more than 30 days showed that its infrared tail is well reproducible. This feature is attributed to the fixed interaction length in the cascaded-HCF, making it more robust compared to filamentation.

By comparing the spectra, output energy, beam profile, and robustness we prefer the cascaded-HCF scheme over NOPA-idler and HCF-filamentation for seeding the OPCPA chain of the PFS.

The main challenge for the cascaded-HCF scheme which we can foresee is its strongly modulated spectrum. A complete characterization of the spectral phase of the seed pulses is yet to be done, which will possible after first amplification stage. In case of some strong modulation of spectral phase in connection with the amplitude modulation, the idler generation scheme, where the initial amplitude modulations are much less, can be considered as a back up solution. In addition to the OPCPA seed generation we have also described a scheme for pulse stretching and compression for the OPCPA chain of the PFS. Here the broadband seed is stretched using a fused-silica double-prism pair stretcher. The amplified pulses will therefore be amplified with negative chirp and recompressed using bulk material. For compensation of the residual higher order dispersion between the prism-pair stretcher and bulk material, we suggest to use broadband chirped mirrors in the stretcher.

Chapter 5

Broadband OPCPA using DKDP and level of temporal synchronization between pump and seed pulses

As discussed in Chapter 1, the PFS system is based on short-pulse pumped OPCPA technique in which high power ps-scale pump pulses are used to amplify a broadband seed in thin OPA crystals. The numerical calculations of Major et al. [2] for the design parameters of the PFS system show a broadband gain in DKDP that supports few-cycle pulse duration when pumped with 1-2 ps pulses with central wavelength of 515 nm in a non-collinear pump-seed geometry (NOPA). These calculations predict multi-Joule level amplification of few-μJ-energy 700–1400-nm spectral-range seed pulses in a total of 7-8 OPCPA stages using few-mm thick DKDP crystals and a pump energy of 15-20 J [2, 111]. In the previous chapters the schemes for generating the optically synchronized seed pulses for the pump laser and broadband OPCPA chain were discussed. Therefore we can now start with the OPA experiment, however the temporal synchronization between the pump and seed pulses have to be checked which is an important issue of OPA to deal with. In this chapter we present the first experimental demonstration of a broadband amplification in DKDP. Moreover, a detailed investigation of the level of timing synchronization between the pump and seed pulses is also described.

Firstly, the experimental setup used for the pump-seed synchronization and parametric amplification measurements is presented. This is followed by the investigation of timing jitter between the pump and seed pulses at the position of first OPCPA stage of the PFS system. Finally, the details of the experiment of few-ps pumped OPCPA are presented.

5.1 Experimental setup

The parametric amplification and the timing jitter measurements were carried out using the available PFS frontend, first amplifier stages of the pump laser chain and broadband seed generation discussed in Chapters 2 and 4, respectively. The schematic layout of the setup is shown in Fig. 5.1. The current configuration of the Yb:YAG CPA pump laser delivers 1-2 ps ∼200 mJ pulses with a FWHM bandwidth of ∼3.5 nm at a central wavelength of 1030 nm. The output is subsequently frequency doubled using DKDP crystal for the pumping the first OPCPA stage at 515 nm. The broadband OPCPA seed pulse, on the other hand, is generated by cascaded spectral broadening technique using the output of the Femtopower system. It is then temporally stretched to match with the pulse duration of the pump laser. The pump laser is combined with the broadband seed pulse in the DKDP OPA crystal in the non-collinear geometry to allow for the broadest bandwidth and to aid the separation of the beams after amplification.

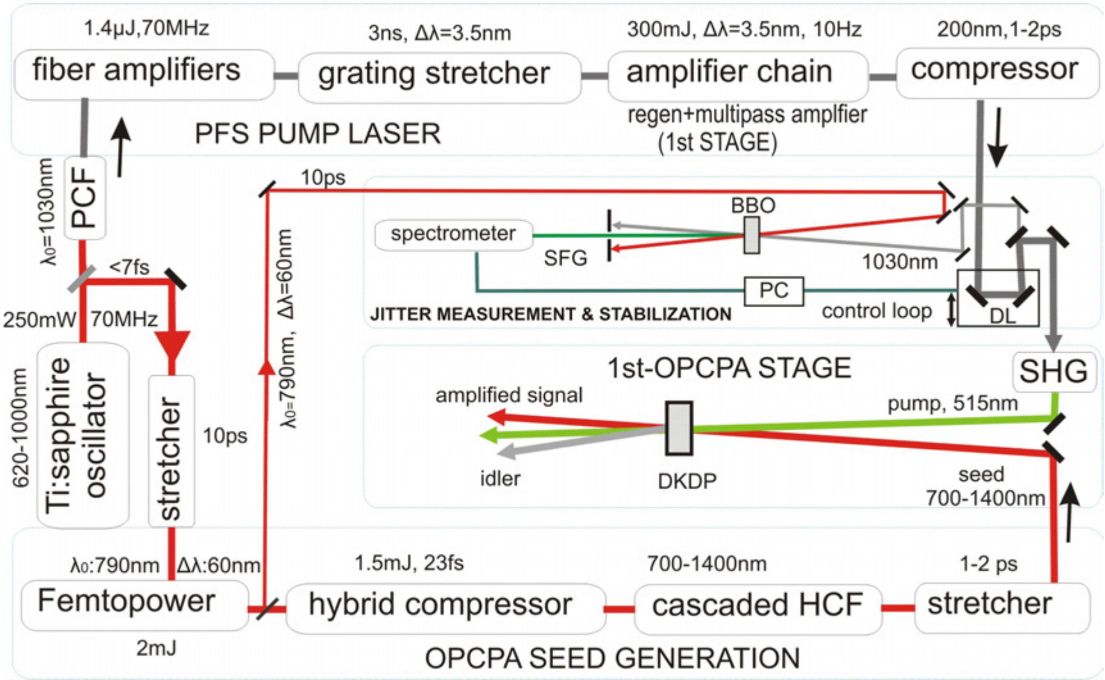
1.4μJ,70MHz
fiber amplifiers
3ns, Δλ=3.5nm
grating stretcher
300mJ, Δλ=3.5nm, 10Hz
amplifier chain
regen+multipass amplfier
(1st STAGE)
200nm,1-2ps
compressor
PFS PUMP LASER
λ0=1030nm
PCF
<7fs
250mW
70MHz
620-1000nm
Ti:sapphire oscillator
stretcher
10ps
10ps
λ0=790nm, Δλ=60nm
spectrometer
SFG
BBO
1030nm
PC
control loop
DL
JITTER MEASUREMENT & STABILIZATION
SHG
1st-OPCPA STAGE
amplified signal
idler
DKDP
pump, 515nm
seed
700-1400nm
λ0:790nm
Δλ:60nm
Femtopower
2mJ
1.5mJ, 23fs
hybrid compressor
700-1400nm
cascaded HCF
1-2 ps
stretcher
OPCPA SEED GENERATION

Figure 5.1: Experimental setup: The current configuration of the pump laser contains two subsequent Yb-doped fiber amplifiers, a grating stretcher, an Yb:glass regenereative amplifier (regen), an Yb:YAG booster amplifier in multipass geometry, and a grating compressor (cf. [72]). The broadband OPCPA seed generation setup contains a Ti:sapphire multipass laser- amplifier (Femtopower), a subsequent hybrid pulse compressor, Ne-filled cascaded hallow core fibers (HCF's), and a prism-pair stretcher (cf. Secs. 4.3.5, 4.5). PCF: photonic crystal fiber; λ_0: central wavelength of the spectrum; $\Delta\lambda$: FWHM of intensity profile; SFG: sum-frequency generation signal; PC: computer; SHG: second harmonic generation; DL: delay line.

For timing jitter measurements, we used the compressed pump pulse at its fundamental frequency (i.e. at 1030 nm) and the stretched amplified pulse after the Femtopower as shown in Fig. 5.1. The details of these measurements are described in the following section.

5.2 Level of synchronization between the OPCPA pump and seed pulses

The technique of few-ps OPCPA demands a very accurate and stable synchronization between the pump and seed signals owing to a very small timing window, i.e. of the order of few-ps, for amplification. A timing jitter of several-100 fs can result in a significant change of the amplified spectrum and hence variation in the compressed-pulse duration from shot-to-shot. Although the pump and OPCPA-seed signals are optically synchronized in our setup, the former has to pass through the entire CPA-pump chain before the parametric amplification of the broadband seed pulses can take place, see Fig. 5.1. This long path through the pump-laser chain results in $>1\mu$s of total optical delay between the OPCPA pump and the seed at the position of the first OPCPA stage for our present setup (Fig. 5.1). To overcome this delay, different pulses from the "master oscillator" of the common frontend are selected for the pump and the seed chains before being combined in the OPCPA stage. In this scheme the sources of possible timing fluctuations between the two pulses can be the finite stability of the master oscillator's repetition rate, temperature drifts, air turbulences and mechanical vibrations of optical components over this rather long optical path of the pump pulse. We therefore performed systematic measurements to quantify the contributions of these effects on the timing synchronization between the pump laser and OPCPA seed pulses. The results of these measurements are detailed in the following subsection.

5.2.1 Timing jitter measurements

In order to quantify the level of synchronization in the above described setup we performed single-shot measurements of the relative timing between the pump and the OPCPA seed pulses.* For this purpose we used the so-called spectral gating technique [151] schematically shown in Fig. 5.2. Here a sum frequency (SFG) signal is generated by the spatio-temporal overlap of a short, and a nearly linearly chirped, long pulse in a nonlinear crystal. The generated signal is monitored using a high resolution spectrometer. For a temporally chirped pulse different spectral components are delayed in time with respect to each other, constituting wavelength (or

---

The described work of timing jitter measurements was equally contributed by S. Klingebiel, MPQ, Hans-Kopfermann Str.1, 85748, Garching, Germany

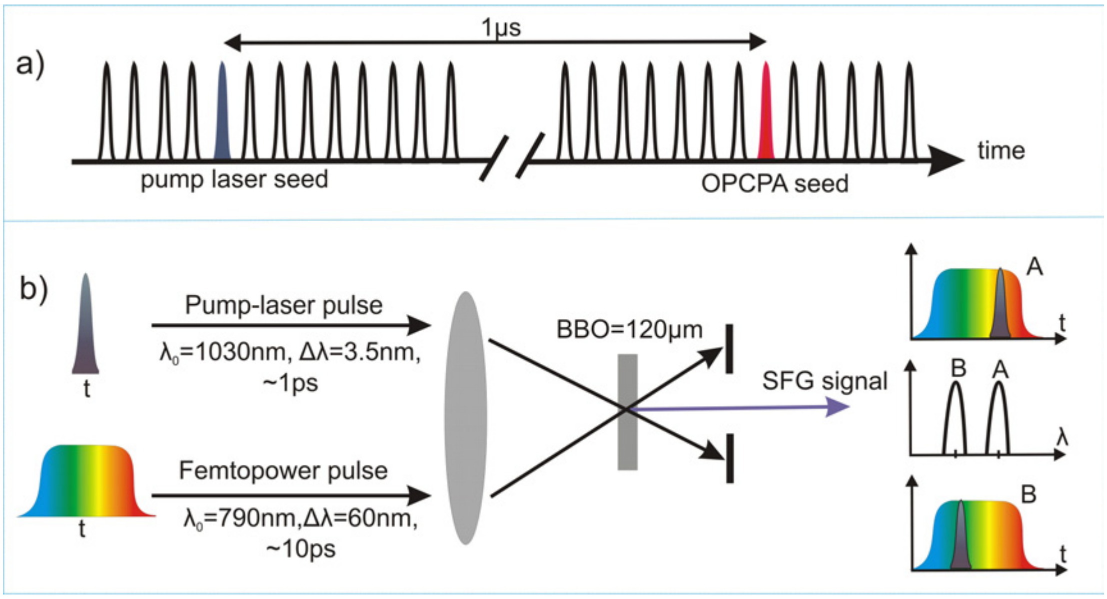

Figure 5.2: a) Scheme of temporal synchronization between the pump and seed pulses at the first OPCPA stage: different pulses are selected from the master oscillator output for seeding the pump laser chain and the OPCPA chain in order to compensate the longer optical delay of the former. b) Schematic picture of the spectral gating technique [151]: A and B indicate the temporal position of the short and long pulses in BBO, for two different shots from the laser sources, in case of imperfect synchronization. The short pulse overlaps with different spectral components of the long pulse which is chirped linearly, causing a shift in the SFG spectrum as depicted.

frequency) dependent group delay (Fig. 3.2(b)). Therefore, a drift in the temporal positions of two pulses from one shot to another results in a change in the overlap between spectral components of the short and long pulses in the nonlinear medium, hence inducing a shift in the SFG spectrum. A perfect temporal synchronization, on the other hand, does not exhibit such change. The timing fluctuations in this way are transformed to the frequency domain and the relative time delay can be derived from the shift of the peaks of corresponding spectra.

We used the compressed ∼1 ps pump pulse before it was frequency doubled, i.e. at 1030 nm (cf. Fig. 5.1). Our reference pulse was split off from the common frontend before compression and spectral broadening. It, therefore, had a pulse duration of >10 ps and a FWHM spectral bandwidth of ∼60 nm (Fig. 3.2). We can safely assume that the additional compression and broadband seed generation does not introduce significant additional timing instabilities, since the optical path difference is negligible compared to that of the pump pulse. This scheme is insensitive to pointing fluctuations (for spatial-chirp free pulses) and shot-to-shot energy changes of the test pulses. The resolution of the technique in our case is ∼10 fs, which is given by the spectrometer resolution (0.15 nm for Avantes AvaSpec 2048) in combination with the accuracy of the determination of the peak position of our spectral distribution.

5.2.2 Results and discussion

Our findings are summarized in Fig. 5.3. The fluctuations of the relative timing between pump and seed for the entire CPA chain are shown in Fig. 5.3(a). Here the pump beam is stretched, fully amplified in the regenerative amplifier (regen) and the multipass amplifier and subsequently compressed. For this measurement no precautions were taken to reduce air fluctuations within the boxes covering the entire system, especially the compressor. The timing jitter in this case was measured to be ±400 fs, which is clearly unacceptable for proceeding with the short-pulse pumped OPCPA experiments. Fig. 5.3(b) depicts the results of synchronization measurements for the same pass through the amplification chain after the installation of beam tubes in the compressor and construction of housings around all the components of the CPA chain. This improvement helped in reducing the air turbulences along the long propagation distances of the beam. From our measurement over $\sim$5 minutes, we can clearly see that there are two separate components to the remaining timing jitter: a shot-to-shot variation of about ±70 fs superimposed on a slow temporal drift of ±200 fs. The Fourier transformation of this jitter measurement reveals the frequency at which the slow temporal variation takes place as <0.1 Hz (Fig. 5.3(c)).

In order to quantify the contribution of different components of the CPA pump-laser chain to the measured timing jitter, we studied the impact of the long delay in the regen. We amplified the unstretched pulses in the regen to a low power level. The relative timing was then measured between the reference pulse and the pulses amplified in the regen in the case when i) the same pulses, and ii) different pulses with $> 1\mu$s delay were selected from the master oscillator for both chains. The timing jitter in these cases was measured to be ±14 fs and ±33 fs respectively (Fig.5.3(d)). This corresponds to the resolution limit of our measurement setup, but is clearly well below our needs for the short-pulse pumped OPCPA. Based on these measurements it can be concluded that the main contribution to the fluctuations of relative timing of pump pulses arises from the stretcher and/or compressor.

An active stabilization system was installed in order to correct the long term timing drifts. The results of temporal synchronization after this improvement are presented in the following.

5.2.3 Active stabilization of timing jitter

We used our home-built active stabilization system at the nominal repetition rate of 10 Hz of the pump laser for the correction of slow drift in the relative timing shown in Fig. 5.3(b). This system performs online monitoring of the relative timings between the pump and seed pulse, at the position of first OPCPA stage of PFS, using the principle shown in Fig. 5.3. An active motorized-

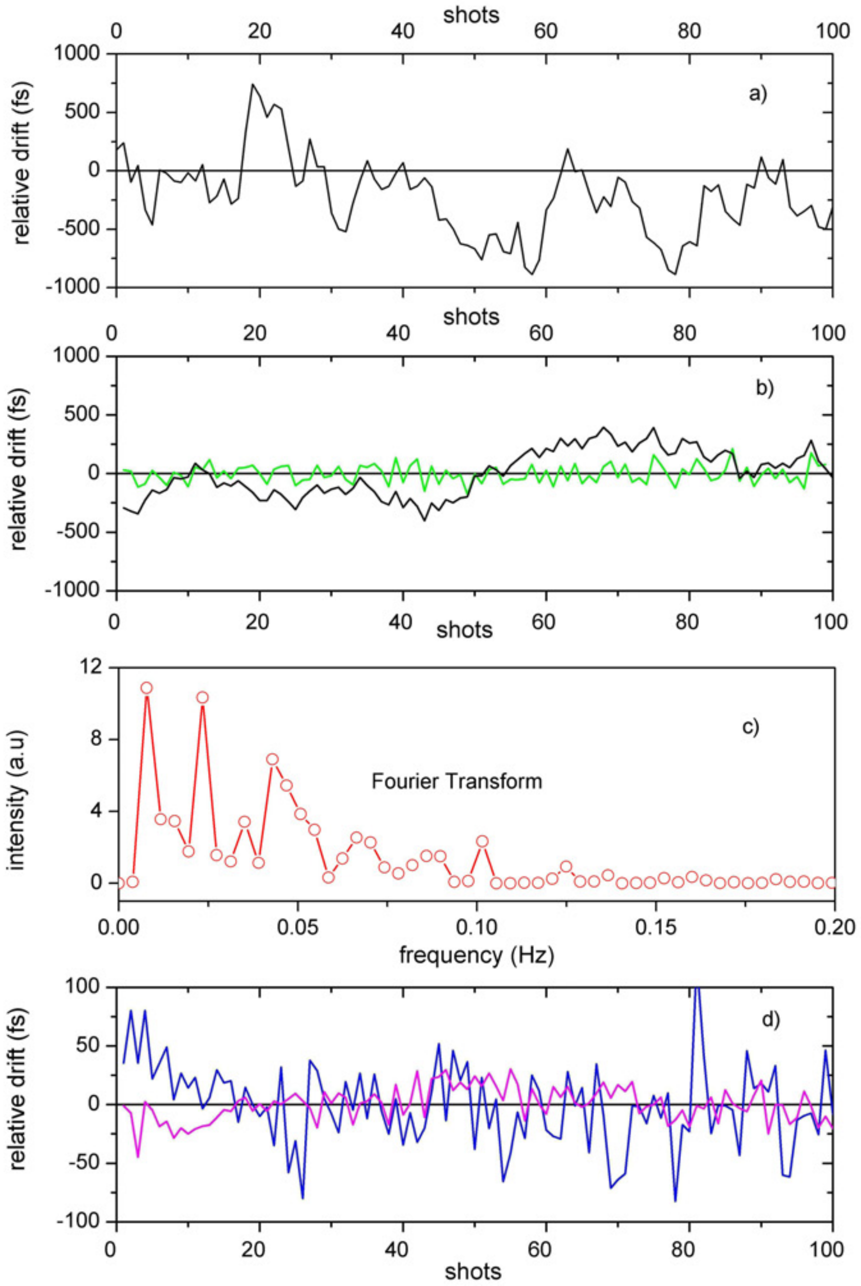

Figure 5.3: Timing jitter measurements: a) Pump pulse passes through entire CPA chain. b) Pump pulse passes through the entire CPA chain with beam tubes in the compressor (black curve); shot-to-shot fluctuations (green) extracted from black curve. c) Fourier transform of black curve in b). d) Timing jitter between the Femtopower and regen amplified-pulses by selecting i) same pulses (pink), and ii) different pulses with 1 μs delay (blue) from the master oscillator. See text for more details.

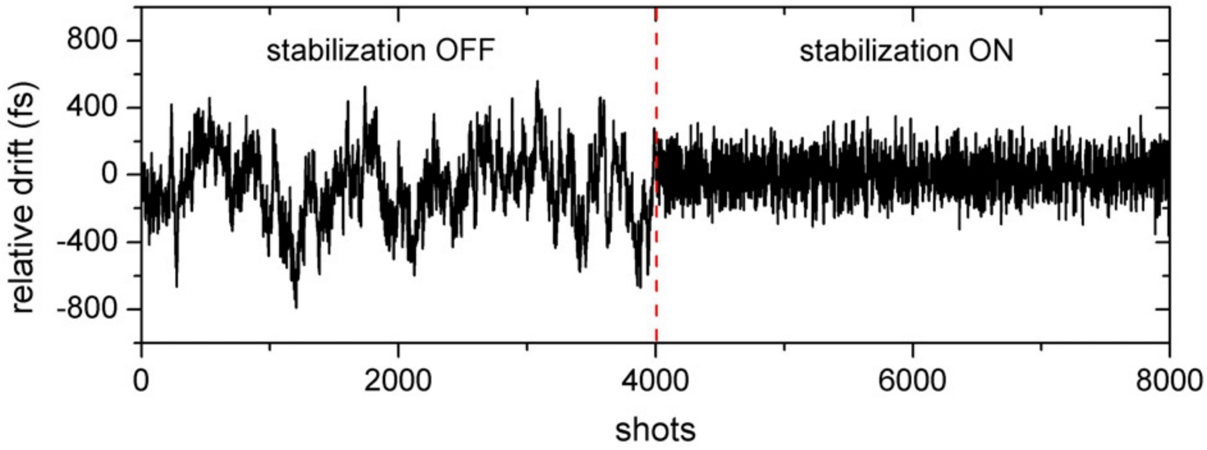

Figure 5.4: Active stabilization of relative timing fluctuations at the position of first OPCPA stage.

delay stage, installed in the optical path of the pump laser, is moved accordingly to correct the timing between the two pulses. This system at present works at less than 10 Hz repetition rate, the measured timing jitter is therefore the average of a number of pulses. Nevertheless this modification has reduced the timing jitter to ±100 fs (Fig. 5.4) which allows to perform the short-pulsed pumped OPCPA (for detailed description see [152]).

As a further investigation of the possible sources of timing jitter in the stretcher-compressor setup, we analysed the effect of beam pointing fluctuations at the input of the stretcher/compressor. Here we performed the beam pointing measurements at the input of the stretcher and compressor. A simple formulation was developed to calculate the equivalent timing jitter due to these fluctuations. The details of this analysis are presented in the following section.

5.2.4 Timing jitter due to the change in beam pointing at the input of the compressor

As discussed in Chapter 2, the design of the compressor for the CPA pump laser is based on a Treacy-type parallel grating pair [45]. Figure 5.5 shows the geometrical arrangement of this compressor for a design angle of incidence (AOI) of α_0 and a grating separation of L_1 along the central wavelength component λ_0, as reproduced from Fig. 2.2. Here for illustration only the λ_0 is considered, however the following discussion is also true for all other wavelengths. The optical path of a ray of wavelength λ_0 for the design AOI of α_0 is shown in red. The ray is diffracted in the first order from the first grating (grating1) at an angle β_0 given by

$$\beta_0 = \arcsin\left(N\lambda_0 - \sin\alpha_0\right), \tag{5.1}$$

where N is the line density of the grating (recalling Eq. 2.3). It impinges on the second grating (grating2) at an angle β_0 and is diffracted at an angle α_0, as calculated from the Eq. 5.1, given that N is same for both gratings. The λ_0 ray subsequently approaches the end mirror at normal incidence, which redirects it back to its original path in order to fold the optical path. The ray travels equal distances in the first and second pass through the compressor.

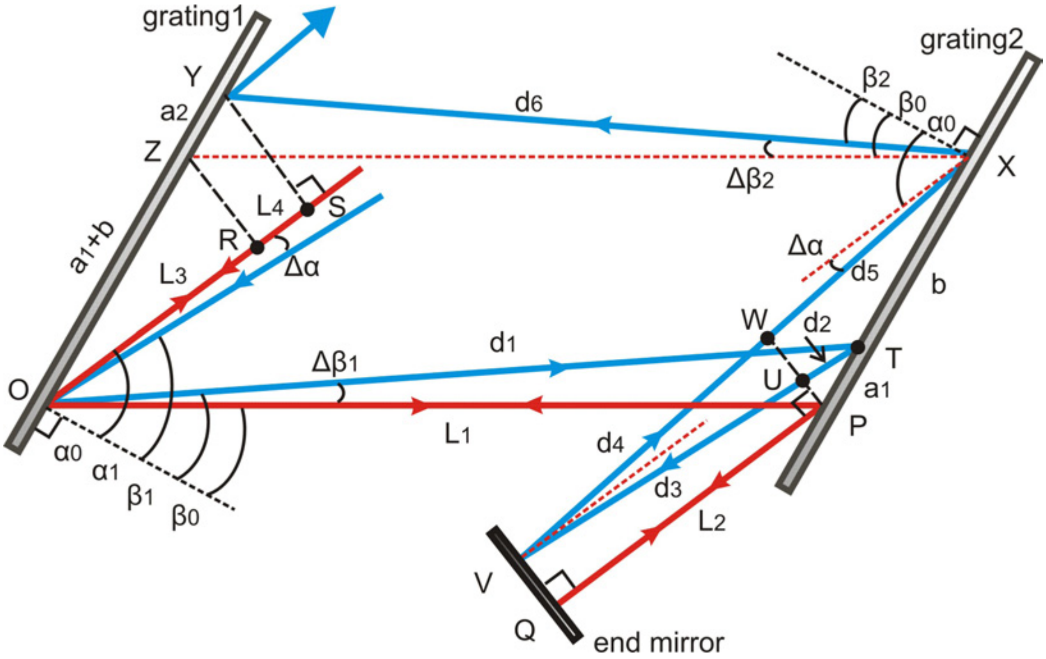

Figure 5.5: Ray diagram illustrating the change in the optical path of a wavelength component λ_0 due to the beam pointing $\Delta\alpha$ at the input of a grating compressor. The red and blue curves correspond to the AOI of α_0, and α_1 $(= \alpha_0 - \Delta\alpha)$, respectively. See text for more details.

The beam pointing fluctuations at the input of a grating compressor, from one shot to another, can be considered as a deviation $\Delta\alpha$ of the AOI of incoming beam from its design value (α_0). This variation results in a change in the diffraction angles (cf. Eq. 5.1) and a non-zero AOI at the end mirror, hence leading to a different optical path for the λ_0 ray for the first and second pass as shown in blue in Fig. 5.5. A change in the optical path length of the λ_0 ray, due to such deviation in the AOI, will constitute a timing jitter between the respective shots. It is worth mentioning that the described situation is different compared to that presented in Chapter 2 showing the dispersion of a grating compressor at different AOI's (Fig. 2.3(b)). Those calculations were intended to select an appropriate AOI for the grating compressor. The end mirror in that case was taken to be perpendicular to rays for every AOI of the incoming laser beam. However, in the present case we study the effect of a deviation of the AOI of the laser beam from its designed valued after it is aligned for a specified AOI and the end mirror cannot be considered perpendicular to each pulse any more.

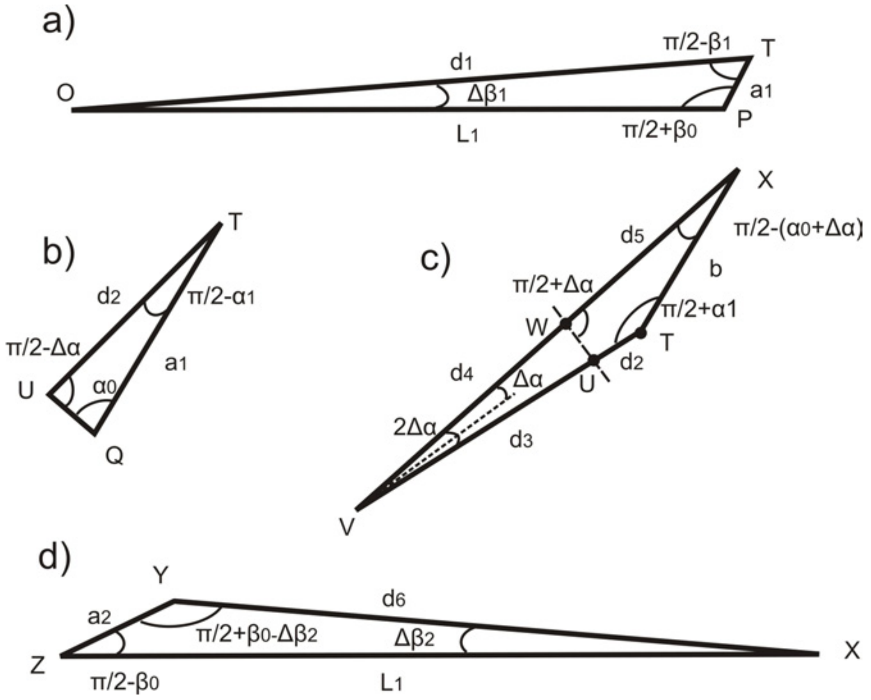

Figure 5.6: Geometrical construction of the optical path of λ_0 ray for calculation of different distances from d_1 to d_6 corresponding to the AOI of α_1, reproduced from blue curve in Fig. 5.5.

From the optical construction shown in Fig. 5.5 the path lengths $P(\lambda_0)|_{\alpha_0}$ and $P(\lambda_0)|_{\alpha_1}$ of the λ_0 ray, between the entrance and exit points (O and YS), corresponding to the AOI of α_0 and α_1, respectively, are calculated as under

$$\begin{aligned} P(\lambda_0)|_{\alpha_0} &= \overline{OP} + \overline{PQ} + \overline{QP} + \overline{PO} + \overline{OR} + \overline{RS} \\ &= L_1 + L_2 + L_2 + L_1 + L_3 + L_4, \end{aligned} \tag{5.2}$$

and

$$\begin{aligned} P(\lambda_0)|_{\alpha_1} &= \overline{OT} + \overline{TU} + \overline{UV} + \overline{VW} + \overline{WX} + \overline{XY} \\ &= d_1 + d_2 + d_3 + d_4 + d_5 + d_6. \end{aligned} \tag{5.3}$$

The difference in arrival times of the pulses after the compressor can be calculated from the difference of optical paths from Eqs. 5.2 and 5.3 as follows

$$\begin{aligned} \Delta\tau_{ext} &= \left| \frac{P(\lambda_0)|_{\alpha_0} - P(\lambda_0)|_{\alpha_1}}{c} \right| \\ &= \left| \frac{d_1 + d_6 - 2L_1}{c} + \frac{d_2 - L_4}{c} + \frac{d_3 + d_4 + d_5 - 2L_2 - L_3}{c} \right|, \end{aligned} \tag{5.4}$$

where c is the speed of light in vacuum. The derivation of the different optical paths described in Eqs. 5.2 and 5.3 follows the general trigonometric relations and optical constructions shown in Figs. 5.5, 5.6 as follows:

$$d_1 = L_1 \cdot \frac{\cos\beta_0}{\cos(\beta_0 + \Delta\beta_1)}; \tag{5.5}$$

$$d_2 = a_1 \cdot \frac{\sin\alpha_0}{\cos\Delta\alpha}, \tag{5.6}$$

where

$$a_1 = L_1 \cdot \frac{\sin\Delta\beta_1}{\cos(\beta_0 + \Delta\beta_1)}; \tag{5.7}$$

$$d_4 = d_3 = \frac{L_2}{\cos\Delta\alpha}; \tag{5.8}$$

$$d_5 = (d_2 + d_3) \cdot \frac{\cos\alpha_1}{\cos(\alpha_0 + \Delta\alpha)} - d_4; \tag{5.9}$$

$$d_6 = L_1 \cdot \frac{\cos\beta_0}{\cos(\beta_0 - \Delta\beta_2)}; \tag{5.10}$$

$$L_3 = (a_1 + a_2 + b)\sin\alpha_0, \tag{5.11}$$

where

$$a_2 = L_1 \cdot \frac{\sin\Delta\beta_2}{\cos(\beta_0 - \Delta\beta_2)}, \tag{5.12}$$

$$b = (d_2 + d_3) \cdot \frac{\sin(2\Delta\alpha)}{\cos(\alpha_0 + \Delta\alpha)}; \tag{5.13}$$

and

$$L_4 = a_2 \sin\alpha_0. \tag{5.14}$$

Recalling the grating equation (from Eq. 5.1) we have

$$\Delta\beta_1 = \arcsin(mN\lambda_0 - \sin(\alpha_0 - \Delta\alpha)) - \beta_0, \tag{5.15}$$

and

$$\Delta\beta_2 = \beta_0 - \arcsin(mN\lambda_0 - \sin(\alpha_0 + \Delta\alpha)). \tag{5.16}$$

The other parameters such as α_0, L_1, L_2, and N are specific to the experimental setup. We use $\alpha_0 = 58.5°$, $L_1 = 6$ m, $L_2 = 3$ m, $\lambda_0 = 1030$ nm, and N= 1740 lines/mm as for our setup.

Solving Eq. 5.4 for individual terms, it can be seen that the respective contribution of the 3rd term to the total timing jitter is 2 orders of magnitude smaller than the others. Neglecting this term we have

$$\begin{aligned}\Delta\tau_{ext} &\approx \left|\frac{d_1 + d_6 - 2L_1}{c} + \frac{d_2 - L_4}{c}\right| \\ &= \pm\frac{L_1}{c}\left(\frac{\cos\beta_0}{\cos(\beta_0 + \Delta\beta_1)} + \frac{\cos\beta_0}{\cos(\beta_0 - \Delta\beta_2)} - 2\right) \\ &\pm\frac{L_1}{c}\left(\frac{\sin\Delta\beta_1}{\cos(\beta_0 + \Delta\beta_1)} \cdot \frac{\sin\alpha_0}{\cos\Delta\alpha} - \frac{\sin\Delta\beta_2}{\cos(\beta_0 - \Delta\beta_2)} \cdot \sin\alpha_0\right)\end{aligned} \tag{5.17}$$

A non-zero value of $\Delta\tau_{ext}$ in Eq. 5.17 is, mainly, due to two factors: i) the difference of AOI's on grating1 and grating2 at points O and X, respectively (cf. Fig. 5.7), causing $(d_1 + d_6) \neq 2 \times L_1$; and ii) the inequality of the angles $\Delta\beta_1$ and $\Delta\beta_2$ due to the asymmetry of diffraction from the grating about central angle (β_0) (cf. Eqs. 5.15, 5.16), resulting in $a_1 \neq a_2$ (hence $d_2 \times \cos\Delta\alpha \approx d_2 \neq L_4$). However, these two factors only become prominent for significantly large amplitudes of beam pointing fluctuations. For $\Delta\alpha \to 0$, we get $(d_1 + d_6) \approx 2 \times L_1$ and $d_2 \approx L_4$. As a consequence, the increase (or decrease) in optical path in the first pass is compensated by a nearly equal decrease (or increase) in the second pass.

As shown in Fig. 5.7, the calculated timing jitter $\Delta\tau_{ext}$ is less than ± 6 fs for the beam pointing fluctuations of ± 50 μrad at the input of the compressor. Our system exhibits the shot-to-shot pointing fluctuations of ± 2 μrad and ± 4 μrad at the input of the stretcher and compressor, respectively, as measured via a WinCam device (DataRay Inc.), which correspond to a timing jitter of <1 fs (Fig. 5.7). Owing to the fact that a parallel grating compressor is matched with its equivalent Martinez-stretcher in term of introduced dispersions and effective optical path lengths, as detailed in Chapter2, we can safely assume that this effect will be similar in the stretcher. It can, therefore, be concluded that the timing jitter due to the beam pointing at the input of the stretcher or compressor in our setup is negligible.

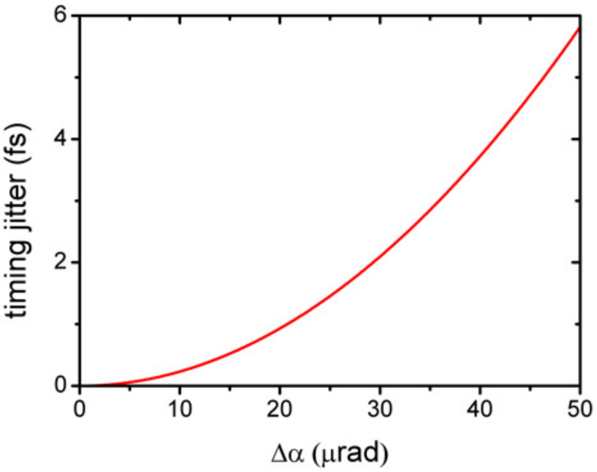

Figure 5.7: Calculated timing jitter due the pointing fluctuations at the input of the grating compressor.

In these calculations we assumed that there was no source of pointing fluctuations inside the compressor which is only valid if the compressor is enclosed in an evacuated or airtight housing. However in a setup, like ours, which is not isolated from such fluctuations, we have to analyse their contribution as well. Therefore we studied the effect of pointing fluctuations originating inside the grating compressor, mainly, due to air turbulences or mechanical vibration of optomechanics. The details are described in the following section.

5.2.5 Timing jitter due to the change in beam pointing inside the compressor

The ray diagram of a wavelength component λ_0 in a grating compressor for the calculation of timing jitter due to the pointing fluctuations inside the compressor is shown in Fig. 5.8. Here the optical path of the λ_0 ray for an AOI α_0 on the grating1 and no pointing fluctuation inside the compressor is shown in red (solid-curve).

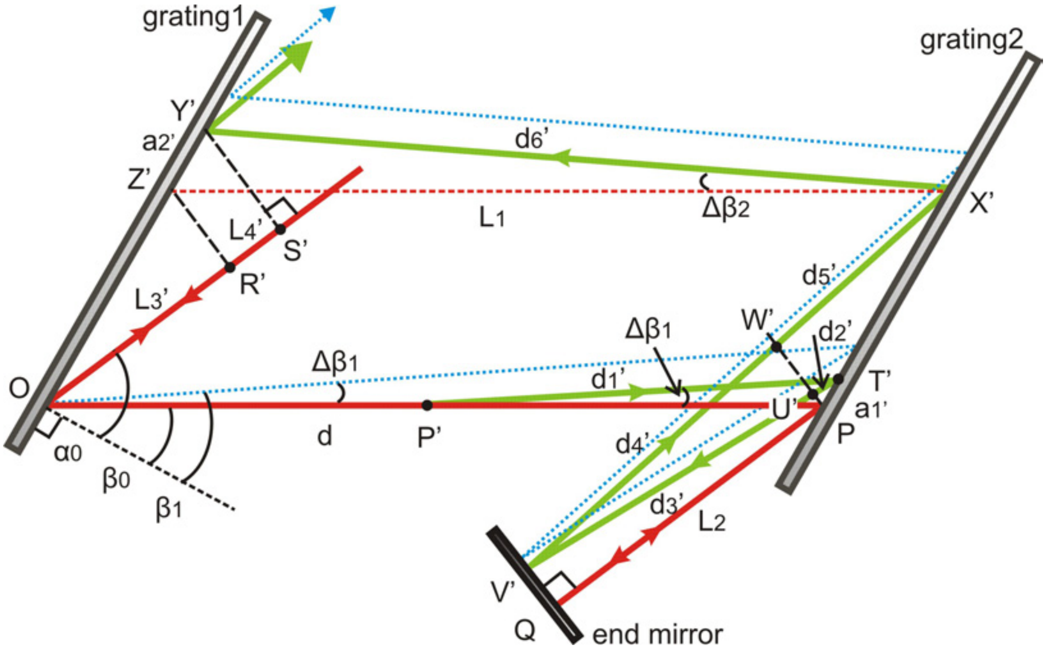

Figure 5.8: Ray diagram illustrating the change in the optical path of a wavelength component (λ_0) due to the beam pointing ($\Delta\beta_1$) originating from an arbitrary point P' inside the compressor (green curve). The dotted-blue curve represents the optical path when the point P' is at $d = 0$, whereas the red curve corresponds to that when there is no disturbance at P'.

Let us consider a perturbation taking place at a point P', at a distance d from grating1, during the first pass which deflects the optical ray by an angle $\Delta\beta_1$ from its original path. The deflected ray subsequently follows the green curve and impinges on grating2 at an AOI of β_1 $(= \beta_0 + \Delta\beta_1)$, hence leading to a different optical path as shown in Fig. 5.8. The optical path shown in dotted-blue corresponds to the situation when the disturbance occurs at the point of incidence (O) on grating1. This condition is identical to that described in the previous section for the AOI of α_1 (cf. Fig 5.5).

The optical path length of the ray between O and $S'Y'$ undergoing deflection $\Delta\beta_1$ due to the perturbation at point P' is given by

$$\begin{aligned} P(\lambda_0)|_{\beta_1} &= \overline{OP'} + \overline{P'T'} + \overline{T'U'} + \overline{U'V'} + \overline{V'W'} + \overline{W'X'} + \overline{X'Y'} \\ &= d + d_1' + d_2' + d_3' + d_4' + d_5' + d_6'. \end{aligned} \tag{5.18}$$

Similarly the optical length of the ray experiencing no perturbation can be written as

$$\begin{aligned} P(\lambda_0)\,|_{\beta_0} &= \overline{OP}+\overline{PQ}+\overline{QP}+\overline{PO}+\overline{OR'}+\overline{R'S'} \\ &= L_1+L_2+L_2+L_1+L_3'+L_4'. \end{aligned} \tag{5.19}$$

The equivalent timing jitter can be derived, similar to Eq. 5.4, as follows

$$\Delta\tau_{int} = \left|\frac{P(\lambda_0)\,|_{\beta_0} - P(\lambda_0)\,|_{\beta_1}}{c}\right| \approx \left|\frac{d+d_1'+d_2'+d_6'-2L_1-L_4'}{c}\right|. \tag{5.20}$$

Owing to the symmetry of the optical constructions presented in Figs. 5.5 and 5.8, the Eqs. 5.5–5.14 can be used to derive the distances $d_1' \cdots d_6'$; and L_3', L_4'. The only modification needed in this case is to replace L_1 in Eqs. 5.5 and 5.7 by $(1-d/L_1)L_1$. The other parameters such as α_0, L_1, L_2, λ_0, and N are similar to the previous section.

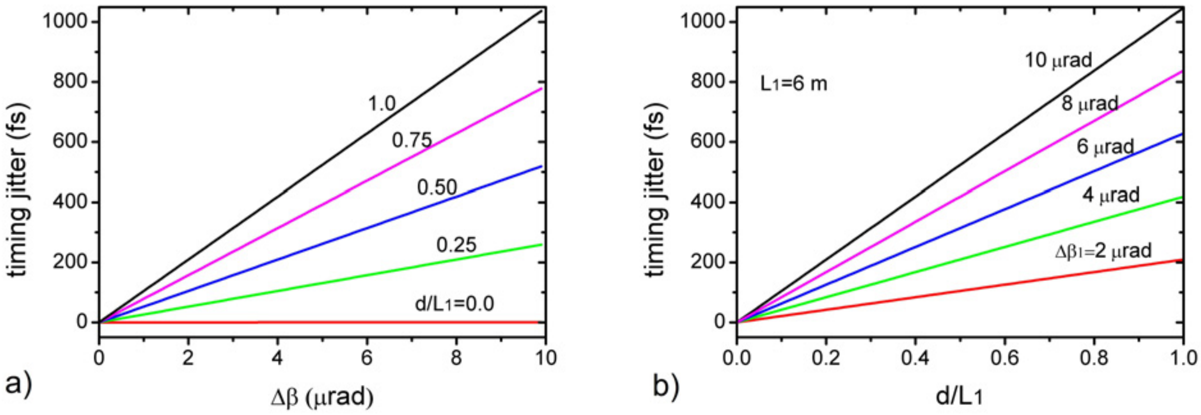

Figure 5.9: Calculated timing jitter of the pulses due to the change in the beam pointing $(\Delta\beta_1)$ inside the compressor. Dependence of the timing jitter on: a) $\Delta\beta_1$ for different values of d/L_1 ranging from 0 to 1; b) d/L_1 for different values of $\Delta\beta_1$ ranging from 2 μrad to 10 μrad, where d is the distance of P' from grating1 and $L_1 = 6$ m.

Fig. 5.9a) shows the relative timing difference of the pulses at the output of the compressor, derived from Eq. 5.20, as a function of change $(\Delta\beta_1)$ in the beam pointing for different distances from grating1 specified by d/L_1= 0.0, 0.25, 0.50, 0.75, and 1.0. It can be seen that the timing jitter, for a specific value of d/L_1, changes linearly w.r.t the internal pointing fluctuations of the compressor. Moreover it depends on the position of the source of perturbation between the gratings. For a particular value of $\Delta\beta_1$, the timing jitter grows linearly with an increase in distance d from grating1 (Fig. 5.9(b)). Even for a small small change of 2 μrad in beam pointing, the calculated timing jitter changes from 0.01 fs to 210 fs as d approaches L_1. Compared to the case when pointing fluctuations take place outside, the calculated timing jitter is four orders of magnitude higher for $d = L_1$. This significant difference is due to the fact that, in case of a change in the beam direction inside the grating compressor (i.e. $d/L_1 \neq 0$), the timing jitter is dominantly contributed by the effect of broken symmetry between the distances a'_1 and a'_2 (Fig. 5.8). The optical path length d'_2 vanishes as $d/L_1 \to 1$, hence L'_4 will no longer be compensated by d'_2. This effect is absent for the case discussed in previous section.

Owing to the fact that the measured timing jitter of ±200 fs, shown in Fig. 5.3(b), corresponds to many combinations of $\Delta\beta_1$ and d in Fig. 5.9, therefore it can be inferred that the pointing fluctuations inside the stretcher and compressor are mainly responsible for our measured jitter.

The possible source of such fluctuations can be the air turbulences since the stretcher and compressor are not enclosed in vacuum enclosures. These calculations are also strictly valid for mechanical instability of the optomechanics in the stretcher, other than the grating mount. In order to calculate the effect of a change in beam pointing due to the mechanical vibrations of the grating mounts, an angular tilt of the respective grating along its dispersion plane (i.e. about an axis parallel to the grooves) have to be assumed. However the change in the optical path length due to this modification will be negligible. Therefore the same calculations can be used for pointing fluctuations arising from the mechanical vibrations of grating mounts.

We can conclude that the beam pointing fluctuations inside the stretcher and compressor setups should be avoided to get rid of the timing jitter. They arise mainly from the air turbulence requiring vacuum enclosures.

By actively stabilizing the pump-seed timing, we can continue to investigate the short-pulse-pumped OPCPA in DKDP, crucial point in PFS development.

5.3 OPCPA experiments in DKDP

Since the discovery of OPA a large variety of nonlinear optical crystals have been utilized, newly introduced and engineered in order to optimize the amplification process in terms of the achievable amplification bandwidth. BBO (β-BaB_2O_4), PPLN (periodically poled $LiNbO_3$), LBO ($LiBM_3O_5$) and KTP ($KTiOPO_4$) are most commonly used due to their high nonlinear coefficients, availability and broad gain bandwidths in the visible and NIR spectral range [4, 153, 60, 154, 155, 156, 157, 158, 159, 160, 161]. A sub-3 cycle, 16 TW light source, which utilizes BBO as an amplification medium, is already in operation [156]. However, these crystals are only available in limited sizes, i.e. present-day technology can provide a maximum aperture of only a few centimeters for BBO and even less for PPLN. In order to generate Joule-scale amplified pulse energies, as in case of the PFS, crystal apertures of the order of few tens of centimeters are needed to avoid optical damage and unwanted nonlinearities. Alternative crystals such as, KDP (KH_2PO_4), DKDP (KD_2PO_4) [161] and CLBO ($CsLiB_6O_{10}$) [162] become attractive for such systems despite their comparatively lower nonlinearity, as they can be grown in sizes of 40 cm and more in aperture. Since the gain bandwidth of DKDP exceeds that of KDP and CLBO [161, 163], this has been the crystal of choice for the final amplification stages in recent high-power projects [62, 75]. Although it has been demonstrated that DKDP is suitable for the amplification of narrowband pulses to the PW-level, e.g. 43 fs in 0.56 PW [75], an experimental evidence of its ability to amplify an even broader spectral bandwidth that can support few-cycle pulses is yet to be done. As predicted by theory [2] such a broadband gain can be achieved by a thin DKDP crystal and pumping with high power few-ps pulses in a non-collinear geometry. Scaling this scheme to high power can be achieved by using large aperture DKDP crystals, as for the PFS system. We present in the following the first such measurement confirming broadband amplification in DKDP, its scaling up to the Petawatt level will be presented in the future work of this group at the MPQ during the developement of the PFS system. The main objective of this experiment was to verify the suitability of the frontend light source, described in this dissertation, to serve as a seed source for this high power system.

For these measurements a small fraction ($\sim$800 μJ) of the total available pump laser energy at 515 nm is used with a FWHM duration of $\sim$2 ps, i.e. slightly longer than the best achievable performance, since in this way the effect of the residual timing jitter can be reduced further. The pump-pulse duration was adjusted by clipping the spectrum inside the grating compressor. These measurements were performed under the condition when the active stabilization of timing jitter was ON. For the amplification measurements we worked in the focus of both the pump and seed beams and thereby obtained near-Gaussian beam profiles in the OPA crystal of 1/e^2 beam diameters of 1.3 mm and 1.2 mm, respectively. The pump intensity was limited to $\sim$100 GW/cm^2, which can be regarded as a safe mode of operation, since the AR coating of the DKDP crystal (515 nm and 700–1400 nm) is the limiting factor in terms of damage in the amplifier stage and its damage threshold was measured to be $\sim$300 GW/cm^2 in our experiment. The internal non-collinear angle (α_{int}) between the pump and signal was fixed at $\sim$0.8°, very close to what was suggested by the theory [2]. The broadband seed spectrum after the cascaded HCF is shown in Fig. 5.10. It has a spike at 720 nm which is approximately two orders of magnitude higher than the spectral intensity at 1000 nm. Since this peak can quickly saturate the spectrometers and other diagnostics we used a 2 mm-thick RG1000 bandpass filter to strongly suppresses the spectral range below 800 nm, and hence the main peak at 720 nm, in order to increase the dynamic range of our diagnostics. The spectrum after the RG1000 filter is also shown in Fig. 5.10(a). The energy of the broadband seed after the RG1000 filter was $\sim$4.5 μJ .

The seed pulse after the RG1000 filter was stretched by changing the prism separation in the stretcher (Sec. 4.5) in such a way to have a GD of $\sim$1.5 ps for a spectral range of 800–1325 nm, as shown in Fig. 5.10(b). A 7 mm-thick DKDP crystal was used for the parametric amplification

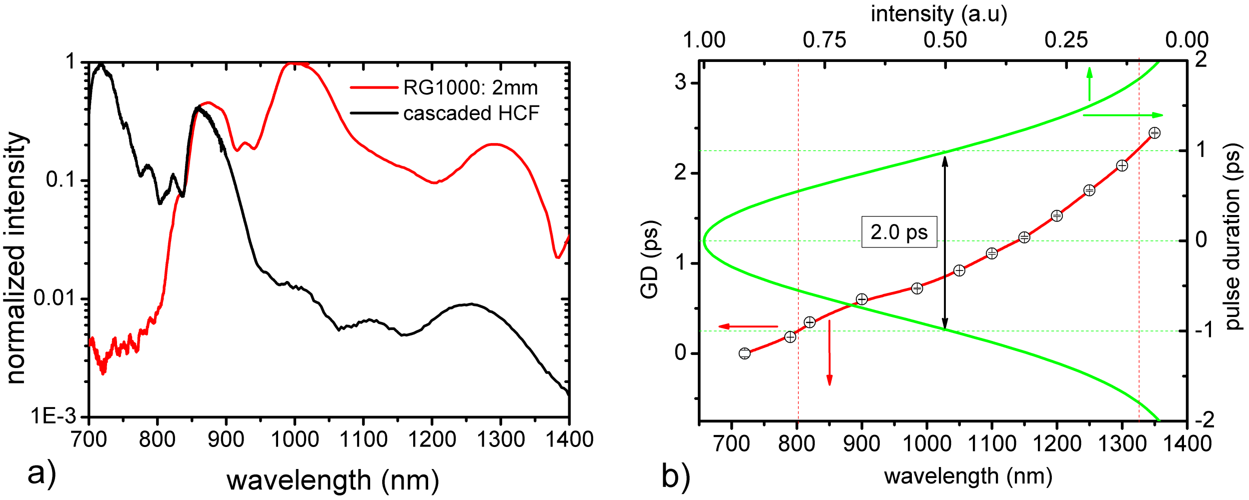

Figure 5.10: a) Broadband OPCPA seed spectra at the output of cascaded HCF and after 2-mm thick RG1000. The spectra are normalized to the peak values. b) Scheme of stretching the OPCPA seed: The seed is stretched in a way that its NIR-tail (800-1325 nm) fits in the FWHM duration of the pump pulse. The presented GD is characterized using the technique described in Sec. 4.5.

of the broadband seed. The phase matching angle was adjusted to be $\sim 37°$. During alignment of the DKDP crystal, we observed high sensitivity of the broadband gain and its overall shape on the phase matching angle. As fine as $< 0.1°$ of accuracy of the phase matching angle is required for a reproducible gain. Moreover we observed that when the phase matching angle was decreased from the optimum value of $\sim 37°$, the amplification extended more and more into the near infrared region with a hump in the middle of the gain spectrum, and vice versa. This dependence of the gain on the phase matching angle helps in shaping the amplified spectrum. We therefore adjusted the phase matching angle at this stage in a way to have amplification in the weaker part (i.e. NIR tail) of our broadband seed spectrum with its maximum close to 1150 nm, so that it could be smoothly amplified in the rest of the OPCPA stages of the PFS. Under these conditions by injection of 4.4 μJ seed energy, 53 μJ of amplified signal is obtained. This corresponds to an overall gain of 9.6 and an extraction efficiency of 6% from pump to signal. The broadband gain ranges from $\sim$800 to 1300 nm. Owing to the RG1000, the spectrum below 800 nm is significantly suppressed, therefore we cannot get any information of gain below this spectral range. We believe that in reality the gain can be even higher. Figure 5.11(a) shows the input and the amplified spectrum and the broadband gain is presented in Fig. 5.11(b). The amplified spectrum supports the sub-two cycle pulse for 1050 nm carrier wavelength with a FWHM duration of 6.1 fs.

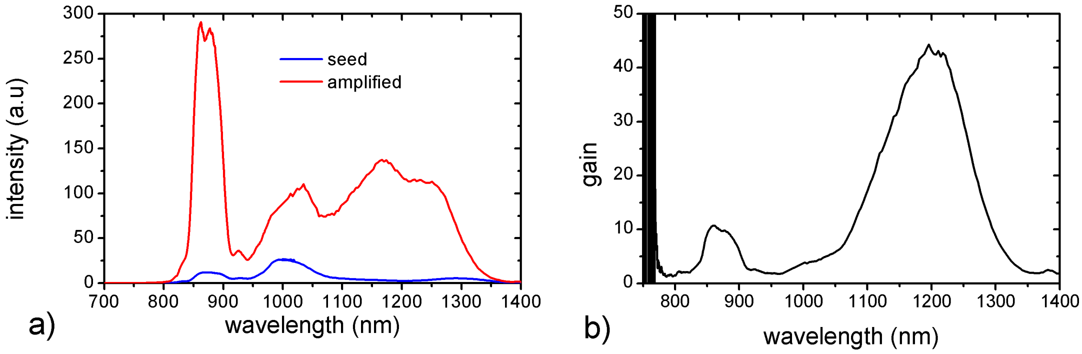

Figure 5.11: a) The amplified and unamplified spectra, using 7mm DKDP under saturation condition. b) amplified gain extracted from a).

5.4 Conclusion

We have quantitatively investigated the level of timing synchronization between the pump and seed pulses at the position of first OPCPA stage of the PFS system. Using the spectral gating technique it is demonstrated that the stretcher-compressor setup for the CPA chain of pump laser is the main source of timing jitter in our system. By means of theoretical calculations we conclude that this timing jitter arises from the beam pointing fluctuations inside the stretcher and compressor caused by the air turbulences in our setup. This conclusion is also strengthened from the fact that by introducing beam tubes inside the compressor as well as building a housing around the stretcher, the described timing instabilities were significantly reduced as presented in Figs. 5.3(a,b). The possible solution to get rid of these air fluctuations, hence the timing jitter, would be to use air-tight enclosures or vacuum chambers both for the stretcher and compressor setups of the CPA pump laser. We expect significant decrease in the shot-to-shot timing jitter after installation of these enclosures. In order to prepare the system for the first short-pulse pumped OPCPA experiments an active synchronization system was installed to eliminate the slow drift at a repetition rate of 10 Hz. This improvement helped to reduce the relative timing jitter to $\sim$100 fs. The performance of this system can still be further improved by using fast data acquisition electronics and incorporating a piezo-stage which has relatively faster response time than the present motor driven stage.

Using the pump and seed pulses with the above described synchronicity, we have demonstrated that the short-pulse pumped parametric amplification in DKDP is feasible with our developed frontend light source and that it can deliver a sufficiently broad spectrum (cf. Fig. 5.11(a)) as well as with reasonable gain to support sub-two-cycle pulse duration.

Chapter 6

Summary and outlook

In the search for a way to generate few-cycle ultrahigh-power light pulses with pulse energies in the Joule range, short-pulse pumped OPCPA has been identified as a promising option for a viable path. The PFS system at MPQ in Garching will be the first embodiment of this novel scheme using picosecond pump pulses for the ultrabroadband parametric amplification. Owing to its unique parameters, the PFS development represents unexplored territory, and thus contains a large number of scientific and technological challenges on the way.

In this work we have tackled a crucial aspect of the PFS project, namely the development of a frontend light source. It provides optically synchronized seed pulses for both the pump-laser chain and the main OPCPA chain. This frontend system is based on a Ti:sapphire oscillator-amplifier system. The seed pulse for the Yb:YAG CPA pump-laser chain is generated using a soliton-based spectral shifting scheme of part of the output power of the Ti:sapphire oscillator to 1030 nm. The spectrum of the seed pulse in the short-pulse OPCPA scheme is required to be in the wavelength range between 700–1400 nm. We used a cascaded hollow core fiber spectral broadening scheme to produce this seed pulse from the Ti:sapphire source. With this scheme we are able to generate sufficient spectral intensity in the required near-infrared range for seeding the OPCPA chain.

In order to perform the first OPA experiments with the PFS system, the accurate synchronization of the pump and seed pulses for the OPA is crucial. This stringent requirement is the main drawback of short-pulse pumped OPCPA. We addressed this issue by characterizing the timing jitter quantitatively. In spite of the optical synchronization of the pulses an active stabilization of the relative arrival times of the two pulses was needed in order to reduce the timing jitter to a level ($\sim$100 fs) at which meaningful parametric amplification experiments can be conducted. Through some theoretical considerations we also identified the source of the large timing jitter to be the long beam propagation paths in the stretcher-compressor setup of the pump-laser chain which can be affected by air turbulences.

We have demonstrated the first broadband parametric amplification experiments in DKDP, which proves that our frontend and the pump-seed synchronization are suitable for the picosecond-pumped OPCPA scheme. This now enables us to conduct systematic studies into the validity of our design calculations and thereby provide experimental support for the entire PFS design. These investigations are currently under way at MPQ. Immediate further steps for the PFS development include the demonstration of the compressibility of the amplified pulses and the experimental proof of the expected high contrast. These studies are also being currently carried out at MPQ.

By the work presented in this thesis we have created the necessary prerequisites for the experimental demonstration of the short-pulse pumped OPCPA scheme for Joule-scale few-cycle pulse generation within the framework of the PFS project. While PFS represents the prototype of this technology, the billion-euro-scale Pan-European installation, the Extreme Light Infrastructure (ELI [68]), is planning to use PFS technology for its frontend architecture due to the aspired parameters (Joule-scale pulse energies with few-cycle pulse durations). This fact further underlines the importance of our presented investigations.

Once the PFS light source is completed, it will allow for first laser-matter interaction experiments which constitute the main motivation behind this infrastructure-development project. The few-cycle ultrahigh-power pulses are expected to generate single attosecond pulses in an interaction with a solid surface with unprecedentedly high intensities and also photon energies, thereby accessing an entirely new regime of attosecond science [39]. In addition, it is expected that the acceleration of monoenergetic electron bunches will also benefit from such a unique driver pulse in terms of a narrow energy distribution, stability and reproducibility, and an increase of the bunch charge [164].

Beside the work directly benefiting the PFS development, additional scientific and technological advancements have emerged from the presented work, which we will summarize in the following. Firstly, a hybrid pulse compression scheme, using a combination of prisms and high-dispersive negatively chirped mirrors, was introduced [111, 113] to resolve the problem of self-phase modulation in purley prism-based compressors of few-10-fs sub-TW CPA laser systems. This effect was previously limiting the performance of these systems in terms of spatio-temporal beam profile of the compressed pulses. In addition, an alternative scheme for pulse compression in this peak-power and pulse-duration regime, using purely the HDM's was presented [49, 165]. Since an all-dispersive-mirror compressor (ADMC) is intrinsically free from nonlinear effects, and spatial and angular chirps, it eradicates all main hurdles of CPA-systems in reaching near bandwidth-limited compressed pulses with excellent spatial quality. Moreover, it provides remarkable simplifications in dispersion management, compared to the conventional grating/prism-based setups. This approach, therefore, opens the way towards simple, compact, user-friendly, and alignment insensitive sub-terawatt-scale prism/grating-free femtosecond laser systems.

Secondly, with the double-angle dispersive mirror (DADM) technology we demonstrated pulse compression to below two-cycle pulse duration [140], exploiting the inherent advantages of this novel mirror technology over the conventional complimentary-chirped mirror approach [105]. These pulses generated by DADM compression technology have recently been used for the acceleration of electrons from nanospheres [166]. This shows the potential for generating pulses of extreme ultraviolet light for biological and medical research. Another implication of this electron acceleration technique is its use in light-controlled ultrafast electronics, holding promise to work up to one million times faster than conventional electronics [166].

Finally, during our efforts to obtain a spectrally broadened seed pulse in the near infrared range, using our cascaded HCF scheme we achieved a supercontinuum spanning nearly three-octaves. Such a spectrum supports a single-cycle pulse duration which can revolutionize the fields of ultrafast spectroscopy [33], electron acceleration using nanospheres [166], higher order harmonic generation [29], and attoscience [30, 32].

Appendix A

List of optical components in the current CPA pump laser chain

Optical component	**Material**	**Thickness [mm]**	**round trips /pieces**
Polarizer cube	BK7	10	2
Fiber amplifier	Silica glass	1400	1
Lens	BK7	4	6
Prism	BK7	20	1
QWP	Crystal Quartz	0.147	1
HWP	Crystal Quartz (o)	0.177	2
Pockels cell	DKDP (e)	36	1
Crystal	TGG	21	1
Compensator plate	Crystal Quartz	4	2
QWP	BK7	0.147	200[a]
Pockels cell	DKDP	36	200
Glass	fused silica	6	200
TFP	BK7	16	2
Polarizer	Calcite (e)	16	4
Crystal	TGG	21	1
Yb:YAG	Yb:YAG	8	8

---

[a] 100 round trips in the regenerative amplifier

TFP: thin-film polarizer; HWP: half-wave plate; QWP: quarter-wave plate; see [71, 72] for more details.

Appendix B

Dispersion calculations of a double-prism pair compressor

The schematic sketch of the double-prism pair compressor is shown in Fig. B.1(a). Four prisms with an identical apex angle α_p are arranged for the angles of minimum deviation at the central wavelength λ_0 of the input-pulse spectrum. θ_i and φ_i $(i = 1 \cdots 8)$ denote the respective angles of incidence and refraction at eight interfaces. The dispersion introduced by the prism compressor is a cumulative effect of angular as well as material dispersions, which have different signs for the GDD [100]. The effective GDD of the prism compressor can therefore be written as

$$\left.\frac{\mathrm{d}^2\Phi(\omega)}{\mathrm{d}\omega^2}\right|_{eff} = \left.\frac{\mathrm{d}^2\Phi(\omega)}{\mathrm{d}\omega^2}\right|_{ang} + \left.\frac{\mathrm{d}^2\Phi(\omega)}{\mathrm{d}\omega^2}\right|_{mat}. \tag{B.1}$$

The angular dispersion can be calculated for the so-called principle arrangement, as introduced by Cheng et al. [50]. The spectral components at λ_0 travel through the vertices of all prisms i.e., along the curve *BCDEF* (Fig. B.1(a)). The wavelengths smaller than λ_0 (denoted by λ_s) fly out of prism P_2 at its apex C, while the λ_ℓ's with $\lambda > \lambda_0$ escape at D. So the material dispersion for this configuration will be negligible. The GDD due to the angular dispersion is therefore given by

$$\left.\frac{\mathrm{d}^2\Phi(\omega)}{\mathrm{d}\omega^2}\right|_{ang} = 2\cdot\frac{\lambda^3}{2\pi c}\,\frac{\mathrm{d}^2P(\lambda)}{\mathrm{d}\lambda^2}, \tag{B.2}$$

where $P(\lambda)$ is the total optical path length along curve *BCDEF*, and $\Phi(\omega)$ represents the overall spectral phase delay introduced by the optical system. The factor of 2 is for the double-pass configuration. $P(\lambda)$ can be calculated using optical construction adapted by Fork et al. [47] and by Cheng et al. [50] as follows

$$P(\lambda) = \ell_0 + \ell_1\cos\beta_1(\lambda) + L\cos\beta_2(\lambda) + \ell_2\cos\beta_3(\lambda) + \ell_3 \tag{B.3}$$

Here $\beta_i(\lambda)$, for $i = 1\cdots 3$, are the angles of an arbitrary wavelength λ with reference λ_0

$$\beta_1(\lambda) = \varphi_2(\lambda) - \theta_1 \tag{B.4}$$

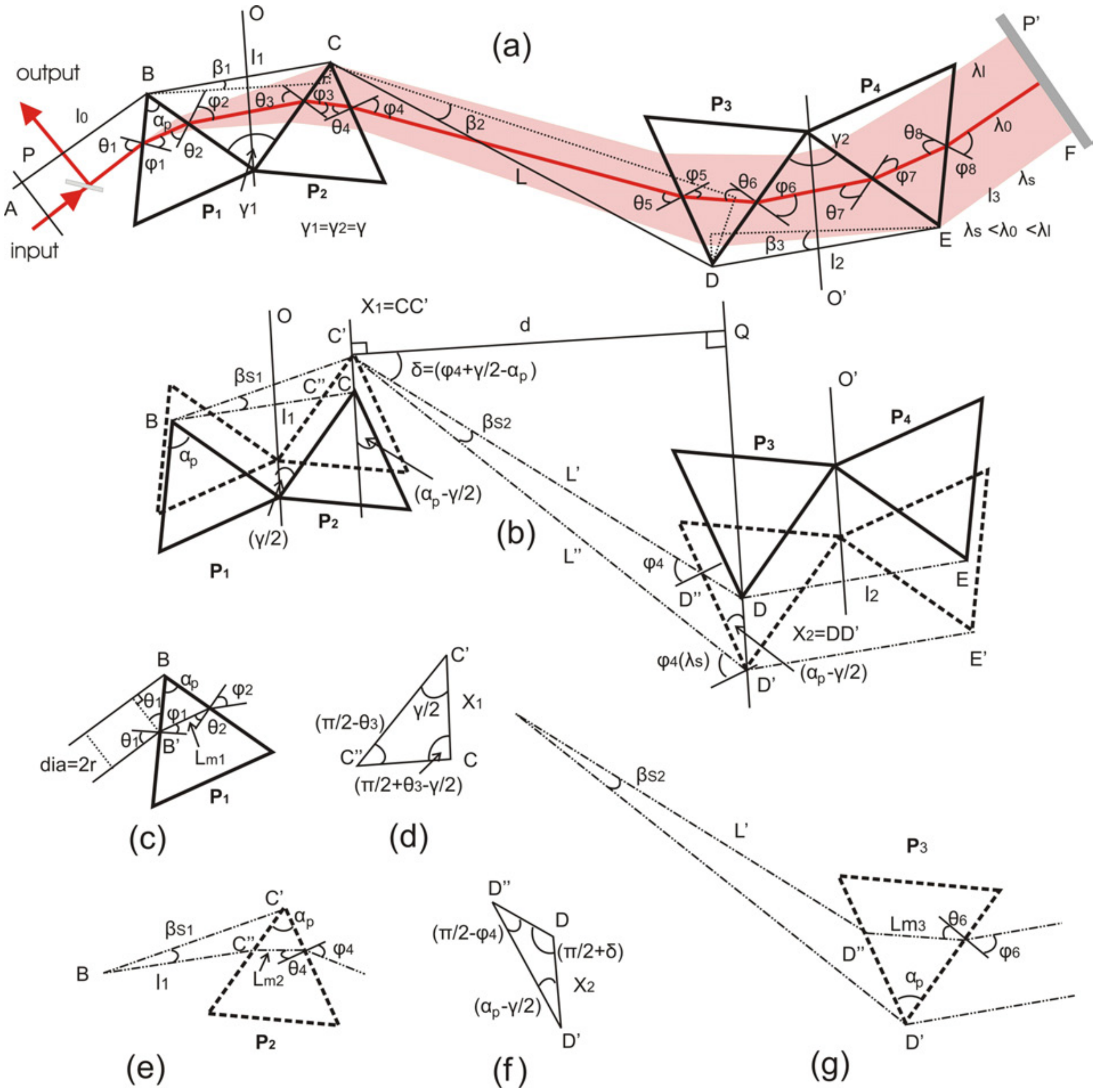
(a)
output
input
A
P
B
C
O
l1
l0
β1
θ1
φ1
θ2
φ2
θ3
φ3
θ4
φ4
αp
P1
P2
γ1
γ1=γ2=γ
β2
L
P3
P4
γ2
φ5
θ5
θ6
φ6
θ7
φ7
θ8
φ8
β3
D
E
l2
O'
P'
F
λl
λ0
λs
l3
λs <λ0 <λl
(b)
X1=CC'
C'
C''
d
Q
δ=(φ4+γ/2-αp)
βS1
βS2
(γ/2)
(αp-γ/2)
L'
L''
φ4
D''
D'
E'
X2=DD'
φ4(λs)
(c)
B'
dia=2r
Lm1
(d)
X1
(π/2-θ3)
(π/2+θ3-γ/2)
γ/2
(e)
Lm2
(f)
(π/2-φ4)
(π/2+δ)
X2
(αp-γ/2)
(g)
Lm3

Figure B.1: Sketch of the double-prism pair compressor. The optical arrangement is adapted from Ref. [50].

$$\beta_2(\lambda) = \varphi_4(\lambda_0) - \varphi_4(\lambda) \tag{B.5}$$

$$\beta_3(\lambda) = \theta_7(\lambda) - \varphi_8 \tag{B.6}$$

$$\begin{aligned} \frac{\mathrm{d}^2 P(\lambda)}{\mathrm{d}\lambda^2} &= \ell_1 \left\{ -\frac{\mathrm{d}^2\varphi_2(\lambda)}{\mathrm{d}\lambda^2} \sin\, \beta_1(\lambda) - \left[\frac{\mathrm{d}\varphi_2(\lambda)}{\mathrm{d}\lambda}\right]^2 \cos\beta_1(\lambda) \right\} + \\ & L \left\{ \frac{\mathrm{d}^2\varphi_4(\lambda)}{\mathrm{d}\lambda^2} \sin\, \beta_2(\lambda) - \left[\frac{\mathrm{d}\varphi_4(\lambda)}{\mathrm{d}\lambda}\right]^2 \cos\beta_2(\lambda) \right\} + \\ & \ell_2 \left\{ -\frac{\mathrm{d}^2\theta_7(\lambda)}{\mathrm{d}\lambda^2} \sin\, \beta_3(\lambda) - \left[\frac{\mathrm{d}\theta_7(\lambda)}{\mathrm{d}\lambda}\right]^2 \cos\beta_3(\lambda) \right\} \end{aligned} \tag{B.7}$$

For minimum deviation and Brewster incidence we have $\tan\theta_1 = n_p(\lambda_0)$, $\sin\theta_1 = n_p(\lambda_0)\sin(\alpha_p/2)$, $\gamma_1 = \gamma_2 = 2\theta_1$.

Using Snell's Law and the relation $\alpha_p = \varphi_1(\lambda) + \theta_2(\lambda) = \varphi_3(\lambda) + \theta_4(\lambda) = \varphi_5(\lambda) + \theta_6(\lambda) = \varphi_7(\lambda) + \theta_8(\lambda)$ yields $\varphi_2(\lambda) = \theta_7(\lambda)$ and $\beta_1(\lambda) = \beta_3(\lambda)$
Hence B.7 can be rewritten as

$$\begin{aligned} \frac{\mathrm{d}^2 P(\lambda)}{\mathrm{d}\lambda^2} &= (\ell_1 + \ell_2) \left\{ \frac{\mathrm{d}^2\varphi_2(\lambda)}{\mathrm{d}\lambda^2} \sin[\theta_1 - \varphi_2(\lambda)] - \left[\frac{\mathrm{d}\varphi_2(\lambda)}{\mathrm{d}\lambda}\right]^2 \cos[\theta_1 - \varphi_2(\lambda)] \right\} + \\ & L \left\{ \frac{\mathrm{d}^2\varphi_4(\lambda)}{\mathrm{d}\lambda^2} \sin[\varphi_4(\lambda_0) - \varphi_4(\lambda)] - \left[\frac{\mathrm{d}\varphi_4(\lambda)}{\mathrm{d}\lambda}\right]^2 \cos[\varphi_4(\lambda_0) - \varphi_4(\lambda)] \right\} \end{aligned} \tag{B.8}$$

The refraction angles $\varphi_2(\lambda)$ and $\varphi_4(\lambda)$ are given by

$$\varphi_2(\lambda) = \left[n_p(\lambda) \sin\alpha_p \cos\left[\arcsin\left(\frac{\sin\theta_1}{n_p(\lambda)}\right)\right] - \cos\alpha_p \sin\theta_1 \right] \tag{B.9}$$

$$\varphi_4(\lambda) = \arcsin\left[n_p(\lambda) \sin\alpha_p \cos\left[\arcsin\left(\frac{\sin\Gamma(\lambda)}{n_p(\lambda)}\right)\right] - \cos\alpha_p \sin\Gamma(\lambda) \right], \tag{B.10}$$

where $\Gamma(\lambda) = \gamma_1 - \varphi_2(\lambda)$
By substituting Eqs.B.8–B.10 in B.2, the GDD due to the angular dispersion can be calculated.

As discussed above, Eq. B.8 is only valid for the principle configuration for which the spectral components at λ_0 travel through the vertices of all prisms. This configuration is not feasible in a real setup because only the spectral component at λ_0 could be passed through the setup, i.e., λ_s and λ_ℓ clip off at points C and D, respectively (Fig. B.1(a)). In order to accommodate the λ_s components, the prism P_2, hence P_1 (being paired), is translated along axis O, as shown in Fig. B.1(b). Similarly, the prism pair P_3-P_4 is shifted parallel to the axis O' to capture the λ_ℓ wavelengths. The third such displacement of both prism pairs is caused by the spatial beam profile (beam diameter) of incoming pulse. These effects contribute material dispersion to the input pulse which is calculate as follows.

The GDD due to the prism material is given by

$$\left.\frac{\mathrm{d}^2\Phi(\omega)}{\mathrm{d}\omega^2}\right|_{mat} = 2\cdot\frac{\lambda^3}{2\pi c^2}\cdot L_m\frac{\mathrm{d}^2 n_p(\lambda)}{\mathrm{d}\lambda^2}, \tag{B.11}$$

where L_m is the total optical material length for a single pass through all the four-prisms (P_1–P_4) corresponding to the wavelength λ_0. The factor of 2 is for the double-pass configuration, as adapted in Eq. B.2. L_m can be subdivided into the individual contributions from each prism pair as

$$L_m = L_{m12} + L_{m34}, \tag{B.12}$$

where $L_{m12} = 2(L_{md} + L_{m2})$ and $L_{m34} = 2(L_{md} + L_{m3} + L_{m4})$ are the material lengths through the prism pairs P_1-P_2 and P_3-P_4, respectively (Fig. B.1(c–g)).

L_{md} is the material length through each prism (Fig. B.1(c)) due to the input beam diameter (denoted by $2r$) given by

$$L_{md} = \overline{BB'}\,\frac{\sin\alpha_p}{\cos\theta_2} = \frac{2r}{\cos\theta_1}\,\frac{\sin\alpha_p}{\cos\theta_2}, \tag{B.13}$$

where r is the beam radius. By using Snell's law, the angles θ_i ($i = 2\cdots 6$) at different interfaces can be calculated as follows

$$\theta_i = \begin{cases} \arcsin\left(n_p(\lambda_0)\sin\varphi_i\right) & \text{if } i = odd \\ \arcsin\left(\frac{\sin\varphi_i}{n_p(\lambda_0)}\right) & \text{if } i = even. \end{cases} \tag{B.14}$$

The angular spread (dispersion) from P_1 will cause P_2 to be moved by an additional amount X_1 in order to avoid the largest wavelength component of λ_ℓ to fly out as shown in Figure B.1(b).

$$X_1 = \ell_1\cdot\tan\beta_{s1} \tag{B.15}$$

where $\beta_{s1} = \varphi_2(\lambda_\ell) - \varphi_2(\lambda_0)$, and ℓ_1 is the apex-to-apex separation of P_1 and P_2 . This additional amount of material L_{m2} can be calculated from Figs. B.1(c- d) as follows

$$L_{m2} = \overline{CC'}\,\frac{\sin\alpha_p}{\cos\theta_4} = X_1\,\frac{\cos(\theta_3 - \gamma/2)}{\cos\theta_3}\,\frac{\sin\alpha_p}{\cos\theta_4} \tag{B.16}$$

where $\theta_3 = \Gamma(\lambda_0) = \gamma - \varphi_2$. The insertion of P_2 is adjusted so as to capture the shortest wavelength component of λ_s (see Figure B.1(b)) which causes P_2 to moved by an amount of X_2 given by

$$X_2 = d\cdot\tan(\delta + \beta_{s2}) - d\cdot\tan\delta \tag{B.17}$$

Where $\delta = (\varphi_4 + \gamma/2 - \alpha_p)$, $\beta_{s2} = \varphi_4(\lambda_\ell) - \varphi_4(\lambda_0)$, and d is the perpendicular distance between the axes Q and Q'. d is related to the prism separation L as follows

$$\begin{aligned} L \approx L' &= \sqrt{d^2 + (d\tan\delta + X_1)^2} \\ L'' &= \sqrt{d^2 + (d\tan\delta + X_1 + X_2)^2} \end{aligned} \tag{B.18}$$

The insertion of P_2 along the axis O' results in a material amount of L_{m3}, as calculated from the Figs. B.1(e–f), is given by

$$L_{m3} = \overline{D'D''}\,\frac{\sin\alpha_p}{\cos\theta_6} = X_2\,\frac{\cos\delta}{\cos\varphi_4}\,\frac{\sin\alpha_p}{\cos\theta_6} \tag{B.19}$$

Owing to the similarity of angular dispersion of P_1 and P_4, the second prism pair (P_3-P_4) will be translated by a distance X_1, contributing an additional material length $L_{m4} = L_{m2}$. Substituting the Eqs.B.13–B.19 in B.11, the contribution due to the prism material for the double-pass configuration can be calculated, which in turn can be used to evaluate the effective dispersion of the prism compressor in a real setup.

Appendix C

Formulae for the peak power, peak intensity and peak fluence of a Gaussian pulse

Consider a pulse with a Gaussian beam profile in both the space (x,y) and time (t) domains. Let w_x and w_y denote the radii of the spatial beam profile at an intensity level of 1/e^2 along x and y axes, respectively in a plane perpendicular to the direction of propagation of the pulse. τ_p represents the full width at intensity half maximum (FWHM) of the temporal profile of the pulse, see Fig. C.1. The pulse energy (E_p) can be written as follows

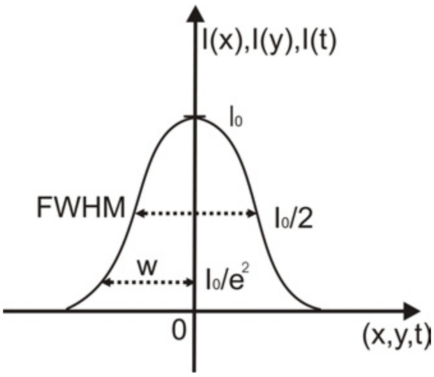

Figure C.1: Gaussian pulse

$$
\begin{aligned}
E_p &= I_0 \int_{-\infty}^{+\infty}\int_{-\infty}^{+\infty}\int_{-\infty}^{+\infty}\left[\exp\left(-2\,\frac{x^2}{w_x^2}\right)\cdot\exp\left(-2\,\frac{y^2}{w_y^2}\right)\cdot\exp\left(-4\ln 2\,\frac{t^2}{\tau_p^2}\right)\right]\mathrm{dxdydt} \\
&= I_0 \int_{-\infty}^{+\infty}\exp\left(-2\,\frac{x^2}{w_x^2}\right)\mathrm{dx}\cdot\int_{-\infty}^{+\infty}\exp\left(-2\,\frac{y^2}{w_y^2}\right)\mathrm{dy}\cdot\int_{-\infty}^{+\infty}\exp\left(-4\ln 2\,\frac{t^2}{\tau_p^2}\right)\mathrm{dt},
\end{aligned}
\tag{C.1}
$$

where I_0 is the peak intensity of the pulse. Substituting $\frac{2}{w_x^2}=a$, $\frac{2}{w_y^2}=b$, and $\frac{4\ln 2}{\tau_p^2}=c$ in Eq. C.1, we have

$$
\begin{aligned}
E_p &= I_0 \int_{-\infty}^{+\infty}\exp\left(-ax^2\right)\mathrm{dx}\cdot\int_{-\infty}^{+\infty}\exp\left(-by^2\right)\mathrm{dy}\cdot\int_{-\infty}^{+\infty}\exp\left(-ct^2\right)\mathrm{dt} \\
&= \sqrt{\frac{\pi}{a}}\cdot\sqrt{\frac{\pi}{b}}\cdot\sqrt{\frac{\pi}{c}},
\end{aligned}
\tag{C.2}
$$

because $\int_{-\infty}^{+\infty}\exp\left(-x^2\right)\mathrm{dx}=\sqrt{\pi}$. Therefore

$$
E_p = \pi^{3/2}\cdot\frac{w_x}{\sqrt{2}}\cdot\frac{w_y}{\sqrt{2}}\cdot\frac{\tau_p}{\sqrt{4\ln 2}}I_0 \tag{C.3}
$$

or

$$\begin{aligned} I_0 &= \frac{\sqrt{4\ln 2}}{\sqrt{\pi}} \cdot \frac{2E_p}{\pi w_x w_y \tau_p} \approx 0.598 \frac{E_p}{w_x w_y \tau_p} \\ &= \frac{\sqrt{4\ln 2}}{\sqrt{\pi}} \frac{F_0}{\tau_p} \approx 0.939 \frac{F_0}{\tau_p}, \end{aligned} \tag{C.4}$$

where $F_0 = \frac{2E_p}{\pi w_x w_y}$ is called the peak fluence.

Similarly, the peak power (P_0) of a Gaussian pulse can be calculated as

$$\begin{aligned} P_0 = I_0 &\int_{-\infty}^{+\infty} \int_{-\infty}^{+\infty} \exp\left(-2\,\frac{x^2}{w_x^2}\right) \cdot \exp\left(-2\,\frac{y^2}{w_y^2}\right) \mathrm{dxdy} \\ &= \frac{\pi w_x w_y}{2} I_0 \implies I_0 = \frac{2P_0}{\pi w_x w_y} \end{aligned} \tag{C.5}$$

Therefore, comparing Eqs. C.4 and C.5 we obtain

$$\begin{aligned} P_0 &= \frac{\sqrt{4\ln 2}}{\sqrt{\pi}} \cdot \frac{E_p}{\tau_p} \\ &\approx 0.939 \frac{E_p}{\tau_p} \end{aligned} \tag{C.6}$$

The average power (P_{av}) of a laser system with the pulse repetition rate of f can be determined from the following relation

$$P_{av} = f\,E_p \tag{C.7}$$

Appendix D

Redshift of few-cycle near-infrared pulses in filamentation regime

In the following we present the results of theoretical simulations on the long wavelength part of the supercontinuum produced by filamentation of few-cycle mJ-scale pulses near 800 nm in Argon. A brief overview of past developments in this subject is also presented.

Supercontinuum generation during the optical filamentation of femtosecond pulses in the gaseous media has been extensively discussed in literature, e.g. [121, 58, 130, 131, 132]. The ultrabroadband supercontinua obtained in the single-filamentation regime in Ar or air extending down to 200 nm in the ultraviolet [124, 133, 134, 135, 136] were demonstrated. Most of these studies, however, were devoted to the wavelength region below 1100 nm using the input pulses from Ti:sapphire based laser system which emit around $\lambda_0 = 800$ nm. The supercontinuum generation into the infrared, on the hand, has received limited attention to date. Recently, the extension of supercontinua into the near-infrared (NIR) domain by single filamentation of μJ-scale-energy femtosecond pulses in transparent solids has been examined in [80]. However the energy in the infrared tail of the supercontinuum was limited to the nJ-scale. Since our investigation was motivated by the need for high energy, broadband pulses in the NIR domain derived from a Ti:sapphire source for seeding the OPCPA chain of the PFS system. The nJ-scale seed energy, as presented in the scheme of spectral broadening using transparent solids [80], is too low to suppress the superfluorescence in the parametric amplifiers of our system [76]. From the available literature it can be seen that the input pulses of few-10 fs with carrier frequency at $\sim$ 800 nm does not show significant broadening into the infrared. This asymmetry in the broadband spectra is due to the fact that in addition to the classical SPM effect other processes such as pulse-steeping, ionization of gas atoms etc. also contribute to the blue shift. We therefore study the process of optical filamentation in a gaseous medium using sub-two-cycle pulse generated from the Ti:sapphire amplifier with spectral broadening in a conventional HCF [57] setup and its subsequent compression using a chirped mirror compressor (CMC).

The presented calculations are performed by Luc Bergé, CEA-DAM, DIF, F-91297 Arpajon, France to study the potential of spectral broadening into the NIR domain and its original using the input pulse of our setup. Moreover the spectral phase of newly generated frequencies (or wavelengths) were also analysed in these calculation. These simulations use linearly polarized input Gaussian pulses and the following feature of the optical filamentation were taken into account: natural diffraction, wavelength dependent dispersion, self-focusing, plasma generation and self-steepening effects.

We investigated a transform-limited pulse with Gaussian spectrum and FWHM duration of 3.4 fs. Figure D.1 details the characteristic dynamics of this pulse at moderate power, i.e. 15 P_{cr} (P_{cr} = 5.67 GW (Eq. 3.20), $E_{in} = 310\,\mu$J) and operating at 720 nm centre wavelength. The pulse at z = 0 has an input beam diameter of 4.4 mm at 1/e^2 level of the intensity profile and is focused by a lens of focal length f = 150 cm. As seen in Fig. D.1(a), the pulse self-focuses at $z_c = 1.25$ m, the nonlinear focus, due to the optical Kerr effect. It generates a tenuous plasma of maximum density limited to $1.5 \times 10^{17}\,\mathrm{cm}^{-3}$, leading to filament self-channeling over $\sim$20 cm (z denotes the longitudinal propagation variable) with a mean clamping intensity of $\sim$100 TW/cm^2. The inset details the intensity distribution of the pulse in the t-z-plane along the self-channelling range. Figure D.1(b) contains the temporal profiles at different z-positions along the same range. The time variable refers to a retarded time expressed in the frame moving with the linear group velocity of the pulse [131]. Slight temporal oscillations are caused by interferences between the pump and the third harmonic. Figure D.1(c) shows the corresponding spectra, averaged over the simulation box. Starting with a near-one-cycle pulse ($\tau_{o.c} = \lambda_0/c = 2.4\,\mathrm{fs}$), the pulse spectrum is initially broad, with a net asymmetry at long wavelengths. Owing to the dispersion, the pulse significantly broadens in time before the nonlinear focus. Beyond this point, pulse breakup occurs while self-steepening favours a shock profile at the trailing edge of the pulse ($t > 0$) along one focusing-defocusing sequence. Besides this shock dynamics responsible for the creation of blue shoulders in the spectra [135], the major feature is the occurrence of the focusing leading edge, i.e. sharp temporal gradients emerge in the front pulse ($t < 0$) (Fig. D.1(b)). Since frequency variations are directly linked to the temporal gradient of the nonlinear phase describing the interplay between Kerr self-focusing and plasma generation, a strong red shift marks the spectra driven by the steepest components of the front pulse [82]. In gas-based self-compression experiments mediated by filamentation, the pulses often attain few-cycle durations by enhancing their rear part to the detriment of the front one [167]. In the present context, we see the reverse route. A single-cycle pulse undergoes strong dispersion in time and self-focusing in space. The former starts to spread out the pulse in time, but contributes to promote pulse splitting through normal group-velocity dispersion near the nonlinear focus z_c [131],

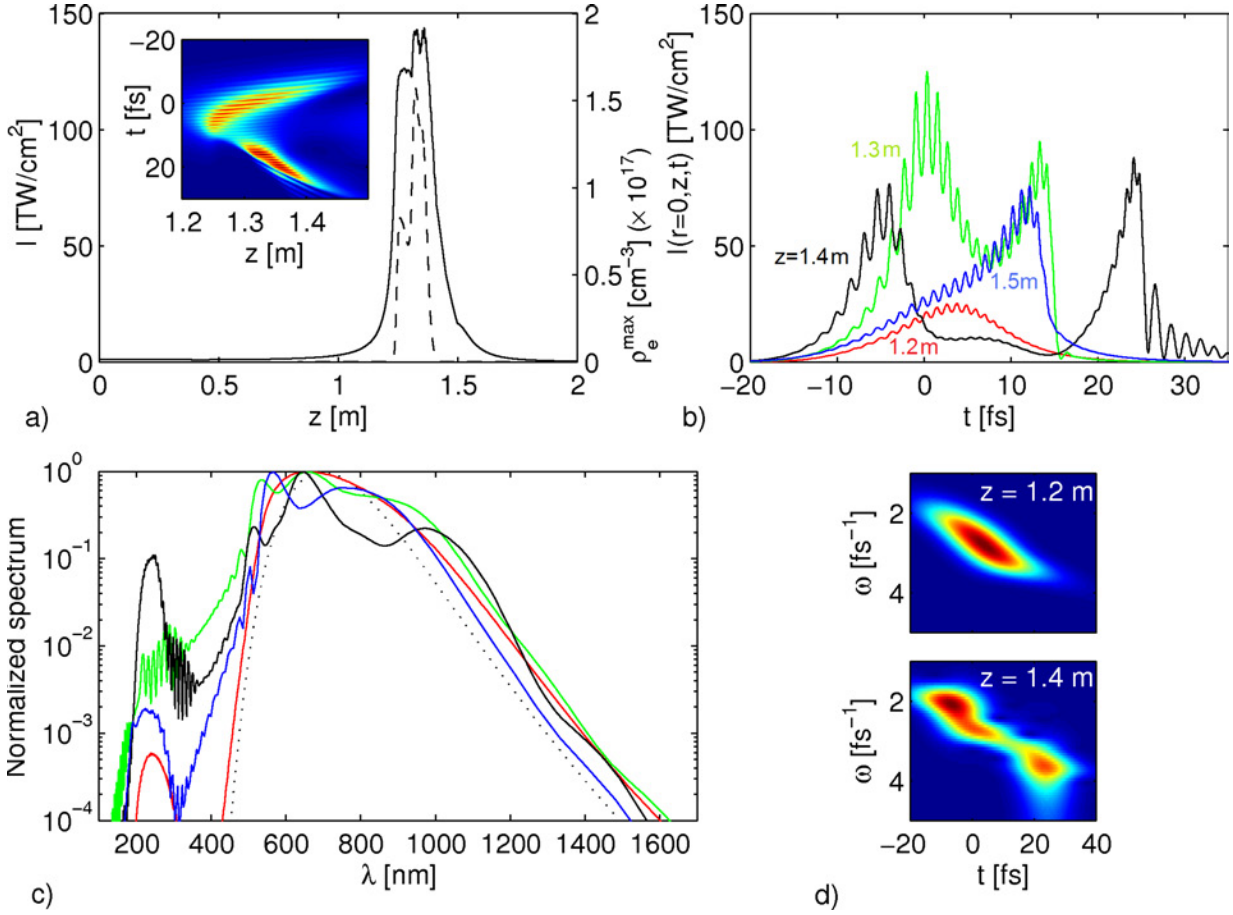

Figure D.1: a) Peak intensity (solid curve, left-hand side axis) and plasma density (dashed curve, right-hand side axis) developed in filamentation regime by a 3.4 fs Gaussian pulse at 720 nm with 15 P_{cr} in converging geometry (f = 150 cm) and in Ar at 0.8 bar pressure. The inset zooms the temporal dynamics between z = 1.2 m and z = 1.5 m. b) Temporal profiles at the propagation distances z = 1.2 m (red curve), z = 1.3 m (green curve), and z = 1.4 m (black curve). The blue curve shows the same pulse with reduced power, i.e. 5 P_{cr} only, at z = 1.5 m. c) Corresponding normalized intensity spectra averaged in the simulation box at the same distances. The dotted curve refers to the input spectrum. d) XFROG traces for the 15 P_{cr} pulse at specific distances.

whereas the latter triggers plasma defocusing that breaks up the pulse. At high enough powers, plasma generation and dispersion thus both favour pulse breakup. The Gaussian pulse is lengthened up to 14 fs at z = 1.2 m due to linear dispersion, then up to 45 fs due to plasma-induced pulse breakup. The resulting spectrum is broadened to almost 3 octaves (from 200 nm to 1600 nm) and the cut-off wavelength at the 10^{-4} level is red shifted by about 150 nm compared with the initial spectrum. To check our statement, we performed simulations discarding harmonic generation, self-steepening or dispersion. Only when dispersion was cancelled, the propagation pattern drastically changed, i.e. the nonlinear focus noticeably moved to shorter distances while the pulse tried to preserve its initial temporal profile at higher clamping intensity [168]. Therefore, at z = 1.2 m, SPM and dispersion are mainly responsible for the first red shift [see red curve in Fig. D.1(c)]. Note that, as the blue-visible bandwidth is enhanced by self-steepening, four-wave mixing $(\omega_{4WM} = 2\omega_0 - \omega_s)$ between the pump frequency (ω_0) and seeded high-frequencies (ω_s) may also contribute to the production of IR components, provided that $\omega_s < 2\omega_0$. However, creating wavelengths above 1500 nm requires the condition of exciting the spectral interval $360 \leq \lambda_s \leq 474\,\mathrm{nm}$ $\left(3.88 \leq \omega_s \leq 5.24\,\mathrm{fs}^{-1}\right)$, which seems barely fulfilled at this stage. At later distances ($z \geq$1.3 m), plasma-induced pulse breakup promotes sharp gradients in the front zone and 4WM can be more efficient. A second stage develops, characterized by the occurrence of a "red shoulder" (or "red hump"), centred around 1100 nm and visible between the levels 10^{-2} and 10^{-1}. This spectral evolution definitively requires sharp leading edges in the pulse profile. To underline the importance of the front pulse shape, we also plotted the temporal profile of the same pulse simulated with lower power ($5P_{cr}$). At clamping intensity, this pulse only steepens its trailing edge (see blue curve in Fig. D.1(b)) while the plasma density remains limited to a few 10^{15} cm^{-3}. In that case, the generated supercontinuum covers better the previous interval of high frequencies seeded for 4WM (see blue curve in Fig. D.1(c)). Nonetheless, the redshift remains limited to the broadening primarily caused by SPM, e.g. the red curve in Fig. D.1(c). These behaviours indicate that the "red hump" develops from the dynamical competition between all nonlinearities and dispersion yielding a prominent leading edge at high enough peak intensities. In Fig. D.1(d), we show a couple of cross-correlation frequency-resolved optical gating (XFROG) traces for the $15P_{cr}$ pulse at the distances z = 1.2 and 1.4 m. These traces confirm that the leading edge sharpening at negative times is associated with the enhancement of infrared wavelengths, while the steepening of the trailing edge at positive times is associated with an additional buildup of blue wavelengths in the spectrum. They also indicate that despite pulse splitting the group delay remains a single-valued function of the frequency. Hence, these pulses are expected to be compressible down to a transform-limited pulse duration close to 2 fs by appropriate dispersion management. Hence, we can conclude that for sub-two cycle pump pulses at high enough power the redshift first develops in a classical SPM broadening stage, followed by a second enhancement induced by sharp leading edges that marks the temporal pulse profile. Initiated by plasma defocusing and strong dispersion, this two-peaked profile preserves a focused front over a long distance, which is associated with the largest redshift in the spectrum.

Bibliography

[1] S. Karsch, Zs. Major, J. Fülöp, I. Ahmad, T.-J. Wang, A. Henig, S. Kruber, R. Weingartner, M. Siebold, J. Hein, C. Wandt, S. Klingebiel, J. Osterhoff, R. Hörlein, and F. Krausz, "The petawatt field synthesizer: A new approach to ultrahigh field generation," in "Advanced Solid-State Photonics," (Optical Society of America, 2008), p. WF1.

[2] Zs. Major, S. Trushin, I. Ahmad, M. Siebold, C. Wandt, S. Klingebiel, T. Wang, J. A. Fülöp, A. Henig, R. S. Kruber, A. Popp, J. Osterhoff, R. Hörlein, J. Hein, V. Pervak, A. Apolonski, F. Krausz, and S. Karsch, "Basic concepts and current status of the petawatt field synthesizer—a new approach to ultrahigh field generation," Review of Laser Engineering **37**, 431–436 (2009).

[3] D. Strickland and G. Mourou, "Compression of amplified chirped optical pulses," Opt. Comm. **56**, 219–221 (1985).

[4] A. Dubietis, G. Jonušauskas, and A. Piskarskas, "Powerful femtosecond pulse generation by chirped and stretched pulse parametric amplification in BBO crystal," Opt. Commun. **88**, 437 (1992).

[5] A. Einstein, *"On the quantum theory of radiation," in Laser Theory, F. A. Barnes, pp. 5-21* (IEEE Press, New York, 1972).

[6] T. H. Maiman, "Stimulated optical radiation in ruby," Nature **187**, 493–494 (1960).

[7] J. Hecht, "Short history of laser development," Opt. Eng. **49**, 091002 (2010). Note: The described chronology of early-age laser developement has been adapted from this article.

[8] A. Javan, W. R. Bennett, and D. R. Herriott, "Population inversion and continuous optical maser oscillation in a gas discharge containing a He-Ne mixture," Phys. Rev. Lett. **6**, 106 (1961).

[9] E. Snitzer, "Optical Maser Action of Nd^{+3} in a Barium Crown Glass," Phys. Rev. Lett. **7**, 444 (1961).

[10] R. N. Hall, G. E. Fenner, J. D. Kingsley, T. J. Soltys, and R. O. Carlson, “Coherent light emission from GaAs Junctions,” Phys. Rev. Lett. **9**, 366 (1962).

[11] C. K. N. Patel, “Continuous-wave laser action on vibrational rotational transitions of CO_2,” Phys. Rev. A **36**, 1187–1193 (1964).

[12] C. K. N. Patel, P. K. Tien, and J. H. McFee, “CW high-power CO_2–N_2-He laser,” Appl. Phys. Lett. **7**, 290–292 (1965).

[13] P. P. Sorokin and J. R. Lankard, “Stimulated emission observed from an organic dye, chloro-aluminum phthalocyanine,” IBM Journal of Research and Development **10**, 162–163 (1966).

[14] N. G. Basov, V. A. Danilychev, and Y. M. Popov, “Stimulated emission in the vacuum ultraviolet region,,” Sov. J. Quantum Electron **1**, 18–22 (1971).

[15] C. Hirlimann, *Femtosecond Laser Pulses: Principles and Experiments* (Springer-Verlag Berlin Heidelberg, 1998).

[16] W. E. Lamb, “Theory of an optical maser,” Phys. Rev. **134**, A1429 (1964).

[17] E. P. Ippen, C. V. Shank, and A. Dienes, “Passive mode locking of the cw dye laser,” Appl. Phys. Lett. **21**, 348–350 (1972).

[18] C. V. Shank and E. P. Ippen, “Subpicosecond kilowatt pulses from a mode-locked cw dye laser,” Appl. Phys. Lett. **24**, 373–375 (1974).

[19] J. C. Walling, O. G. Peterson, H. P. Jenssen, R. C. Morris, and E. W. O’Dell, “Tunable alexandrite lasers,” IEEE J. Quantum Electron. **QE-16**, 1302–1315 (1980).

[20] P. F. Moulton, “Spectroscopic and laser characteristics of Ti:Al_2O_3,” J. Opt. Soc. Am. B **3**, 125–133 (1986).

[21] D. E. Spence, P. N. Kean, and W. Sibbett, “60-fsec pulse generation from a self-mode-locked Ti:sapphire laser,” Opt. Lett. **16**, 42–44 (1991).

[22] A. Stingl, M. Lenzner, C. Spielmann, F. Krausz, and R. Szipöcs, “Sub-10-fs mirror-dispersion-controlled Ti:sapphire laser,” Opt.Lett. **20**, 602–604 (1995).

[23] R. Ell, U. Morgner, F. X. KÃÂrtner, J. G. Fujimoto, E. P. Ippen, V. Scheuer, G. Angelow, T. Tschudi, M. J. Lederer, A. Boiko, and B. Luther-Davies, “Generation of 5-fs pulses and octave-spanning spectra directly from a Ti:sapphire laser,” Opt. Lett. **26**, 373–375 (2001).

[24] S. Nolte, C. Momma, H. Jacobs, A. Tunnemann, B. N. Chichkov, B. Wellegehausen, and H. Welling, “Ablation of metals by ultrashort laser pulses,” J. Opt. Soc. Am. B **14**, 2716 (1997).

[25] H. Lubatschowsk, A. Heisterkamp, F. Will, A. Singh, J. Sebrin, A. Ostendorf, O. Kermani, R. Heermann, H. Welling, and W. Ertmer, “Medical applications for ultrafast laser pulses,” RIKEN Rev. **50**, 113 (2003).

[26] A. Zewail, “Femtochemistry: atomic-scale dynamics of the chemical bond using ultrafast lasers (nobel lecture).” Angew. Chem. Int. Ed. Engl. **39**, 2587–2631 (2000).

[27] F. Krausz and M. Ivanov, “Attosecond physics,” Rev. Mod. Phys. **81**, 163 (2009).

[28] M. F. Kling and M. J. Vrakking, “Attosecond electron dynamics,” Annu. Rev. Phys. Chem. **59**, 46392 (2008).

[29] P. M. Paul, E. S. Toma, P. Breger, G. Mullot, F. Augé, P. Balcou, H. G. Muller, and P. Agostini, “Observation of a train of attosecond pulses from high harmonic generation,” Science **292**, 1689–1692 (2001).

[30] M. Hentschel, R. Kienberger, C. Spielmann, G. A. Reider, N. Milosevic, T. Brabec, P. Corkum, U. Heinzmann, M. Drescher, and F. Krausz, “Attosecond metrology,” Nature **414**, 509–513 (2001).

[31] J. Seres, E. Seres, A. J. Verhoef, G. Tempea, C. Streli, P. Wobrauschek, V. Yakovlev, A. Scrinzi, C. Spielmann, and F. Krausz, “Laser technology: Source of coherent kiloelectronvolt X-rays,” Nature **433**, 596–596 (2005).

[32] P. B. Corkum and F. Krausz, “Attosecond science,” Nat Phys **3**, 381–387 (2007).

[33] E. Goulielmakis, Z.-H. Loh, A. Wirth, R. Santra, N. Rohringer, V. S. Yakovlev, S. Zherebtsov, T. Pfeifer, A. M. Azzeer, M. F. Kling, S. R. Leone, and F. Krausz, “Real-time observation of valence electron motion,” Nature **466**, 739–743 (2010).

[34] J. Faure, Y. Glinec, A. Pukhov, S. Kiselev, S. Gordienko, E. Lefebvre, J.-P. Rousseau, F. Burgy, and V. Malka, “A laser-plasma accelerator producing monoenergetic electron beams,” Nature **431**, 541–544 (2004).

[35] S. P. D. Mangles, C. D. Murphy, Z. Najmudin, A. G. R. Thomas, J. L. Collier, A. E. Dangor, E. J. Divall, P. S. Foster, J. G. Gallacher, C. J. Hooker, D. A. Jaroszynski, A. J. Langley, W. B. Mori, P. A. Norreys, F. S. Tsung, R. Viskup, B. R. Walton, and K. Krushelnick, “Monoenergetic beams of relativistic electrons from intense laser-plasma interactions,” Nature **431**, 535–538 (2004).

[36] C. G. R. Geddes, C. Toth, J. van Tilborg, E. Esarey, C. B. Schroeder, D. Bruhwiler, C. Nieter, J. Cary, and W. P. Leemans, “High-quality electron beams from a laser wakefield accelerator using plasma-channel guiding,” Nature **431**, 538–541 (2004).

[37] M. Geissler, J. Schreiber, and J. Meyer-ter Vehn, “Bubble acceleration of electrons with few-cycle laser pulses,” New Journal of Physics **8**, 186–186 (2006).

[38] Y. Nomura, R. Horlein, P. Tzallas, B. Dromey, S. Rykovanov, Zs. Major, J. Osterhoff, S. Karsch, L. Veisz, M. Zepf, D. Charalambidis, F. Krausz, and G. D. Tsakiris, "Attosecond phase locking of harmonics emitted from laser-produced plasmas," Nat. Phys **5**, 124–128 (2009).

[39] G. D. Tsakiris, K. Eidmann, J. Meyer-ter-Vehn, and F. Krausz, "Route to intense single attosecond pulses," New J. Phys. **8**, 19 (2006).

[40] M. Fuchs, R. Weingartner, A. Popp, Zs. Major, S. Becker, J. Osterhoff, I. Cortrie, B. Zeitler, R. Hörlein, G. D. Tsakiris, U. Schramm, T. P. Rowlands-Rees, S. M. Hooker, D. Habs, F. Krausz, S. Karsch, and F. Gruner, "Laser-driven soft-X-ray undulator source," Nat Phys **5**, 826–829 (2009).

[41] A. Henig, D. Kiefer, K. Markey, D. C. Gautier, K. A. Flippo, S. Letzring, R. P. Johnson, T. Shimada, L. Yin, B. J. Albright, K. J. Bowers, J. C. Fernńdez, S. G. Rykovanov, H.-C. Wu, M. Zepf, D. Jung, V. K. Liechtenstein, J. Schreiber, D. Habs, and B. M. Hegelich, "Enhanced laser-driven ion acceleration in the relativistic transparency regime," Phys. Rev. Lett. **103**, 045002 (2009).

[42] R. A. Snavely, M. H. Key, S. P. Hatchett, T. E. Cowan, M. Roth, T. W. Phillips, M. A. Stoyer, E. A. Henry, T. C. Sangster, M. S. Singh, S. C. Wilks, A. MacKinnon, A. Offenberger, D. M. Pennington, K. Yasuike, A. B. Langdon, B. F. Lasinski, J. Johnson, M. D. Perry, and E. M. Campbell, "Intense high-energy proton beams from petawatt-laser irradiation of solids," Phys. Rev. Lett. **85**, 2945–2948 (2000).

[43] V. Malka, S. Fritzler, F. Lefebvre, E. d′Humières, R. Ferrand, G. Grillon, C. Albaret, S. Meyroneinc, J. Chambaret, A. Antonetti, and D. Hulin, "Practicability of protontherapy using compact laser systems," Med. Phys. **31**, 1587–1592 (2004).

[44] G. A. Mourou, T. Tajima, and S. V. Bulanov, "Optics in the relativistic regime," Reviews of Modern Physics **78**, 309–371 (2006).

[45] E. B. Treacy, "Optical pulse compression with diffraction gratings," IEEE Journal of Quantum Electron **5**, 454–458 (1969).

[46] O. E. Martinez, "3000 times grating compressor with positive group velocity dispersion: Application to fiber compensation in 1.3–1.6 μm region," IEEE Journal of Quantum Electronics **23**, 59 (1987).

[47] R. L. Fork, O. E. Martinez, and J. P. Gordon, "Negative dispersion using pairs of prisms," Opt. Lett. **9**, 150–152 (1984).

[48] S. Kane and J. Squier, "Grism-pair stretcher–compressor system for simultaneous second- and third-order dispersion compensation in chirped-pulse amplification," J. Opt. Soc. Am. B **14**, 661–665 (1997).

[49] V. Pervak, I. Ahmad, S. A. Trushin, Zs. Major, A. Apolonski, S. Karsch, and F. Krausz, "Chirped-pulse amplification of laser pulses with dispersive mirrors," Opt. Express **17**, 19204–19212 (2009).

[50] Z. Cheng, F. Krausz, and C. Spielmann, "Compression of 2 mJ kilohertz laser pulses to 17.5 fs by pairing double-prism compressor: analysis and performance," Optics Communications **201**, 145–155 (2002).

[51] F. Tavella, Y. Nomura, L. Veisz, V. Pervak, A. Marcinkevîcius, and F. Krausz, "Dispersion management for a sub-10-fs, 10 TW optical parametric chirped-pulse amplifier," Opt. Lett. **32**, 2227–2229 (2007).

[52] M. Perry, "Crossing the petawatt threshold," Sci. Tech. Rev. **12**, 4–11 (1996).

[53] M. D. Perry, D. Pennington, B. C. Stuart, G. Tietbohl, J. A. Britten, C. Brown, S. Herman, B. Golick, M. Kartz, J. Miller, H. T. Powell, M. Vergino, and V. Yanovsky, "Petawatt laser pulses," Opt. Lett. **24**, 160–162 (1999).

[54] C. Danson, P. Brummitt, R. Clarke, J. Collier, B. Fell, A. Frackiewicz, S. Hancock, S. Hawkes, C. Hernandez-Gomez, P. Holligan, M. Hutchinson, A. Kidd, W. Lester, I. Musgrave, D. Neely, D. Neville, P. Norreys, D. Pepler, C. Reason, W. Shaikh, T. Winstone, R. Wyatt, and B. Wyborn, "Vulcan petawatt—an ultra-high-intensity interaction facility," Nuclear Fusion **44**, S239 (2004).

[55] Y. Kitagawa, H. Fujita, R. Kodama, H. Yoshida, S. Matsuo, T. Jitsuno, T. Kawasaki, H. Kitamura, T. Kanabe, S. Sakabe, K. Shigemori, N. Miyanaga, and Y. Izawa, "Prepulse-free petawatt laser for a fast ignitor," IEEE Journal of Quantum Electronics **40**, 281 – 293 (2004).

[56] M. Aoyama, K. Yamakawa, Y. Akahane, J. Ma, N. Inoue, H. Ueda, and H. Kiriyama, "0.85-PW, 33-fs Ti:sapphire laser," Opt. Lett. **28**, 1594–1596 (2003).

[57] M. Nisoli, S. D. Silvestri, and O. Svelto, "Generation of high energy 10 fs pulses by a new pulse compression technique," Appl. Phys. Lett. **68**, 2793 (1996).

[58] A. Couairon and A. Mysyrowicz, "Femtosecond filamentation in transparent media," Physics Reports **441**, 47–189 (2007).

[59] R. A. Baumgartner and R. L. Byer, "Optical parametric amplification," IEEE J. Quantum Electron. **QE-15**, 432 (1979).

[60] G. Cerullo and S. De Silvestri, "Ultrafast optical parametric amplifiers," Rev. Sci. Instrum. **74**, 1–18 (2003).

[61] E. A. Khazanov, V. V. Lozhkarev, G. I. Friedman, V. N. Ginzberg, E. V. Katin, A. V. Kirsanov, G. A. Luchinin, A. N. Mal'shakov, M. A. Matryanov, O. V. Palashov, A. K. Poteomkin, A. M. Sergeev, A. A. Shaykin, and I. V. Yakovlev, "Compact 0.56 petawatt laser system based on OPCPA," in "OSA Technical Digest (CD)," (Optical Society of America, 2007), p. ThB5.

[62] E. A. Khazanov and A. M. Sergeev, “Petawatt lasers based on optical parametric amplifiers: their state and prospects,” Physics-Uspekhi **51**, 969–974 (2008).

[63] A. Shirakawa, I. Sakane, and T. Kobayashi, “Pulse-front-matched optical parametric amplification for sub-10-fs pulse generation tunable in the visible and near infrared,” Opt. Lett. **23**, 1292–1294 (1998).

[64] Zs. Major, T.-J. Wang, I. Ahmad, S. A. Trushin, J. A. Fülöp, A. Henig, S. Kruber, R. Weingartner, M. Siebold, J. Hein, C. Wandt, S. Klingebiel, A. Popp, J. Osterhoff, R. Hörlein, V. Pervak, A. Apolonskiy, F. Krausz, and S. Karsch, “OPA Development on the Petawatt Field Synthesizer,” in “OSA Technical Digest Series (CD),” (Optical Society of America, 2009), p. MB5.

[65] T.-J. Wang, Zs. Major, I. Ahmad, S. A. Trushin, F. Krausz, and S. Karsch, “Ultra-broadband near-infrared pulse generation by noncollinear OPA with angular dispersion compensation,” Appl. Phys. B **100**, 207 (2009).

[66] E. Gaul, M. Martinez, J. Blakeney, M. Ringuette, D. Hammond, A. Jochmann, R. Escamilla, T. Borger, G. Dyer, and T. Ditmire, “Activation of a 1.1 petawatt hybrid, opcpa-nd:glass laser,” in “Lasers and Electro-Optics, 2009 and 2009 Conference on Quantum electronics and Laser Science Conference. CLEO/QELS 2009. Conference on,” (2009), pp. 1 –2.

[67] A. Lyachev, O. Chekhlov, J. Collier, R. Clarke, M. Galimberti, C. Hernandez-Gomez, P. Matousek, I. Musgrave, D. Neely, P. Norreys, I. Ross, Y. Tang, T. Winstone, and B. Wyborn, “The 10PW OPCPA Vulcan Laser Upgrade,” in “High Intensity Lasers and High Field Phenomena,” (Optical Society of America, 2011), p. HThE2.

[68] T. Graf, J. Mackenzie, H. Jelinkova, G. Paulus, V. Bagnoud, and C. Blanc, eds., *Extreme light infrastructure: laser architecture and major challenges*, vol. 7721 of *1*, The International Society for Optical Engineering (Proc. SPIE, 2010). Doi:10.1117/12.854687.

[69] E. Gerstner, “Laser physics: Extreme light,” Nature **446**, 16–18 (2007).

[70] M. Siebold, J. Hein, C. Wandt, S. Klingebiel, F. Krausz, and S. Karsch, “High-energy, diode-pumped, nanosecond Yb:YAG MOPA system,” Opt. Express **16**, 3674–3679 (2008).

[71] C. Wandt, S. Klingebiel, M. Siebold, Zs. Major, J. Hein, F. Krausz, and S. Karsch, “Generation of 220 mJ nanosecond pulses at a 10 Hz repetition rate with excellent beam quality in a diode-pumped Yb:YAG MOPA system,” Opt. Lett. **33**, 1111 (2008).

[72] S. Klingebiel, C. Wandt, C. Skrobol, I. Ahmad, S. A. Trushin, Zs. Major, F. Krausz, and S. Karsch, “High energy picosecond Yb:YAG CPA system at 10 Hz repetition rate for pumping optical parametric amplifiers,” Opt. Express **19**, 5357–5363 (2011).

[73] E. Innerhofer, T. Südmeyer, F. Brunner, R. Häring, A. Aschwanden, R. Paschotta, C. Hönninger, M. Kumkar, and U. Keller, "60-W average power in 810-fs pulses from a thin-disk Yb:YAG laser," Opt. Lett. **28**, 367–369 (2003).

[74] P. Lacovara, H. K. Choi, C. A. Wang, R. L. Aggarwal, and T. Y. Fan, "Room-temperature diode-pumped yb:yag laser," Opt. Lett. **16**, 1089–1091 (1991).

[75] V. Lozhkarev, G. Freidman, V. Ginzburg, E. Katin, E. Khazanov, A. Kirsanov, G. Luchinin, A. Mal'shakov, M. Martyanov, O. Palashov, A. Poteomkin, A. Sergeev, A. Shaykin, and I. Yakovlev, "Compact 0.56 petawatt laser system based on optical parametric chirped pulse amplification in KD*P crystals," Laser Physics Letters **4**, 421–427 (2007).

[76] F. Tavella, A. Marcinkevičius, and F. Krausz, "Investigation of the superfluorescence and signal amplification in an ultrabroadband multiterawatt optical parametric chirped pulse amplifier system," New J. of Phys. **8**, 219 (2006).

[77] J. Itatani, J. Faure, M. Nantel, G. Mourou, and S. Watanabe, "Suppression of the amplified spontaneous emission in chirped-pulse-amplification lasers by clean high-energy seed-pulse injection," Optics Communications **148**, 70–74 (1998).

[78] C. Teisset, N. Ishii, T. Fuji, T. Metzger, S. Köhler, R. Holzwarth, A. Baltuška, A. Zheltikov, and F. Krausz, "Soliton-based pump–seed synchronization for few-cycle OPCPA," Opt. Express **13**, 6550–6557 (2005).

[79] P. Russell, "Photonic crystal fibers," Science **299**, 358–362 (2003).

[80] M. Bradler, P. Baum, and E. Riedle, "Femtosecond continuum generation in bulk laser host materials with sub-μJ pump pulses," Applied Physics B: Lasers and Optics **97**, 561 (2009).

[81] F. Mitschke and L. Mollenauer, "Discovery of the soliton self-frequency shift," Opt. Lett. **1**, 659–661 (1986).

[82] G. Agrawal, *Nonlinear Fiber Optics* (Academic Press, San Diego,, 2001).

[83] X. Liu, C. Xu, W. Knox, J. Chandalia, B. Eggleton, S. Kosinski, and R. Windeler, "Soliton selffrequency shift in a short tapered air-silica microstructure fiber," Opt. Lett. **26**, 358–360 (2001).

[84] W. Reeves, D. Skryabin, F. Biancalana, J. Knight, P. Russell, F. Omenetto, A. Efimov, and A. Taylor, "Transformation and control of ultra-short pulses in dispersion-engineered photonic crystal fibres," Nature **424**, 511–515 (2003).

[85] E. Serebryannikov, A. Zheltikov, N. Ishii, C. Teisset, S. Köhler, T. Fuji, T. Metzger, F. Krausz, and A. Baltuška, "Soliton self-frequency shift of 6-fs pulses in photonic-crystal fibers," Appl. Phys. B **81**, 585–588 (2005).

[86] P. Banks, M. Perry, V. Yanovsky, S. Fochs, B. Stuart, and J. Zweiback, “Novel all-reflective stretcher for chirped-pulse amplification of ultrashort pulses,” Quantum Electronics, IEEE Journal of **36**, 268–274 (2000).

[87] M. Pessot, P. Maine, and G. Mourou, “1000 times expansion/compression of optical pulses for chirped pulse amplification,” Optics Communications **62**, 419–421 (1987).

[88] G. Pretzler, “Höchstleistungs-kurzpulslaser,” Lecture notes (unpublished).

[89] J. C. Diels and W. Rudolph, *Ultrashort Laser Pulse Phenomena: Fundamentals, Techniques, and Applications on a Femtosecond Time Scale* (Elsevier, 2006), 2nd ed.

[90] J. Britten, “Diffraction gratings for high-intensity laser applications,” Tech. Rep. LLNL-BOOK-401125, Lawrence Livermore National Laboratory, Livermore, CA 94550. (2008).

[91] Optical design program: RAYTRACE, ver. 0.9(12), University of Erlangen-Nuremberg. `http://www.optik.uni-erlangen.de/odem/`.

[92] J. Neauport, E. Lavastre, G. Razé, G. Dupuy, N. Bonod, M. Balas, G. de Villele, J. Flamand, S. Kaladgew, and F. Desserouer, “Effect of electric field on laser induced damage threshold of multilayer dielectric gratings,” Opt. Express **15**, 12508–12522 (2007).

[93] D. Kane and R. Trebino, “Characterization of arbitrary femtosecond pulses using frequency-resolved optical gating,” IEEE J. Quantum Electron **29 (2)**, 571 (1993).

[94] C. Iaconis and I. Walmsley, “Spectral phase interferometry for direct electric-field reconstruction of ultrashort optical pulses,” Opt. Lett. **23**, 792–794 (1998).

[95] G. Pretzler, A. Kasper, and K. Witte, “Angular chirp and tilted light pulses in CPA lasers,” Appl. Phys. B **70**, 1 (2000).

[96] Z. Sacks, G. Mourou, and R. Danielius, “Adjusting pulse-front tilt and pulse duration by use of a single-shot autocorrelator,” Opt. Lett. **26**, 462 (2001).

[97] P. Tournois, “Acousto-optic programmable dispersive filter for adaptive compensation of group delay time dispersion in laser systems,” Optics Communications **140**, 245–249 (1997).

[98] A. L. Cavalieri, E. Goulielmakis, B. Horvath, W. Helml, M. Schultze, M. Fiess, V. Pervak, L. Veisz, V. S. Yakovlev, M. Uiberacker, A. Apolonski, F. Krausz, and R. Kienberger, “Intense 1.5-cycle near infrared laser waveforms and their use for the generation of ultra-broadband soft-x-ray harmonic continua,” New Journal of Physics **9**, 242 (2007).

[99] S. Sartania, Z. Cheng, M. Lenzner, G. Tempea, C. Spielmann, F. Krausz, and K. Ferencz, “Generation of 0.1-TW 5-fs optical pulses at a 1-kHz repetition rate,” Opt. Lett. **22**, 1562–1564 (1997).

[100] R. W. Boyd, *Nonlinear Optics* (Elsevier, 2003), 2nd ed.

[101] S. A. Planas, N. L. P. Mansur, C. H. B. Cruz, and H. L. Fragnito, “Spectral narrowing in the propagation of chirped pulses in single-mode fibers,” Opt. Lett. **18**, 699–701 (1993).

[102] V. Pervak, C. Teisset, A. Sugita, S. Naumov, F. Krausz, and A. Apolonski, “High-dispersive mirrors for femtosecond lasers,” Opt. Express **16**, 10220–10233 (2008).

[103] R. Szipöcs, K. Ferencz, C. Spielmann, and F. Krausz, “Chirped multilayer coatings for broadband dispersion control in femtosecond lasers,” Opt. Lett. **19**, 201 (1994).

[104] R. Sziöcs, A. Köházi-Kis, S. Laká, P. Apai, A. Kovács, G. DeBell, L. Mott, A. Louderback, A. Tikhonravov, and M. Trubetskov, “Negative dispersion mirrors for dispersion control in femtosecond lasers: chirped dielectric mirrors and multi-cavity Gires-Tournois interferometers,” Applied Physics B: Lasers and Optics **70**, S51–S57 (2000).

[105] V. Laude and P. Tournois, “Chirped-mirror pairs for ultra-broadband dispersion control,” in “Summaries of Papers Presented at the Conference on Lasers and Electro-Optics, CLEO’99,” (1999), pp. 187–188. DOI:`10.1109/CLEO.1999.834063`.

[106] R. Paschotta, “Encyclopedia of laser physics and technology,” `http://www.rp-photonics.com/spotlight_2009_10_03.html`.

[107] O. Uteza, B. Bussire, F. Canova, J.-P. Chambaret, P. Delaporte, T. Itina, and M. Sentis, “Laser-induced damage threshold of sapphire in nanosecond, picosecond and femtosecond regimes,” Applied Surface Science **254**, 799–803 (2007).

[108] S. Backus, C. G. Durfee, M. M. Murnane, and H. C. Kapteyn, “High power ultrafast lasers,” Rev. Sci. Instrum. **69**, 1207 (1998).

[109] G. Fibich and A. L. Gaeta, “Critical power for self-focusing in bulk media and in hollow waveguides,” Opt. Lett. **25**, 335–337 (2000).

[110] A. von Conta, “Characterization of the laser induced damage threshold of mirrors in the ultrashort pulse regime,” Master’s thesis, Fakultät für Feinwerk- und Mikrotechnik/Physikalische Technik, Hochschule München (2010).

[111] I. Ahmad, S. A. Trushin, Zs. Major, C. Wandt, S. Klingebiel, T.-J. Wang, V. Pervak, A. Popp, M. Siebold, F. Krausz, and S. Karsch, “Frontend light source for short-pulse pumped OPCPA system,” Applied Physics B: Lasers and Optics **97**, 529–536 (2009).

[112] V. Pervak. Ludwig-Maximilians-Universität München, Am Coulombwall 1, D-85748 Garching, Germany, private communication, December 2010.

[113] I. Ahmad, S. Trushin, V. Pervak, C. Wandt, S. Klingebiel, Zs. Major, M. Siebold, F. Krausz, and S. Karsch, "Hybrid pulse compressor for 1.5 mJ, sub-23 fs CPA System," in "CLEO/Europe and EQEC 2009 Conference Digest," (Optical Society of America, 2009), pp. CF3–5.

[114] A. C. Eckl, "Perspectives of Implementation: All Dispersive Mirror Compressor (ADMC) for Femtosecond High Power Ti:Sapphire Lasers," Bechelor's thesis, Fakultät für Physik, Ludwig-Maximilians-Universität München (2010).

[115] F. Tavella, "Multiterawatt few-cycle pulse OPCPA for applications in high-Field physics," Ph.D. thesis, Ludwig-Maximilians-Universit at M unchen, Germany (2009).

[116] I. N. Ross, P. Matousek, G. H. C. New, and K. Osvay, "Analysis and optimization of optical parametric chirped pulse amplification," J. Opt. Soc. Am. B **19**, 2945–2956 (2002).

[117] `http://www.okotech.com/linear`.

[118] J. A. Fülöp, Zs. Major, A. Henig, S. Kruber, R. Weingartner, T. Clausnitzer, E.-B. Kley, A. Tünnermann, V. Pervak, A. Apolonski, J. Osterhoff, R. Hörlein, F. Krausz, and S. Karsch, "Short-pulse optical parametric chirped-pulse amplification for the generation of high-power few-cycle pulses," New J. Phys. **9**, 438 (2007).

[119] K. Varjú, A. Kovács, G. Kurdi, and K. Osvay, "High-precision measurement of angular dispersion in a CPA laser," Applied Physics B: Lasers and Optics **74**, s259–s263 (2002). DOI:10.1007/s00340-002-0882-z.

[120] M. Feit and J. Fleck, "Effect of refraction on spot-size dependence of laser-induced breakdown," Appl. Phys. Lett. **24**, 169–172 (1974).

[121] C. Hauri, W. Kornelis, F. Helbing, A. Heinrich, A. Couairon, A. Mysyrowicz, J. Biegert, and U. Keller, "Generation of intense, carrier-envelope phase-locked few-cycle laser pulses through filamentation," Applied Physics B: Lasers and Optics **79**, 673–677 (2004). 10.1007/s00340-004-1650-z.

[122] A. Braun, G. Korn, X. Liu, D. Du, J. Squier, and G. Mourou, "Self-channeling of high-peak-power femtosecond laser pulses in air," Opt. Lett. **20**, 73–75 (1995).

[123] J. T. Manassah, *The supercontinuum laser source*, 184 (Springer, New York, 1989).

[124] K. Kosma, S. A. Trushin, W. Fuss, and W. E. Schmid, "Characterization of the supercontinuum radiation generated by self-focusing of few-cycle 800 nm pulses in argon," Journal of Modern Optics **55**, 2141 (2008).

[125] F. DeMartini, C. Townes, T. Gustafson, and P. Kelley, "Self-steepening of light pulses," Phys. Rev. **164**, 312–323 (1967).

[126] J. E. Rothenberg, “Space-time focusing: breakdown of the slowly varying envelope approximation in the self-focusing of femtosecond pulses,” Opt. Lett. **17**, 1340–1342 (1992).

[127] J. K. Ranka and A. L. Gaeta, “Breakdown of the slowly varying envelope approximation in the self-focusing of ultrashort pulses,” Opt. Lett. **23**, 534–536 (1998).

[128] I. Ahmad, L. Bergé, Zs. Major, F. Krausz, S. Karsch, and S. Trushin, “Redshift of few-cycle infrared pulses in the filamentation regime,” To be published.

[129] C. W. Thiel, “Four-wave mixing and its applications,” `http://www.physics.montana.edu/students/thiel/docs/FWMixing.pdf`.

[130] S. L. Chin, S. A. Hosseini, W. Liu, Q. Luo, F. Théberge, N. Aközbek, A. Becker, V. P. Kandidov, O. G. Kosareva, and H. Schroeder, “The propagation of powerful femtosecond laser pulses in optical media: Physics, applications, and new challenges,” Can. J. Phys. **83**, 863 (2005).

[131] L. Bergé, S. Skupin, R. Nuter, J. Kasparian, and J.-P. Wolf, “Ultrashort filaments of light in weakly ionized, optically transparent media,” Reports on Progress in Physics **70**, 1633 (2007).

[132] J. Kasparian and J.-P. Wolf, “Physics and applications of atmospheric nonlinear optics and filamentation,” Opt. Express **16**, 466 (2008).

[133] E. Goulielmakis, S. Koehler, B. Reiter, M. Schultze, A. J. Verhoef, E. E. Serebryannikov, A. M. Zheltikov, and F. Krausz, “Ultrabroadband, coherent light source based on self-channeling of few-cycle pulses in helium,” Opt. Lett. **33**, 1407–1409 (2008).

[134] S. A. Trushin, S. Panja, K. Kosma, W. E. Schmid, and W. Fuss, “Supercontinuum extending from $>$ 1000 to 250 nm, generated by focusing 10-fs laser pulses at 805 nm into Ar,” Appl. Phys. B **80**, 399 (2005).

[135] N. Akozbek, S. A. Trushin, A. Baltuska, W. Fuss, E. Goulielmakis, K. Kosma, F. Krausz, S. Panja, M. Uiberacker, W. E. Schmid, A. Becker, M. Scalora, and M. Bloemer, “Extending supercontinuum spectrum down to 200 nm by self-phase modulation of few-cycle 800-nm pulses in argon,” New Journal of Physics **8**, 177 (2006).

[136] S. Skupin and L. Bergé, “Supercontinuum generation of ultrashort laser pulses in air at different central wavelengths,” Opt. Commun. **280**, 173 (2007).

[137] TEM Messtechnik GmbH, *BeamLock-4D User Manual*. `http://www.tem-messtechnik.de/`.

[138] T. Kanai, A. Suda, S. Bohman, M. Kaku, S. Yamaguchi, and K. Midorikawa, “Pointing stabilization of a high-repetition-rate high-power femtosecond laser for intense few-cycle pulse generation,” Appl. Phys. Lett. **92**, 061106–3 (2008).

[139] A. Couairon, M. Franco, G. Méchain, T. Olivier, B. Prade, and A. Mysyrowicz, "Femtosecond filamentation in air at low pressures: Part I: Theory and numerical simulations," Optics Communications **259**, 265–273 (2006).

[140] V. Pervak, I. Ahmad, M. K. Trubetskov, A. V. Tikhonravov, and F. Krausz, "Double-angle multilayer mirrors with smooth dispersion characteristics," Opt. Express **17**, 7943–7951 (2009).

[141] F. X. Kärtner, N. Matuschek, T. Schibli, U. Keller, H. A. Haus, C. Heine, R. Morf, V. Scheuer, M. Tilsch, and T. Tschudi, "Design and fabrication of double-chirped mirrors," Opt. Lett. **22**, 831–833 (1997).

[142] N. Matuschek, L. Gallmann, D. H. Sutter, G. Steinmeyer, and U. Keller, "Back-side-coated chirped mirrors with ultrasmooth broadband dispersion characteristics," Appl. Phys. B **71**, 509–522 (2000).

[143] P. Baum, M. Breuer, E. Riedle, and G. Steinmeyer, "Brewster-angled chirped mirrors for broadband pulse compression without dispersion oscillations," Opt. Lett. **31**, 2220–2222 (2006).

[144] H. Macleod, *Thin-Film Optical Filters* (Bristol: Adam Hilger Ltd., 2001), 3rd ed.

[145] J. L. Chilla and O. E. Martinez, "Frequency domain phase measurement of ultrashort light pulses. effect of noise," Optics Communications **89**, 434–440 (1992).

[146] D. Milam, M. J. Weber, and A. J. Glass, "Nonlinear refractive index of fluoride crystals," Appl. Phys. Lett. **31**, 822 (1977).

[147] D. Lorenc, M. Aranyosiova, R. Buczynski, R. Stepien, I. Bugar, A. Vincze, and D. Velic, "Nonlinear refractive index of multicomponent glasses designed forfabrication of photonic crystal fibers," Applied Physics B: Lasers and Optics **93**, 531–538 (2008). 10.1007/s00340-008-3217-x.

[148] E. T. J. Nibbering, M. A. Franco, B. S. Prade, G. Grillon, C. Le Blanc, and A. Mysyrowicz, "Measurement of the nonlinear refractive index of transparent materials by spectral analysis after nonlinear propagation," Optics Communications **119**, 479–484 (1995).

[149] D. Milam, "Review and assessment of measured values of the nonlinear refractive-index coefficient of fused silica," Appl. Opt. **37**, 546–550 (1998).

[150] T. Kobayashi and A. Baltuska, "Sub-5 fs pulse generation from a noncollinear optical parametric amplifier," Meas. Sci. Technol. **13**, 1671 (2002).

[151] T. Miura, K. Kobayashi, K. Takasago, Z. Zhang, K. Torizuka, and F. Kannari, "Timing jitter in a kilohertz regenerative amplifier of a femtosecond-pulse Ti:Al_2O_3 laser," Opt. Lett. **25**, 1795 (2000).

[152] S. Klingebiel, I. Ahmad, C. Wandt, C. Skrobol, S. A. Trushin, Zs. Major, F. Krausz, and S. Karsch, "Experimental and theoretical investigation of timing jitter inside a stretcher/compressor setup," To be published.

[153] D. Brida, C. Manzoni, G. Cirmi, M. Marangoni, S. Bonora, P. Villoresi, S. De Silvestri, and G. Cerullo, "Few-optical-cycle pulses tunable from the visible to the mid-infrared by optical parametric amplifiers," Journal of Optics **12**, 013001 (2010).

[154] N. Ishii, L. Turi, V. S. Yakovlev, T. Fuji, F. Krausz, A. Baltuska, R. Butkus, G. Veitas, V. Smilgevicius, R. Danielius, and A. Piskarskas, "Multimillijoule chirped parametric amplification offew-cycle pulses," Opt. Lett. **30**, 567–569 (2005).

[155] S. Witte, R. T. Zinkstok, A. L. Wolf, W. Hogervorst, W. Ubachs, and K. S. E. Eikema, "A source of 2 terawatt, 2.7 cycle laser pulses based on noncollinear optical parametric chirped pulse amplification," Opt. Express **14**, 8168–8177 (2006).

[156] D. Herrmann, L. Veisz, R. Tautz, F. Tavella, K. Schmid, V. Pervak, and F. Krausz, "Generation of sub-three-cycle, 16 TW light pulses by using noncollinear optical parametric chirped-pulse amplification," Opt. Lett. **34**, 2459–2461 (2009).

[157] O. Chalus, P. K. Bates, M. Smolarski, and J. Biegert, "Mid-IR short-pulse OPCPA with micro-Joule energy at 100 kHz," Opt. Express **17**, 3587–3594 (2009).

[158] S. Adachi, N. Ishii, T. Kanai, A. Kosuge, J. Itatani, Y. Kobayashi, D. Yoshitomi, K. Torizuka, and S. Watanabe, "5-fs, multi-mJ, CEP-locked parametric chirped-pulse amplifier pumped by a 450-nm source at 1 kHz," Opt. Express **16**, 14341–14352 (2008).

[159] X. Gu, G. Marcus, Y. Deng, T. Metzger, C. Teisset, N. Ishii, T. Fuji, A. Baltuska, R. Butkus, V. Pervak, H. Ishizuki, T. Taira, T. Kobayashi, R. Kienberger, and F. Krausz, "Generation of carrier-envelope-phase-stable 2-cycle 740-μJ pulses at 2.1-μm carrier wavelength," Opt. Express **17**, 62–69 (2009).

[160] K. W. Aniolek, R. L. Schmitt, T. J. Kulp, B. A. Richman, S. E. Bisson, and P. E. Powers, "Microlaser-pumped periodically poled lithium niobate optical parametric generator-optical parametric amplifier," Opt. Lett. **25**, 557–559 (2000).

[161] V. V. Lozhkarev, G. I. Freidman, V. N. Ginzburg, E. A. Khazanov, O. V. Palashov, A. M. Sergeev, and I. V. Yakovlev, "Study of broadband optical parametric chirped pulse amplification in a DKDP crystal pumped by the second harmonic of a Nd : YLF laser," Laser Physics **15**, 1319–1333 (2005).

[162] Y. Mori, I. Kuroda, S. Nakajima, T. Sasaki, and S. Nakai, "New Nonlinear-optical Crystal - Cesium Lithium Borate," Applied Physics Letters **67**, 1818–1820 (1995).

[163] B. Zhao, X. Liang, Y. Leng, Y. Jiang, C. Wang, H. Lu, J. Du, Z. Xu, and D. Shen, "Degenerated optical parametric chirped-pulse amplification with cesium lithium borate," Appl. Opt. **45**, 565–568 (2006).

[164] A. Buck, M. Nicolai, K. Schmid, C. M. S. Sears, A. Savert, J. M. Mikhailova, F. Krausz, M. C. Kaluza, and L. Veisz, "Real-time observation of laser-driven electron acceleration," Nat Phys **advance online publication**, – (2011).

[165] I. Ahmad, V. Pervak, S. Trushin, Zs. Major, S. Karsch, and F. Krausz, "Compression of mj-scale chirped-amplified pulses to sub-20 fs using high-dispersive mirrors," in "OSA Technical Digest Series (CD)," (Optical Society of America, 2010), p. AMD5.

[166] S. Zherebtsov, T. Fennel, J. Plenge, E. Antonsson, I. Znakovskaya, A. Wirth, O. Herrwerth, F. Suszmann, C. Peltz, I. Ahmad, S. A. Trushin, V. Pervak, S. Karsch, M. J. J. Vrakking, B. Langer, C. Graf, M. I. Stockman, F. Krausz, E. Ruhl, and M. F. Kling, "Controlled near-field enhanced electron acceleration from dielectric nanospheres with intense few-cycle laser fields," Nat Phys **advance online publication**, – (2011).

[167] C. Brée, A. Demircan, S. Skupin, L. Bergé, and G. Steinmeyer, "Self-pinching of pulsed laser beams during filamentary propagation," Opt. Express **17**, 16429 (2009).

[168] L. Bergé. CEA-DAM, DIF, F-91297 Arpajon, France, private communication, November 2010.

Acknowledgements

First all, I would like to thank to almighty Allah who gifted me the life, health, remembrance, and honour. My heartiest gratitude to Prof. Ferenc Krausz for giving me an opportunity to work at the Max-Planck-Institute of Quantum Optics, Garching. I am very grateful to Prof. Stefan Karsch for supervising me during my PhD studies and continuously supporting me with his ideas, perception, experience, and knowledge. Many thanks to Prof. Abdallah M. Azzeer for sparing some time from his very busy schedule to review my dissertation. I would also like to say my special gratitudes to Zsuzsanna Major who always backed me with her professional and moral support. Her valuable expertise in laser and OPCPA development proved to be very beneficial for me. I always found her very helpful, sympathetic and kind.

I am deeply indebted to Sergei Trushin for his cooperation and guidance through out my work— both in the lab and at the time of thesis writing. It was a great pleasure to work with you, Sergei!. I am also very much thankful to Dr. Javed Akhtar and Dr. Mushtaq Ahmed in Pakistan for suggesting me this fascinating field of research. I appreciate the contributions to my work from my very nice colleagues: Sandro Klingebiel, Christoph Wandt, Tie-Jun Wang, Christoph Skrobol, Antonia Popp, Rainer Hörlein, Xun Gu and Sergey Zherebtsov. Many thanks to Luc Bergé (Arpajon, France) for his collaboration on the "NIR redshift in filamenation" manuscript. Bundle of thanks to Vladimir Pervak for designing and manufacturing a variety of dispersive mirrors for this work. Thanks to Anna Caroline Eckl and Aaron von Conta for their cooperation during their own diploma works at the MPQ. I would also like to acknowledge the technical support from Mr. Schönauer, Mr. Strobl, Mr. Haas, Mr. Fischer, Mr. Grote and Mr. Böswald. Without their help, life would have been very complicated. It was a great chance to learn Autodesk-Inventor and machining from Mr. Schönauer. Special thanks are due to Mrs. Wild. I found her organizing abilities invincible. I am also grateful to Franziska Hoss, Thorsten Naeser, and all the staff from purchase department for their assistance. Financial support from the Higher-Education Commission of Pakistan (HEC-DAAD 2006) is also acknowledged. Many thanks to Monika Osman at the DAAD for her technical support regarding my PhD stipend.

I am very much thankful to my grandparents for their motivations and prayers for my bright future (May their souls rest in Jannat-ul-Fridos!). Hope it would be a great gift for them if I dedicate my thesis to them. My deepest gratitudes are to my parents, my wife and my whole family for their prayers, encouragement and unconditional support. Lots of love to little Abeeha and Hub-e-Fatima...

Curriculum vitae

IZHAR AHMAD

Present Address:	Hans-Kopfermann Str.1, D-85748, Garching, Germany
Permanent Address:	Village & PO: 346 G.B., Toba Tek Singh, Pakistan
Personnel:	Date of birth: 09.10.1978 Place of birth: Toba Tek Singh, Pakistan
Contacts:	+4917664167310 (Germany) +923005392161 (Pakistan) izhar.ahmad@mpq.mpg.de izhar916@yahoo.com

Education

PhD Studies Nov. 2006–July 2011

Max-Planck Institute of Quantum Optics, Garching, Germany

Field of studies: few-optical-cycle pulse generation, short-pulse pumped OPCPA

Thesis title: “Development of an optically synchronized seed source for a high-power few-cycle OPCPA system”

M.Engg in Nuclear Power Plant Engineering 2003

KINPOE, NED University of Engineering and Technology, Karachi, Pakistan

CGPA: all courses= 3.44/4.0, graduate courses= 3.6/4.0

Thesis title: “Design of the shielding cask for the KANUPP booster fuel assembly”

MSc in Physics 2000

Govt. College of Science, Fasialabad, Pakistan (affiliated with the “University of the Punjab,

Lahore, Pakistan")
Total marks: 832/1200, 1st division
Major subjects: advanced electronics, electricity and magnetism, classical mechanics, thermodynamics, nuclear physics.

Academic Honors

Doctoral scholarship 2006–2010
Higher Education Commission of Pakistan in collaboration with the German Academic Exchange Service (DAAD)

KINPOE fellowship for M.Engg 2001–2003
Karachi Institute of Nuclear Power Engineering, Karachi, Pakistan

Languages

Urdu – native language
English
German

Scientific Research

PhD studies 2006–2011
Max-Planck Institute of Quantum Optics, Garching, Germany
Development of an optically synchronized seed source for a high-power few-cycle OPCPA system— Petawatt Field Synthesizer (PFS)

Sr. Scientist 2003–2006
Optics Labs, Nilore, Islamabad, Pakistan
R&D experience with different types of Lasers, such as Nd:YAG (cw); He:Ne, Lambda-Physik Dye-Laser, Spectrophotometer and Monochrometer

Peer-reviewed Journal Papers

1. Zs. Major, S. A Trushin, **I. Ahmad**, M. Siebold, C. Wandt, S. Klingebiel, T.-J. Wang, J. A. Fülöp, A. Henig, S. Kruber, R. Weingartner, A. Popp, J. Osterhoff, R. Hörlein, J. Hein, V. Pervak, A. Apolonski, F. Krausz, and S. Karsch, "Basic concepts and current status of

the Petawatt Field Synthesizer—a new approach to ultrahigh field generation," Rev. Laser Eng. 37, 431 (2009)

2. V. Pervak, **I. Ahmad**, S. A. Trushin, Zs. Major, A. Apolonski, S. Karsch, and F. Krausz, "Chirped-pulse amplification of laser pulses with dispersive mirrors," Opt. Exp. 17, 19204 (2009)
3. V. Pervak, **I. Ahmad**, M. K. Trubetskov, A. V. Tikhonravov, and F. Krausz, "Double-angle multilayer mirrors with smooth dispersion characteristics," Opt. Exp. 17, 7943 (2009)
4. V. Pervak, **I. Ahmad**, J. A. Fülöp, M. K. Trubetskov, and A. V. Tikhonravov, "Comparison of dispersive mirrors based on the time-domain and conventional approaches for sub-5 fs pulses," Opt. Exp. 17, 2207 (2009)
5. **I. Ahmad**, S.A Trushin, Zs. Major, C. Wandt, S. Klingebiel, V. Pervak, A. Popp, T.-J. Wang, M. Siebold, F. Krausz and S. Karsch, "Frontend light source for short-pulse pumped OPCPA System," Appl. Phys. B 97, 529 (2009)
6. T.-J. Wang, Zs. Major, **I. Ahmad**, S. Trushin, F. Krausz and S. Karsch, "Ultrabroadband near-infrared pulse generation by noncollinear OPA with angular dispersion compensation," Appl. Phys. B 100, 207 (2010)
7. S. Klingebiel, C. Wandt, C. Skrobol, **I. Ahmad**, S. A. Trushin, Zs. Major, F. Krausz, and S. Karsch, "High energy picosecond Yb:YAG CPA system at 10 Hz repetition rate for pumping optical parametric amplifiers," Opt. Exp. 19, 5357 (2011)
8. S. Zherebtsov, T. Fennel, J. Plenge, E. Antonsson, I. Znakovskaya, A. Wirth, O. Herrwerth, F. Suszmann, C. Peltz, **I. Ahmad**, S. A. Trushin, V. Pervak, S. Karsch, M. J. J. Vrakking, B. Langer, C. Graf, M. I. Stockman, F. Krausz, E. Ruhl, and M. F. Kling, "Controlled near-field enhanced electron acceleration from dielectric nanospheres with intense few-cycle laser fields," Nat Phys. advance online publication, – (2011).
9. **I. Ahmad**, L. Bergé, S.A. Trushin, Zs. Major, F. Krausz and S. Karsch, "Redshift of few-cycle infrared pulses in filamentation regime," to be published
10. S. Klingebiel, **I. Ahmad**, C. Wandt, C. Skrobol, S. Trushin, Zs. Major, F. Krausz, and S. Karsch, "Experimental and theoretical investigation of timing jitter inside a stretcher/compressor setup," to be published
11. "Efficient amplification of broadband near-infrared radiation by picosecond OPCPA in DKDP pumped at 515 nm," in preparation

Peer-reviewed Conference Papers

1. M. Siebold, C. Wandt, S. Klingebiel, Zs. Major, S. Trushin, **I. Ahmad**, T-J. Wang, J. Hein, F. Krausz, and S. Karsch, “High-energy diode-pumped Yb:YAG chirped pulse amplifier,” Proc. of SPIE Vol. 6998, 69980E, (2008)

2. S. Karsch, Zs. Major, J. Fülöp, **I. Ahmad**, T.-J. Wang, A. Henig, S. Kruber, R. Weingartner, M. Siebold, J. Hein, C. Wandt, S. Klingebiel, J. Osterhoff, R. Hörlein, and F. Krausz, “ The Petawatt Field Synthesizer: A New Approach to Ultrahigh Field Generation,” in Advanced Solid-State Photonics (Optical Society of America, 2008), p. WF1

3. M. Siebold, S. Klingebiel, C. Wandt, Zs. Major, A. Popp, **I. Ahmad**, T. Wang, J. Hein, F. Krausz, and S. Karsch, “High Energy Diode-Pumped Yb:YAG Laser for ns-Pulses,” in Advanced Solid-State Photonics, OSA Technical Digest Series (CD) (Optical Society of America, 2008), paper MF3.

4. **I. Ahmad**, S. A. Trushin, Zs. Major, C. Wandt, S. Klingebiel, V. Pervak, A. Popp, T.-J. Wang, M. Siebold, F. Krausz, and S. Karsch, “Optically Synchronized Frontend for High-Power Short-Pulse OPCPA System,” in Advanced Solid-State Photonics (Optical Society of America, 2009), p. TuB8

5. Zs. Major, T. Wang, **I. Ahmad**, S. Trushin, J. A. Fülöp, A. Henig, S. Kruber, R. Weingartner, M. Siebold, J. Hein, C. Wandt, S. Klingebiel, A. Popp, J. Osterhoff, R. Hörlein, V. Pervak, A. Apolonskiy, F. Krausz, and S. Karsch, “OPA Development on the Petawatt Field Synthesizer,” in Advanced Solid-State Photonics, OSA Technical Digest Series (CD) (Optical Society of America, 2009), paper MB5.

6. S. Klingebiel, C. Wandt, M. Siebold, Zs. Major, **I. Ahmad**, S. Trushin, R. Hörlein, T.-J. Wang, F. Krausz, and S. Karsch, “Counteracting Gain Narrowing Using Spectral Amplitude Shaping in a High-Energy Diode-Pumped CPA System Based on Yb-Doped Materials,” in Advanced Solid-State Photonics, OSA Technical Digest Series (CD) (Optical Society of America, 2009), paper TuB9.

7. C. Wandt, S. Klingebiel, R. Hörlein, **I. Ahmad**, T. Wang, S. Trushin, Zs. Major, M. Siebold, J. Hein, F. Krausz, and S. Karsch, “High-Energy, Diode-Pumped CPA to the Joule-Level Based on Yb-Doped Materials,” in Advanced Solid-State Photonics, OSA Technical Digest Series (CD) (Optical Society of America, 2009), paper WA4.

8. C. Wandt, S. Klingebiel, **I. Ahmad**, T. Wang, S. Trushin, Zs. Major, M. Siebold, F. Krausz, and S. Karsch, “High-energy, diode-pumped CPA based on Yb-doped materials,”

in CLEO/Europe and EQEC 2009 Conference Digest, (Optical Society of America, 2009), paper CA4_5.

9. **I. Ahmad**, S.A Trushin, , V. Pervak ,Zs. Major, C. Wandt, S. Klingebiel, M. Siebold, F. Krausz and Stefan Karsch, “Hybrid Pulse Compressor for 1.5 mJ, sub-23 fs CPA System,” in CLEO-Europe 2009, CF3.5

10. **I. Ahmad**, V. Pervak, S. Trushin, Zs. Major, S. Karsch, and F. Krausz “Implementation of HDM as all-mirror compressor in mJ-scale sub-20-fs chirped pulse amplifier,” in the Technical Digest of UltraFast Optics (UFO VII) and High Field Short Wavelength (HFSW XIII), Arcachon, France (2009)

11. Zs. Major, S. Klingebiel, C. Skrobol, **I. Ahmad**, C. Wandt, S. A. Trushin, F. Krausz, and S. Karsch, “Status of the Petawatt Field Synthesizer—pump-seed synchronization measurements,” AIP Conf. Proc. 1228, 117 (2010).

12. **I. Ahmad**, L. Bergé, S. A. Trushin, Zs. Major, S. Karsch, and F. Krausz, “Supercontinuum extending from 270 to 1400 nm generated by focusing sub-5-fs laser pulses at 720 nm into argon,” in Technical Digest of COFIL 2010: 3rd International Symposium on Filamentation, Crete, Greece, (2010).

13. **I. Ahmad**, V. Pervak, S. Trushin, Zs. Major, S. Karsch, and F. Krausz, “Compression of mJ-scale chirped-amplified pulses to sub-20 fs using high-dispersive mirrors,” in OSA Technical Digest Series (CD), (Optical Society of America, 2010), p. AMD5.

14. **I. Ahmad**, S. Klingebiel, C. Skrobol, C.Wandt, S. Trushin, Zs. Major, F. Krausz, and S. Karsch, “Pump-seed synchronization measurements for high-power short-pulse pumped few-cycle OPCPA system,” in Advanced Solid-State Photonics, (Optical Society of America, 2010), p. AMB9.

15. V. Pervak, **I. Ahmad**, S. Trushin, Zs. Major, S. Karsch, and F. Krausz , ”Dispersive mirror compressor for chirped pulse amplifiers,” 36th European Conference and Exhibition on Optical Communication (ECOC), p. 1–3, (2010) doi: 10.1109/ECOC.2010.5621337

16. S. Zherebtsov, T. Fennel, J. Plenge, E. Antonsson, I. Znakovskaya, A. Wirth, O. Herrwerth, F. Süßmann, C. Peltz, **I. Ahmad**, S. Trushin, V. Pervak, S. Karsch, M. Vrakking, B. Langer, C. Graf, M. Stockman, F. Krausz, E. Rühl, and M. Kling, “Controlled electron acceleration from dielectric nanospheres in intense few-cycle laser fields,” in CLEO/Europe and EQEC 2011 Conference Digest, OSA Technical Digest (CD) (Optical Society of America, 2011), paper EI1_5.

17. Zs. Major, C. Skrobol, **I. Ahmad**, C. Wandt, S. Klingebiel, S. A. Trushin, F. Krausz, and S. Karsch, “Towards Joule-scale few-cycle pulses - progress and challenges of short-pulse pumped OPCPA,” in High Intensity Lasers and High Field Phenomena, OSA Technical Digest (CD) (Optical Society of America, 2011), paper HThE1.

Conferences

- International Nathiagali Summer College on Physics & Contemporary Needs, June 28, 2004, Nathiagali, Pakistan
- Deutsche Physikalische Gesellschaft (DPG) Frühjahrstagung (DPG Spring Meeting), March 10, 2008, Darmstadt, Germany
- Advanced Solid-State photonics (Optical Society of America, 2009), February 02, 2009, Denver, USA
- The European Conference on Lasers and Electro-Optics and the XIth European Quantum Electronics Conference (CLEO/Europe-EQEC), June 14–16, Munich, Germany
- The UltraFast Optics (UFO VII) and High Field Short Wavelength (HFSW XIII) Conference, August 31 -September 4, 2009, Arcachon, France
- Advanced Solid-State Photonics (ASSP), January 31-February 03, 2010, San Diego, USA
- COFIL 2010: 3rd International Symposium on Filamentation, May 31–June 05, 2010, Crete, Greece